Synthesis and photocatalytic properties of Bi_2S_3 and metal doped Bi_2S_3 nanoparticles

V.M Nkwe

Orcid.org/0000-0002-3253-318

1

Dissertation submitted in fulfilment of the requirements for the degree *MSc Chemistry* at the North-West University

Supervisor: Prof. D.C. Onwudiwe

Co-supervisor: Dr. J. Osuntokun

Graduation: April 2019

Student number: 24299618

DECLARATION

I hereby declare that the work presented in this research project entitled: "Synthesis and photocatalytic properties of Bi_2S_3 and metal doped Bi_2S_3 nanoparticles" submitted for the requirement of MSc degree (chemistry) to the Department of Chemistry, North-West University, Mafikeng Campus is an original research work of my own under the supervision of Prof. D.C. Onwudiwe. This research work has not previously been submitted to any other University or by another student of the North-West University or other University.

Signature: ----------

Violet Mmatsie Nkwe

ACKNOWLEDGEMENTS

I would like to thank my Lord Jesus Christ and Saviour for giving me the strength, grace and courage to execute this research work. If it wasn't for His Grace I wouldn't have completed this work.

I am also very grateful to my supervisor, Prof. D.C. Onwudiwe for his guidance, encouragement, and thoroughness during the supervision of this research process, because it wouldn't be possible without his input and time. Thank you and God bless you abundantly.

I wish to express my sincere gratitude to my Co-supervisor Dr Jejenija Osuntokun for his contribution towards the success of this work; I would like to thank him for the wonderful work he did, and his time. God bless you. I sincerely appreciate the HOD Dr Mkhize and the Director Prof Katata-Seru for their support and encouragement.

I also thank our laboratory technicians; Mr Mokalane Kagiso and Loyilani Sizwe for their time in assisting me to characterize my analytical samples. My unalloyed special thanks go to the greatest people ever, the Inorganic chemistry research group, Ms Fola Felicia Bohinihi, Mr Jerry Adeyemi, Ms Mathato Motaung, Ms Tshabo Papane, Dr E.E Elemeka for their encouragement, professional advice, unlimited and diversified support to me throughout the course of this work. I love you very deeply and God bless you all.

Lastly, I would like to thank; Sasol bursary and my mentor Mr Moeketsi Olebogeng for his mentorship and support, NRF funding, North-West University postgraduate bursary for financial supports and the NWU Mafikeng Campus. Big thanks to my family and friends, for their faith in me, kindness and for the endless prayers.All the sources cited included as referencing are also acknowledged.

TABLE OF CONTENTS

Contents

DECLARATION i

ACKNOWLEDGEMENTS ii

TABLE OF CONTENTS iii

LIST OF FIGURES vi

LIST OF SCHEMES ix

LIST OF ABBREVIATION x

ABSTRACT xii

CHAPTER 1 1

1.0 INTRODUCTION 1

1.1 Background of bismuth sulphide 1

1.3 General background on semiconductors 2

1.4. Classification of semiconductors 3

1.5 Doping of semiconductor nanoparticles 3

1.6 General background on nanoparticles 4

1.7 Classification of the nanomaterials 5

1.8 Photocatalytic activity 7

1.9 Morphology and structural properties for photocatalytic activity 8

1.10 Strategies for improving photocatalytic activity 8

1.2 Problem statement 11

1.3 AIM AND OBJECTIVES 12

1.3.1 Aim 12

1.3.2 Objectives 12

CHAPTER 2 16

2.0 LITERATURE REVIEW 16
2.1 Bismuth sulphide by microwave synthetic route 17
2.2 Bismuth sulphide by hydrothermal route 18
2.3 Bismuth sulphide by single source precursor synthetic route 19
2.4 Metal doped bismuth sulphide 20
2.5 Common dyes in photocatalytic studies 21
2.6 Photocatalytic property of Bi_2S_3 nanoparticles and its composites 22
2.7 Photocatalytic property of metal doped Bi_2S_3 nanoparticles 23
CHAPTER 3 28
3.0 EXPERIMENTAL PROCEDURE 28
3.1 Preparation of the dithiocarbamate ligands and complexes 28
3.1.1 Synthesis of sodium 4-methyl-phenyldithiocarbamate [NaL^1] 28
3.1.3 Synthesis of sodium *N*-benzyldithiocarbamate [NaL^3] 29
3.2. Synthesis of the bismuth dithiocarbamate complexes 29
3.3 Synthesis of bismuth sulphide nanomaterials 30
3.3.1 Synthesis of Bi_2S_3 nanorods by solvothermal method 30
3.3.2 Synthesis of Bi_2S_3 nanoparticles by microwave method 31
3.4 Synthesis of Mn(II) and Sn(IV) doped Bi_2S_3 nanomaterials by hydrothermal method 31
3.5 Characterization of metal complexes 31
3.6 Characterization of the Bi_2S_3 nanoparticles 32
3.7 Photocatalytic evaluation of the Bi_2S_3 and metal doped Bi_2S_3 nanomaterials 32
3.8 Results and Discussion 32
3.8.1 Synthesis of the dithiocarbamate ligands and complexes 32
3.8.3 NMR spectroscopic studies of the complexes 35
3.8.4 Thermal studies 39

CHAPTER 4 43
4.1. DISCUSSION 43
4.1 XRD studies 43
4.2 TEM studies 47
4.2.1 Microwave irradiation method 47
4.2.2 Solvothermal method 49
4.2.3 Hydrothermal method 53
4.3 EDX analysis of Bi_2S_3 doped with Mn ions 57
4.3.1 EDX analysis 57
4.4 UV-vis studies 60
4.4.1 Tauc plots of Bi_2S_3 60
4.4.1 UV-vis of Mn doped Bi_2S_3 62
4.5 Evaluation of photocatalytic property 66
4.6. MB degradation process 75
CHAPTER 5 80
CONCLUSION 80
5.2 FUTURE STUDIES 83
APPENDIX 84
FTIR results 84

LIST OF FIGURES

Figure 1.1: Bismuth sulphide (Bi_2S_3) [1]. 1
Figure 1.2: Comparison between the insulator, semiconductor and conductor[12]. 2
Figure 1.3: Variation in colours of Au nanoparticles with differences in sizes and shapes [22].... 5
Figure 1.4: Schematic illustration of structural dimensionality of materials with expected 6
properties [23]. 6
Figure 1.5: Mechanism of photocatalysis by oxidative decomposition [27]. 7
Figure 1.6:Water pollution by different industrial effluents [34-36] 11
Figure 2.1: Methylene blue dye structure 21
Scheme 3.1: Structures of the synthesized (a) Bi(III) tris (4-methyl-phenyldithiocarbamate), (b) Bi(III) tris (N-phenyldithiocarbamate), and (c) Bi(III) tris (N-benzyldithiocarbamate) complexes. 33
Figure 3.2: **(a)** ^{1}H and **(b)** ^{13}C NMR spectra of Bi(III) tris(4-methyl-phenyldithiocarbamate) complex, **[Bi(L^1)$_3$]**. 36
Figure 3.3: **(a)** ^{1}H and **(b)** ^{13}C NMR spectra of Bi(III) tris (N-phenyldithiocarbamate) complex, **[Bi(L^2)$_3$]**. 37
Figure 3.4: **(a)** ^{1}H and **(b)** ^{13}C NMR spectra of Bi(III) tris (N-benzyldithiocarbamate) complex, **[Bi(L^3)$_3$]**. 38
Figure 3.5: TG/DTG curves of **[Bi(L^1)$_3$]**, **[Bi(L^2)$_3$]**, and **[Bi(L^3)$_3$]**,obtained under nitrogen atmosphere. 40
Figure 4.1: XRD of (a) undoped and (b) Mn doped Bi_2S_3 nanomaterials obtained from **[Bi(L^1)$_3$]**. 44
Figure 4.2: XRD of (a) undoped and (b) Mn doped Bi_2S_3 nanomaterials obtained from **[Bi(L^2)$_3$]**. 44
Figure 4.3: XRD of (a) undoped and (b) Mn doped Bi_2S_3 nanomaterials obtained from **[Bi(L^3)$_3$]**. 45
..... 45
Figure 4.4: XRD of (a) undoped and (b) Sn doped Bi_2S_3 nanomaterials obtained from **[Bi(L^1)$_3$]**. 45

Figure 4.5: XRD of (a) undoped and (b) Sn doped Bi_2S_3nanomaterials obtained from [**Bi(L^2)$_3$**]. 46
Figure 4.6: XRD of (a) undoped and (b) Sn doped Bi_2S_3 nanomaterials obtained from [**Bi(L^3)$_3$**]. 46
Figure 4.7: TEM images of Bi_2S_3 synthesized from complex [**Bi(L^1)$_3$**]..... 48
Figure 4.8: TEM images of Bi_2S_3 synthesized from complex [**Bi(L^2)$_3$**]..... 48
Figure 4.9: TEM images of Bi_2S_3 synthesized from complex [**Bi(L^3)$_3$**]..... 49
Figure 4.10: TEM micrograph ofBi_2S_3(1) nanorods prepared from [**BiL^1_3**] at **(a)** low magnification, **(b)** high magnification, inset-HRTEM showing lattice fringes; with corresponding particle size histogram showing **(c)** width and **(d)** length of the nanorods..... 50
Figure 4.11: TEM micrograph of Bi_2S_3(2) nanorods prepared from [**BiL^2_3**] at **(a)** low magnification, **(b)** high magnification, inset-HRTEM showing lattice fringes; with corresponding particle size histogram showing **(c)** width and **(d)** length of the nanorods..... 51
Figure 4.12: TEM micrograph of Bi_2S_3(3) nanorods prepared from [**BiL^3_3**] at **(a)** low magnification, **(b)** high magnification, inset-HRTEM showing lattice fringes; with corresponding particle size histogram showing **(c)** width and **(d)** length of the nanorods..... 52
Figure 4.13: TEM micrograph of Mn doped Bi_2S_3(1)prepared from [**Bi(L^1)$_3$**] at **(a)** low magnification, **(b)** high magnification, inset-HRTEM showing lattice fringes; with corresponding particle size histogram showing **(c)** width and **(d)** length of the nanorods..... 53
Figure 4.14: TEM images of Mn doped Bi_2S_3(2)prepared from [**Bi(L^2)$_3$**] at **(a)** low magnification, **(b)** high magnification, inset-HRTEM showing lattice fringes; with corresponding particle size histogram showing **(c)** width and **(d)** length of the nanorods..... 54
Figure 4.15: TEM images of Sn doped Bi_2S_3(1) prepared from [**Bi(L^1)$_3$**] at **(a)** low magnification, **(b)** high magnification, inset-HRTEM showing lattice fringes; with corresponding particle size histogram showing **(c)** width and **(d)** length of the nanorods..... 55
Figure 4.16: TEM images of Sn doped Bi_2S_3(2) prepared from [**Bi(L^2)$_3$**] at **(a)** low magnification, **(b)** high magnification, inset-HRTEM showing lattice fringes; with corresponding particle size histogram showing **(c)** width and **(d)** length of the nanorods..... 56
Figure 4.17: EDX spectra of Mn doped Bi_2S_3 obtained from [**Bi(L^1)$_3$**], [**Bi(L^2)$_3$**], and [**Bi(L^3)$_3$**]. 58
Figure 4.18: EDX spectra of Sn doped Bi_2S_3 obtained from [**Bi(L^1)$_3$**], [**Bi(L^2)$_3$**], and [**Bi(L^3)$_3$**]. 59

Figure 4.20: UV-vis spectra Mn doped Bi_2S_3 nanomaterials prepared from (a) [**Bi(L^1)$_3$**], (b) [**Bi(L^2)$_3$**] and [**Bi(L^3)$_3$**]; and their corresponding plot of $(\alpha h\nu)^2$ versus hν. 63
Figure 4.21: UV-vis spectra Sn doped Bi_2S_3nanomaterials prepared from (a) [**Bi(L^1)$_3$**], (b) [**Bi(L^2)$_3$**] and [**Bi(L^3)$_3$**]; and their corresponding plot of $(\alpha h\nu)^2$ versus hν. 65
Figure 4.22: (a) The absorption spectra of aqueous MB at different time intervals, and (b) percentage degradation of MB with change in time, using Bi_2S_3(1) prepared using [**Bi(L^1)$_3$**]. ... 68
Figure 4.23: (a) Absorption spectra of aqueous MB at different time intervals, and (b) percentage degradation of MB with change in time, using Bi_2S_3(2) prepared using [**Bi(L^2)$_3$**]. 69
Figure 4.24: (a) Absorption spectra of aqueous MB and (b) percentage degradation of MB using Bi_2S_3(3) prepared using [**Bi(L^3)$_3$**]. 70
Figure 4.25: (a) Absorption spectra of aqueous MB and (b) percentage degradation of MB using Sn doped Bi_2S_3(1). 71
Figure 4.26: (a) Absorption spectra of aqueous MB, and (b) percentage degradation of MB using Sn doped Bi_2S_3(2). 72
Figure 4.27: (a) Absorption spectra of aqueous MB and (b) percentage degradation of MB using Mn doped Bi_2S_3(1). 73
Figure 4.28: (a) The absorption spectra of aqueous MB and (b) percentage degradation of MB using Mn doped Bi_2S_3(2). 74
Figure 4.29: Schematic representation of degradation of MB in (a) pure Bi_2S_3, (b) metal doped Bi_2S_3 with intermediate band [30]. 76
Scheme 4.1: Chemical structure of MB and the photocatalytic reaction pathway [31]. 76
Figure **S1:** (a) **NaL^1** and (b) **BiL$^1_3$** (4-methyl-N-phenyldithiocarbamate) 84
Figure **S2:** (a) **NaL^2** and (b) **BiL$^2_3$** (N-phenyldithiocarbamate) 85
Figure **S3:** (a) **NaL^3** and (b) **BiL$^3_3$** (N-benzyldithiocarbamate) 86

LIST OF SCHEMES

Scheme 3.1: Structures of the synthesized (a) Bi(III) tris (4-methyl-phenyldithiocarbamate), (b) Bi(III) tris(N-phenyldithiocarbamate), and (c) Bi(III) tris(N-benzyldithiocarbamate).....33

Scheme 4.1: Chemical structure of MB and the photocatalytic reaction pathway 76

LIST OF ABBREVIATION

Bi_2S_3	Bismuth sulphide
NPs	Nanoparticles
MB	Methylene blue
TDBS	Tin-doped Bi_2S_3
G-C_3N_4	Graphitic carbon nitride
$Bi_2O_2CO_3$	Bismuth subcarbonate
BiOCl	Bismuth oxychloride
Bi_2O_3	Bismuth(III) oxide
FTIR	Fourier transform infrared spectroscopy
UV-vis	Ultraviolet-visible spectroscopy
TGA	Thioglycolic acid
SEM	Scanning electron microscopy
TEM	Transmission electron microscopy
HRTEM	High resolution transmission electron microscopy
SAED	Selected area electron diffraction
XRD	X-ray diffraction
PL	Photoluminescence
SSP	Single source precursor
RhB	Rhodamine B
MO	Methyl orange

THF	Tetrahydrofuran
NaOH	Sodium Hydroxide
TOP	Trioctylphosphine
HDA	Hexadecylamine
SA	Salicylic acid
STS	Sodium thiosulphate
VB	Valence band
CB	Conduction band
0D	Zero dimensional
1D	One dimensional
2D	Two dimensional
3D	Three dimensional
CO_2	Carbon dioxide
TiO_2	Titanium dioxide
$AgBiS_2$	Silver doped bismuth sulphide
SC	Semiconductor

ABSTRACT

Intriguing prospects for the development of materials with improved properties for optical, electronic and catalytic applications has motivated research in novel materials. Semiconductor nanoparticles exhibit variable and controllable properties which are associated with the change in the energy structure with size decrease which affects their optoelectronic properties. Interestingly, metal sulphide nanomaterials have stimulated great interest as a result of their value in basic scientific research and prospective technological applications due to their good properties and potential applications in areas such as electronic, optical and catalytic materials. Besides the rich structural diversity and pronounced quantum confinement effects, metal sulphides are widely utilised in many areas of environmental benefits. Bismuth sulphide (Bi_2S_3) is one of the important members of semiconducting chalcogenides of the type A_2B_3 (where A = Sb, Bi, As, and B = S, Se, Te). This research reports pure Bi_2S_3 and metal doped Bi_2S_3 nanoparticles using bismuth(III) dithiocarbamate as single source precursor. A series of Bi(III) complexes of 4-methyl-*N*-phenyldithiocarbamate, *N*-phenyldithiocarbamate and *N*-benzyldithiocarbamate were successfully prepared and characterized by NMR and FTIR spectroscopic techniques, and elemental analysis. The complexes were represented as **$[Bi(L^1)_3]$**, **$[Bi(L^2)_3]$** and **$[Bi(L^3)_3]$** respectively. In the FTIR spectra of the complexes, the stretching frequencies of ν(C-S) for all the complexes were found in the range of 1012-1030 cm^{-1} region. This indicated the presence of bindentate form of bonding in the dithiocarbamate compounds. The three complexes:**$[Bi(L^1)_3]$**, **$[Bi(L^2)_3]$** and **$[Bi(L^3)_3]$** were utilized as precursor compounds to prepare bismuth sulphide nanostructures which were represented as Bi_2S_3(1), Bi_2S_3(2), and Bi_2S_3(3), respectively using both microwave and solvothermal routes. Furthermore, Mn and Sn doped Bi_2S_3(1), Bi_2S_3(2), and Bi_2S_3(3) were respectively prepared using autoclave method. The undopedBi_2S_3 and metal doped Bi_2S_3 nanomaterials were characterized using UV-vis spectroscopy, photoluminescence (PL) spectroscopy, transmission electron microscopy (TEM), high-resolution transmission electron microscopy (HRTEM) and X-ray diffraction (XRD) analysis. The XRD results confirmed the feasibility of obtaining orthorhombic structure Bi_2S_3 nanoparticles from a single source precursor and the EDX was also used to confirm the presence of the respective dopants in the metal doped Bi_2S_3. The TEM results for the undoped and metal doped Bi_2S_3 nanomaterials prepared by solvothermal and hydrothermal methods respectively

showed nanorods of about 100 nm in length and 20 nm in diameter, while the products obtained via microwave method gave spherical morphology of about 100 nm in size, but with observable agglomeration. Both the diameter and length of the Bi_2S_3 nanorods increases with the increasing concentration of bismuth precursor. The evaluation of the photocatalytic properties of the nanorods obtained via solvothermal and autoclave routes were carried out using methylene blue as test compound. The results indicated that about 82-87% of MB was photocatalytically degraded after 150 min under visible light irradiation using the undoped Bi_2S_3 nanorods. However, the metal doped Bi_2S_3 nanorods showed the higher photocatalytic activity above 90% of methylene blue (MB) degradation. These results could be ascribed to the excellent visible light absorption of Bi_2S_3 nanomaterials and the efficient separation of photoinduced electron-hole pairs by the metal doped Bi_2S_3 nanomaterials. In conclusion all of the nanorods have good photocatalytic activity for degradation of MB. However, the small nanorods in metal doping have the highest degradation efficiency due to high surface area. Therefore, it is expected that the Bi_2S_3 nanorods have potential in applications in the photocatalytic degradation of organic pollutants. The use of metal doped Bi_2S_3 nanorods in water treatment may guide the development of future semiconductor photocatalysts in environmental remediation.

CHAPTER 1

1.0 INTRODUCTION

1.1 Background of bismuth sulphide

Bismuth sulphide (Bi_2S_3) is a stable and environmentally friendly material which has direct band gap energy of 1.30 eV. It is a brown solid (Figure 1.1), which occurs in nature as a lead-grey to tin white material known as bismuthite [1]. Bismuth sulphide is described as a semiconductor because its conductivity lies between that of the insulators (non-conductors) and the conductors (generally metals). It has a typical lamellar structure which makes it possible to be applied in photocatalysis [2]. As an n-type semiconductor, it has great electron mobility and is applied in many areas including supercapacitor electrodes, sensors, photodetectors, and thermoelectric devices, due to its reasonably low band gap energy [3,4]. It has also been largely employed in medicine, contrast agent, biomolecular detector, and as photocatalyst [4].

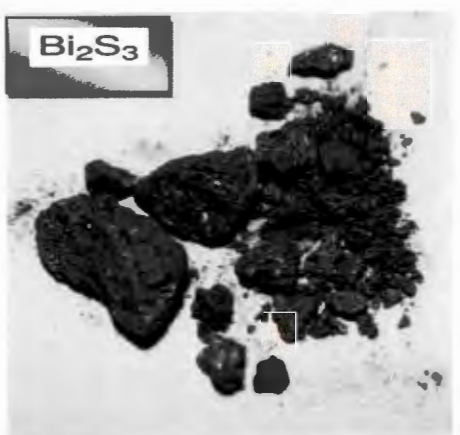

Figure 1.1: Bismuth sulphide (Bi_2S_3) [1].

Bismuth sulphide has a great absorption coefficient range of 104-105 cm^{-1}, and a sensible incident photon to conversion efficiency of (~5%) [5,6]. Its direct band gap energy could be adjusted by varying the particle size and shape, thereby causing some changes in the properties. The band edges fall within the visible solar energy spectrum. Hence, it is a suitable material for solar energy conversion devices [7]. These band edges are also very useful for the separation of charge carriers, and generation of a defect-free interface [4].

1.2. Synthesis of bismuth sulphide nanoparticles

Different methods of synthesis have been reported for the preparation of Bi_2S_3 nanoparticles, thus, resulting into different sizes and morphologies. Such methods include thermal decomposition (hydrothermal or solvothermal methods), biomolecule-assisted pathways and microwave irradiation techniques [8,9]. There are different factors which influence the properties of the prepared Bi_2S_3 nanocrystals; for example, the precursor concentration, molar ratio of Bi to S, reaction temperature and reaction time. These factors ultimately influence the energy-level structure and optical absorption [5]. However, these different properties are the consequences of quantum confinement effect and large surface to volume ratio.

1.3 General background on semiconductors

Semiconductors are materials which have conductivity that lies between the conductor and insulator, such as silicon (Si) and germanium (Ge). They have very few "free electrons" because their atoms are arranged together in a crystalline lattice [10]. These electrons are capable of moving from one level to another, but under certain circumstances. The tendency to conduct electricity could be enhanced by adding specific donor or acceptor atoms into the crystalline structure, thus, producing extra free electrons than holes or the other way round [11]. Figure 1.2 shows the difference between an insulator, a semiconductor and conductor.

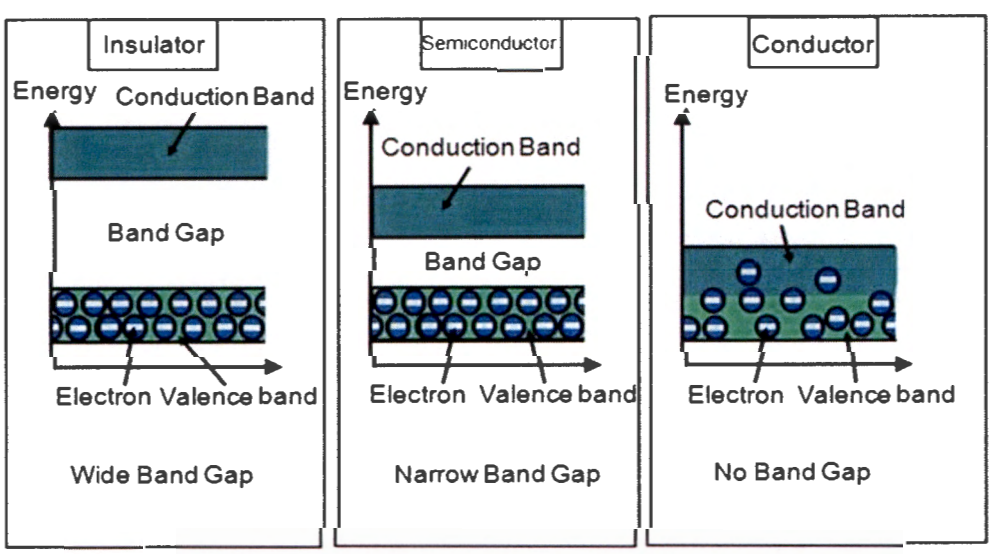

Figure 1.2: Comparison between the insulator, semiconductor and conductor [12].

As shown in Figure 1.2, an insulator has a completely filled bands separated by a considerable energy gap from an unoccupied band. On the other hand, a semiconductor has a very small energy band gap and can be a pure element, such as silicon or germanium, while a conductor has its valence band only partially filled (no band gap) [11,12].

1.4. Classification of semiconductors

Semiconductors may be classified as either intrinsic or extrinsic. The intrinsic semiconductors are very pure semiconductors, which imply the absence of any doping impurities, whereas the extrinsic semiconductors are obtained by doping with impurity atoms [10]. The number of holes in the valence band and the electrons in the conduction band are equal. In extrinsic semiconductors, the pure state of the semiconductor material is diluted by adding small quantities of impurities. There are two types of extrinsic semiconductors: p-type and n-type semiconductors. P-type is when the doped semiconductor contains mostly free holes, and as n-type is when it contains mostly free electrons [13]. This implies that in a p-type semiconductor, the number of holes is much more than the electrons. Holes are the majority charge carrier and electrons form the minority carriers. Similarly, in n-type materials, the number of electrons is much greater than the number of holes. Electrons are the majority carrier whereas holes are the minority carriers [14,15].

1.5 Doping of semiconductor nanoparticles

In the doping process, small amounts of impurities (donor or acceptor atoms) are added to pure semiconductors, thereby causing large changes in the conductivity of the material. Doping is capable of increasing the concentration of charge carriers either by giving out or receiving electrons (receiving electrons leads to the increase in the hole population). As the doped semiconductor is no longer in its pure state, these donor and acceptor atoms are collectively termed as "impurities". Normally, the impurities are referred to as dopants or doping agents and these dopants have energy levels which are close to the edges of the conduction or valence band of semiconductor materials. The doping of semiconductor nanomaterials using transition metals is important since it influences the different properties such as electrical, optical, catalytic, and magnetic potency of the host semiconductor [16]. It is also a strategy to improve the utilization

of solar light for semiconductors, either by modifying the band gap structures or indirectly exchanging the energy.

Band gap modification can be realized by creating impurity levels in the forbidden band of semiconductor or shifting the valence band edge. This method has been successfully employed to extend the light absorption range of some wide band gap semiconductors from UV to visible light with appropriate transition metals or non-metal dopants [17]. Moreover, in doping, the manipulation of the size and shape which is achieved by decreasing the size of a particle to the nanometers level can reduce the electron-hole recombination probability. This is because the electrons and holes do not have to travel a distance which is longer than their diffusion length [18]. However, it is important to point out that this manipulation has its own side effect since it also results in increase in the bandgap.

Semiconductor nanoparticles provide possibility of improving the properties of engineering materials in order to enhance the characteristics of fabricated devices' properties. A gradual changeover from solid state to the molecular structure occurs when the size of the particle reduces. The electronic bands split into discrete energy levels when the size of the particles are suitably small, as the electrons turn out to be quantum confined [19]. Therefore, the nanocrystal size influences the band structure of a material which is semiconducting in nature, and the properties are affected by the reduction incrystal size. So, the band gap of the semiconductor could be adjusted to a required value [18]. The optical emission and absorption properties rely on the transition among these bands. Hence, semiconductors display great changes in their optical properties. Variations in the shapes of semiconductor nanoparticles have an effect on their magnetic and photocatalytic properties [16].

1.6 General background on nanoparticles

Nanoscience is a multi-disciplinary field that combines the knowledge of several areas such as physics, chemistry, biology and engineering. It is a field of science that focuses on the study of materials, whose size is less than 100 nanometers. It also involves the observation of the governing laws of the nanosized objects, developing the theoretical models to explain the features of these nanosized objects and investigating its properties. The characteristics of the

objects are altered when it goes to a nanometer size regime. Hence, the material's physical, chemical and biological properties are different from the ones of micrometer and larger scale particles [20].

Nanoparticles (NPs) belong to a wide class of materials which include particulate substances that have at least one of its dimension less than 100 nm. Subject to the overall shape, they could be 0D, 1D, or 2D [20, 21]. In the nanosize domain, the size of the material can influence the physiochemical properties. For example, the optical behaviour of a 20 nm gold and platinum have characteristic wine red colour and yellowish grey colours respectively. Figure 1.3 shows the variation in colours of Au nanoparticles with difference in sizes and shapes.

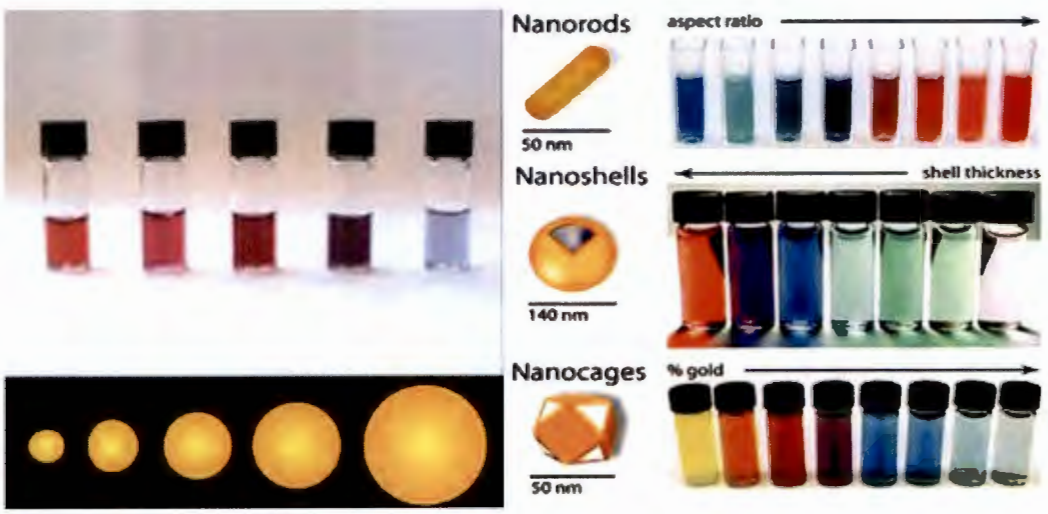

Figure 1.3: Variation in colours of Au nanoparticles with differences in sizes and shapes [22].

1.7 Classification of the nanomaterials

The basic unit of nanomaterials can be divided into three categories: zero-dimensional (0D) which are nanoparticles with all three dimensions in the nanometer size range; one-dimensional (1D) in which examples are nanowires, nanofibers, nanorods, nanotubes and nanoribbons have two dimensions in the nanoscale level; two-dimensional (2D) such as nanoplates and nanosheets have one-dimensional space at nanoscale, and the three-dimensional (3D) [21,23]. Figure 1.4 shows the shapes and structures of 0D, 1D, 2D and 3D nanoparticles.

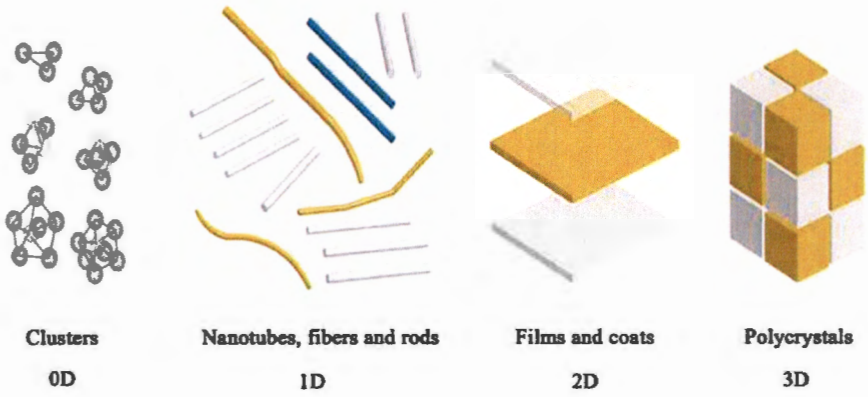

Figure 1.4: Schematic illustration of structural dimensionality of materials with expected properties [23].

Nanoparticles may be composed of three layers. These include firstly the surface layer. This part may be functionalized with a variation of molecules, metal ions, surfactants and polymers; the second layer is the shell layer. This part is, in all aspects, a chemically different material from the core. The third layer is the core, which is principally the central portion of the nanoparticles and is usually referred to as the nanoparticle itself [22,24]. Due to such extraordinary properties, these materials have fascinated immense interest of researchers across many fields.

There are two principal factors which are responsible for the significant difference in the properties of nanomaterials compared to their bulk materials. They are the size effects and quantum confinement effects. These factors can alter or enhance material properties such as reactivity, strength and electrical characteristics. Quantum confinement is the spatial confinement of electron-hole pairs (excitons) in one or more dimensions within a material. It is more prominent in semiconductors because they have energy gap in their electronic band structure. On the other hand, surface effect describes the presence of a greater proportion of atoms at the surface compared to those inside as a particle size decreases [25].

1.8 Photocatalytic activity

Photocatalysis is a process which involves the initiation and acceleration of photoreaction upon the irradiation of light in the presence of a photocatalyst. It is a substance that promotes reactions by absorbing light without being altered itself, before or after the reaction [18]. By making use of the energy of absorbed photons, photocatalysis can be carried out in a wide variety of vital chemical processes. Areas of application include environmental remediation by the destruction of organic pollutants for purification of water or air, and in the production of solar fuels. The later involves the generation of fuels, hydrogen from water or methane/methanol from CO_2 [26]. Materials which are semiconducting in nature can be utilized in photocatalysis as particle dispersions or in photoelectrochemical mode. Using TiO_2, which is a common semiconductor photocatalyst, the typical mechanism of photocatalysis is presented in Figure 1.5.

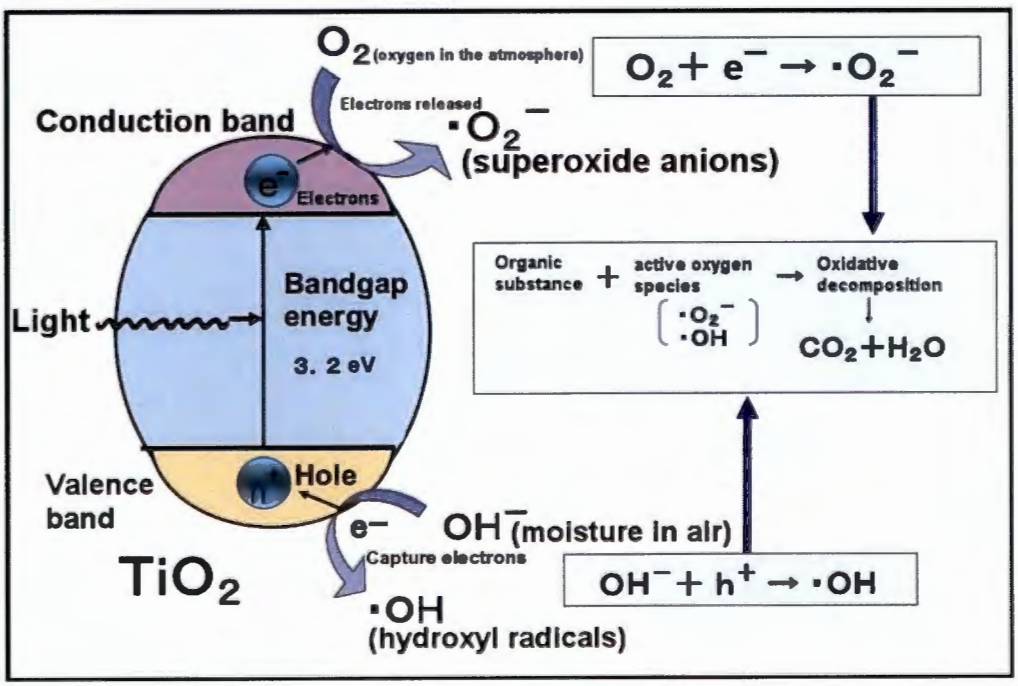

Figure 1.5: Mechanism of photocatalysis by oxidative decomposition [27].

In the process of photocatalysis, the absorption of light by a photocatalyst initiates the excitation of electrons present in the valence band (VB) to migrate to the conduction band (CB); thus, leaves the positive holes in the VB. Consequently, the electrons and holes which have been photogenerated are transferred to the surface of the semiconductor, and this trigger a series of

redox reactions. In general, thermal catalysis is restricted to spontaneous reactions ($\Delta G < 0$). Nevertheless, for photocatalysis both the spontaneous and non-spontaneous reactions are possible. These results in the oxidative degradation of organic compounds and the reduction of water and CO_2, respectively [28,29]. In the case of non-spontaneous reactions, light acts as the source of energy which is transformed into chemical energy that is gathered in the reaction products.

1.9 Morphology and structural properties for photocatalytic activity

The chemical and physical performance of nanostructured semiconductors could be tailored by three structural parameters, which are size, morphology and defect. The photocatalytic activity of semiconductor catalysts could also be distinctively mediated by these three structural parameters. The size dependence of semiconductor electronic structure provides an effective modulation of band narrowing and the subsequent changes in band gap energy. As the morphology and structural properties are controllable, improved photocatalytic performance could be achieved by synthesizing specific low dimensional nanostructures and assembling their orientated hierarchical structures, which would provide more reactive sites, high mass transfer rate and good light harvest to semiconductor catalysts. More recently, by controlling the dominance of high energy facets and structural irregularities such as edges and corners, crystal-facet engineering emerges as a good tool to finely tune the physicochemical properties of catalysts, further leading to the unprecedented selectivity and activity for photocatalysis [8, 18]. This is achieved by controlling the dominance of high-energy facets and structural irregularities such as edges and corners.

1.10 Strategies for improving photocatalytic activity

To improve the activity of a photocatalyst, it is important to first explore and understand the chemistry of the process. According to the classical quantum theory, a typical photocatalysis process is triggered by the absorption of light with the irradiation of photo energy which is equal to or greater than the band gap energy of the semiconductor (SC) photocatalyst. This would

subsequently inject electrons into the conduction band (CB) and, thus, leave the same quantity of holes in the valence band [30,31] (VB), as illustrated in Eq. (1).

$$SC\ h\nu \rightarrow SC\ (e^-_{CB}, h^+_{VB}) \quad (1)$$

The occurrence of charge separation, through the formation of electron-hole pair is the first step of photocatalysis, which is called photo excitation. This phenomenon is extremely fast occurring in few to second. The second step involves the transfer of the photo-excited electron–hole pairs to the surface of the semiconductor. The transfer of electrons and holes always competes with other phenomena such as the trap (e.g., shallow traps and deep traps) and relaxation of charge carriers, and the recombination of electrons and holes. All of these three phenomena would significantly hinder the transfer of charge carriers by squandering accessible light energy in the forms of heat and light, as illustrated in Eq. (2) [30,32].

$$SC(e^-_{CB}, h^+_{VB}) \rightarrow SC + \text{energy} \quad (2)$$

The excited electrons and holes on the surface of semiconductor initiates a redox reaction with electron donors (D) and electron acceptors (A), and then induce surface chemistry, which is the third step of photocatalytic cycle. The generated primary redox intermediate products, namely reactive free radicals, take the photodegradation of organic dye for instance, they would be trapped and react with pollutant molecules so as to implement the photocatalytic cycle, as illustrated in equation (3) and (4).

$$A^{\bullet+} + \text{pollutant} \rightarrow \text{degradation products} + A_{red} \quad (3)$$

$$D^{\bullet-} + \text{pollutant} \rightarrow \text{degradation products} + D_{ox} \quad (4)$$

Thus, to enhance the photocatalytic activity of nanomaterials, several key parameters should be taken into account including light response, light energy utilization, transfer speed of charge carries, separation efficiency of charge carriers and active sites. In view of those basic principles, considerable work has been carried out in order to improve the photocatalytic activity of bismuth-related nanomaterials in the past decades. In this work, morphology modulation is considered as a practical strategy. Here, photocatalysis could, on one hand, have more reactive sites and easier electron-hole transfer. On the other hand, it may be endowed with more primary

active species. It is also found that some bismuth-related nanomaterials with specific size and structure show better light absorption which facilitates the photo-induced charge separation. An important approach which has been widely reported for the improvement of the photocatalytic activity of bismuth compounds is doping. Strategies such as composition and doping improve the photoactivity of nanomaterials by widening the photo response range, thereby facilitating charge carriers' transfer and inhibiting electron–hole recombination [18,30].

1.2 Problem statement

Rapid industrialization and high population growth has resulted in the increase in different activities to the detriment of the environment. In recent times, due to increased industrial activities, larger volumes of effluents are discharged into the surrounding water without any treatment, thus creating water pollution. Different textile, dyeing and printing industries discharge their waste-water into nearby water resources as shown in a Figure 1.6. However, this coloured water is quite harmful and also, sometimes, toxic in nature [33].

Figure 1.6:Water pollution by different industrial effluents [34-36]

Thus, environmental pollution is a major challenge and a great problem for our society that seriously threatens human health and the existence. With the increase in environmental pollution, lots of attention has been devoted to photocatalysis for the remedial action of highly polluted environment. Researchers have used different oxides and sulphide-based semiconductors as photocatalysts for degrading the dyes. For example, TiO_2 semiconductor has been utilised for the photodegradation of surfactants from waste-water [29,36]. The removal and recovery of mercury from water has also been achieved by photocatalysis, in addition to the new technologies involving photo-induced water splitting using semiconductor photocatalysts.

Several treatment technologies have been developed for the decolourization and degradation of dyes in waste-water pollutants. These technologies are classified according to the principle of remediation into (1) physical methods, such as adsorption, reverse osmosis, ultrafiltration and ion exchange, (2) chemical methods, such as chlorination and ozonation, and (3) biological methods, such as aerobic and anaerobic treatments [33, 37]. Most of these techniques remove pollutants by transferring them from one phase to another without converting them into

environmentally friendly end products. Therefore, they create another contaminated material, which requires further treatment and hence, adds an extra cost to the overall degradation process [34]. Some of these treatment techniques also have challenges in terms of cost effectiveness, non-environmentally friendly and poor efficiency. Advanced oxidation processes (AOPs) such as Fenton, photo-Fenton catalytic reactions, UV/H_2O_2 and UV/O_3 have proved to be sufficiently effective alternatives for the treatment of waste-waters containing dyes [37,38].

1.3 AIM AND OBJECTIVES

1.3.1 Aim

The aim of this work is to prepare pure Bi_2S_3 and metal doped Bi_2S_3 nanomaterials with different morphologies for improved photocatalytic degradation of a dye in polluted water.

1.3.2 Objectives

The aim of this study would be accomplished through the following objectives:

- synthesis of novel bismuth complexes (4-methyl-phenyldithiocarbamates, N-phenyldithiocarbamate and N-benzyldithiocarbamate) as single source precursors and their characterization,
- preparation of bismuth sulphide nanoparticles using solvothermal and microwave methods, and their characterization,
- preparation of Mn(II) and Sn(IV) doped Bi_2S_3 nanoparticles using hydrothermal method and their characterization,
- conduction of photocatalytic studies of the Bi_2S_3 and doped Bi_2S_3 nanoparticles using methylene blue as a common pollutant.

REFERENCES

[1] C. Ye, G. Meng, Z. Jiang, Y. Wang, G. Wang, L. Zhang, J. Am. Chem. Soc. 124 (2002) 15180.

[2] B. Sun, Z. Qiao, K. Shang, H. Fan, S. Ai, Mater. Lett. 91 (2013) 142.

[3] G. Konstantatos, L. Levina, J. Tang, E.H. Sargent, Nano Lett. 8 (2008) 4002.

[4] A. Helal, F.A. Harraz, A.A. Ismail, T.M. Sami, I.A. Ibrahim, Mater. Des. 102 (2016) 202.

[5] S.K. Dutta, S.K. Mehetor, N. Pradhan, J. Phys. Chem. Lett. 6 (2015) 936.

[6] N. Saha, A. Sarkar, A.B. Ghosh, A.K. Dutta, G.R. Bhadu, P. Paul, B. Adhikary, RSC Adv. 5 (2015) 88848.

[7] B. Pejova, I. Grozdanov, Mater. Chem. Phys. 99 (2006) 39.

[8] P.R.R. Mesquita, J.S. Almeida, L.S.G. Teixeira, A.F. Da Silva, L.A. Silva, J. Braz. Chem. Soc. 24 (2013) 280.

[9] S. Ranjitha, G. Rajarajan, J. Marimuthu, S. Natarajan, S. Vadivel, Int. J. Sci. Res. (2014) 9.

[10] R.F. Khairutdinov, Russ. Chem. Rev. 67 (1998) 109.

[11] D. Klimm, IUCrJ. 1 (2014) 281.

[12] E.P. Wagner, J. Chem. Educ. 93 (2016) 1289.

[13] L. Tolbert, B. Ozpineci, 5 (2003) 1.

[14] L.M. Tolbert, B. Ozpineci, S.K. Islam, M.S. Chinthavali, P. Electronics, E. Machinery, O. Ridge, O. Ridge, 25 (2005.) 3.

[15] K. Shenai, R.S. Scott, B.J. Baliga, IEEE Trans. Electron Devices. 36 (1989) 1811.

[16] N. Anasane, R. Ameta, Mater. Sci. Pol. 35 (2017) 6.

[17] W.W. Anku, S.O.B. Oppong, P.P. Govender, Bismuth - Adv. Appl. Defects Charact. (2018)

[18] L. Zhang, M. Jaroniec, Appl. Surf. Sci. 430 (2018) 2.

[19] H. Zhao, F. Tian, R. Wang, R. Chen, Rev. Adv. Sci. Eng. 3 (2014) 3.

[20] A.P. Nikalje, Med. Chem. 5 (2015) 81.

[21] J.N. Tiwari, R.N. Tiwari, K.S. Kim, Prog. Mater. Sci. 57 (2012) 724.

[22] E.C. Dreaden, A.M. Alkilany, X. Huang, C.J. Murphy, M.A. El-Sayed, Chem. Soc. Rev. 41 (2012) 2740.

[23] E. Moustafa, A. Noah, K. Beshay, L. Sultan, M. Essam, O. Nouh,World J. Eng. Techn. 3 (2015) 116.

[24] I. Khan, K. Saeed, I. Khan, Arab. J. Chem. 31 (2017) 6.

[25] S. Chaturvedi, P.N. Dave, N.K. Shah, J. Saudi Chem. Soc. 16 (2012) 307.

[26] S.C. Roy, O.K. Varghese, M. Paulose, C. a Grimes, ACS Nano. 4 (2010) 1259.

[27] A. Ibhadon, P. Fitzpatrick, Catalysts. 3 (2013) 189.

[28] N. Shaham-Waldmann, Y. Paz, Mater. Sci. Semicond. Proc. 42 (2016) 72.

[29] C. Byrne, G. Subramanian, S.C. Pillai, J. Environ. Chem. Eng. 6 (2018) 3531.

[30] E. Karamian, S. Sharifnia J. CO_2 Util. 16 (2016) 194.

[31] M. Tahir, N.S. Amin, Energy Convers. Manag. 76 (2013) 194.

[32] G. Palmisano, V. Augugliaro, M. Pagliaro, L. Palmisano, Chem. Commun. (2007) 3425.

[33] A. Azizullah, M.N.K. Khattak, P. Richter, D.P. Häder, Environ. Int. 37 (2011) 479.

[34] T. Robinson, G. McMullan, R. Marchant, P. Nigam, Bioresour. Technol. 77 (2001) 247.

[35] A. Bhatnagar, A.K. Jain, J. Colloid Interface Sci. 281 (2005) 49.

[36] S. Sharma, R. Ameta, R.K. Malkani, S.C. Ameta, Maced. J. Chem. Chem. Eng. 30 (2011) 229.

[37] H. Kisch, N. Serpone, E. Pelizzetti, John Wiley & Sons, Inc, 4 (1989) 1.

[38] U. M. Gaya and A. H. Abdullah, J. Photochem. Photobio. 9, (2007) 1.

CHAPTER 2

2.0 LITERATURE REVIEW

Bismuth sulphide is an important class of semiconductor with very rich properties. It owes its wide application to its unique properties. The development of nanotechnology and the interesting properties of materials in nano size regime have further accentuated the research interest in bismuth sulphide nanoparticles. Diverse morphologies of Bi_2S_3 have been reported such as nanotubes, nanowires, nanoribbons, nanoflowers, microbelts, snowflake-like nanostructures and self-supported arrangements of radially associated one-dimensional (1D) nanostructures [1]. These nanomaterials have been prepared through various synthetic methods such as single-source precursor approach, hydrothermal/solvothermal process, and microwave-assisted solvothermal technique. Some of these methods will be highlighted.

However, these applications are limited when in the bulk stage and can be enhanced by their size dependant properties when in the nanometre dimension. Different methods can be employed for the conversions of materials from their respective precursor complexes to the nanoscale dimension solvothermal decompositions of precursors are generally preferred for nanoparticle synthesis. In this process, the solvents serve the duo purpose of acting as both the heat sink and capping agents. The solvothermal single source precursor approach involves the use of a single complex which bears both the metal and the anion of interest [1]. This method has many advantages over others: the presence of the bridging and chelating organic ligands can give rise to monodispersed nanoparticles which acquire some important structural properties from the precursor compounds. It allows intimate interactions between the molecules leading to homogenous distribution of the metal ion, thereby preventing molecular aggregation. The reaction occurs under relatively mild reaction conditions and the organic molecules are very volatile giving rise to pure and metastable phases [2].

A lot of research has been focused on microwave assisted synthesis of Bi_2S_3, resulting in series of different dimensionalities and morphologies. For example, bismuth sulphide nanorods and urchin-like morphologies synthesised by microwave irradiation in the presence of surfactants and in ionic liquids have been reported [3-7]. Lu *et al*, reported some microcrystalline Bi_2S_3 with three-dimensional (3D) flower-like superstructures synthesised by microwave method [8]. By

using microwave assisted solvothermal technique, Wen-hui Li reported the synthesis of some bismuth sulphide (Bi_2S_3) nanowires [9]. Despite the success of these microwave procedures, most of them involved the use of dual source: bismuth salt as bismuth source and sulphur containing compounds as sulphur source. However, the use of sulphur sources such as thiourea, thioacetamide and sodium sulphide prompts various health and environmental risks [10]. Such concerns could be overcome using single source precursor molecules. In addition to the environmental issues, the decomposition of single source precursors has other synthesis benefits over the binary systems because the proximity and fixed geometry of the elements in the single source precursor molecule may give greater control and tenability to the reaction [11].

2.1 Bismuth sulphide by microwave synthetic route

The microwave route to nanomaterials synthesis exhibits many advantages such as effectiveness, economic and environmental friendliness [2,3]. It was discovered in 1986, and has since been established to be an efficient heating process. The microwave synthesis process is very fast, and in addition to its simplicity, it has advantages over other conventional methods. Some of the advantages include shorter reaction time, production of small particle sizes with narrow size distribution and phases with high purity [4,5]. In reported studies, bismuth sulphide (Bi_2S_3) nanorods have been obtained under microwave irradiation process using precursors and solvents. Surfactants which are microwave active such as polyvinyl pyrrolidone, potassium oleate, and ethylene diaminetetraacetic acid have been used to prepare Bi_2S_3 [3,6]. A gelatine solution was used as capping agent in a microwave assisted green process to prepare Bi_2S_3nanorods. The crystal phase, optical properties, as well as the morphological evolution processes of the as-synthesized Bi_2S_3 were reported [7].

Wu *et al,* reported a large-scale microwave assisted synthesis of highly crystalline Bi_2S_3 nanorods from a solution of bismuth citrate and thiourea. The microwave irradiation route reduced the reaction time by at least 80% compared to other methods. By changing various experimental parameters, including the capping agent, time, reaction solvent, ratio of reactant, bismuth and sulphur precursor, different shapes and sizes of Bi_2S_3 nanostructures were also obtained [8]. A microwave assisted synthesis of Bi_2S_3nanorods in ionic liquid has been reported [9].The ionic liquid played a vital role in the shape and size of the prepared Bi_2S_3.

Microcrystalline bismuth sulphide (Bi_2S_3) with three-dimensional (3D) flower-like structures obtained via microwave irradiation of a solution of bismuth nitrate ($Bi(NO_3)_3 \cdot 5H_2O$) and thiourea ($(NH_2)_2CS$) in ethylene glycol have also been reported [3].

A microwave-assisted solvothermal method has been devised for the controlled preparation of bismuth sulphide nanowires. Li reported one-dimensional (1D) bismuth sulphide (Bi_2S_3) nanowires using $Bi(NO_3)_3$ and Na_2S in absolute ethanolic solution by microwave-assisted solvothermal method [10]. The microwave synthesis had the capacity to produce nanowires or spheres of Bi_2S_3 without the use of any capping molecule, but the control of the shape of the metal sulphides was a key issue to deal with. In earlier reports, different shapes of surfactant-free Bi_2S_3 including fibers, rods or hedgehogs in their nano dimensions, were obtained by microwave-assisted method using different salts of bismuth. The possible formation mechanisms of the nanofibers or "urchins" were also reported [11].

Different factors such as type of solvent, the solution pH, temperature, and concentration of solution were factors that could influence the size and properties of the nanomaterial. Similarly, the reaction time also affects the yield but not the shape of Bi_2S_3 obtained by microwave heating [8]. The synthesis of Bi_2S_3 using different sulphur sources has been reported, and the influence of the type of bismuth sources on the morphology and purity of the products was studied [4,5,8]. Bismuth sulphide with different shapes was prepared using bismuth nitrate pentahydrate ($Bi(NO_3)_3 \cdot 5H_2O$) and two types of sulphur sources (methyl thiourea and thiourea) in different solvents of water and glycolsby a microwave irradiation approach at 180 W and for 20 min [4].

2.2 Bismuth sulphide by hydrothermal route

Hydrothermal synthesis is a route for preparing nanomaterials from an aqueous solution in an autoclave at high temperature and pressure. It is a rapid technique which has the advantage of high product yields. The method allows particle size and shape to be controlled by changing one of the processing variables. Its main challenge is the removal of the products from the solution and at same time avoiding particle agglomeration. Hence, steric stabilizing reagents are added or freeze drying of the suspensions is carried out to avoid this problem [12].

The hydrothermal method of synthesis has many advantages and it is environmentally friendly, less expensive and allows for the reduction of free energies for various equilibria[13]. Zhu *et al.*

prepared Bi_2S_3 nanostructures which includes sub-microtubes, nanoflowers and nanorods by hydrothermal method using urea-assisted processes at a low temperature [14]. A hydrothermal approach was devised to prepare Bi_2S_3 with various shapes (nanoparticles, nanoflaked flowers and nanothornycolumn) using bismuth(III) monosalicylate and three different types of sulphur sources [L-cysteine, thiourea and thioacetamide] as precursors. The influence of the reaction conditions was studied and possible formation mechanism for the various Bi_2S_3 nanostructures was proposed [15]. A mild hydrothermal route has been reported by Yang *et al*, for the synthesis of metal sulphides which used thioglycolic acids (TGAs) as nontoxic template [16]. The use of thioglycolic acid (TGA) as both a sulphur source and stabilising agents facilitated the formation of the star shaped morphology [17].

A simple hydrothermal reaction involving bismuth nitrate and thioglycolic acid (TGA) has yielded nanoparticles of different morphologies at relatively low temperature. The effect of variables such as reactant concentration, molar ratio of TGA to the bismuth nitrate, temperature and time of reaction on the particle shape, sizes and phases of nanocrystalline Bi_2S_3 products was studied[18]. Orthorhombic structure bismuth sulphide nanorods have been synthesized through hydrothermal method by Helal *et al.* The presence of water in the reaction system and the hydrothermal process parameters were factors reported to play key roles in the development of high aspect ratio nanorods[19].

Key variable factors such as the Bi/S molar ratio, time and temperature of reaction greatly influence the structural morphologies of Bi_2S_3 [20]. A surfactant hydrothermal process has been devised for the preparation of single-crystalline bismuth sulphide (Bi_2S_3) nanorodsusing triethanolamine as an agent of complexation for the Bi^{3+} ions and elemental sulphur(as the sulphur source), solubilized in monoethanolamine [19].

2.3 Bismuth sulphide by single source precursor synthetic route

The single source precursor (SSP) approach implies that all the constituent elements required in the nanomaterial can be incorporated into one compound. The compound is then utilized as a precursor for the desired product. Thermal decomposition (thermolysis or pyrolysis) of single source precursors are proven to provide easier and simpler control of the shapes and sizes, and growth of high quality nanoparticles in large scale production [21,22]. This route is one of the

most commonly used methods as it affords stable monodispersed colloidal quantum dots whose size distribution could be approximately ~5%. Compared to other routes which require exact control over stoichiometry, the SSP routes offer mildness, safety and the fabrication procedure is very simplified [23].

Different morphologies of nanostructured bismuth sulphide (Bi_2S_3) have been prepared successfully using the single source precursor route. Tian *et al.* prepared Bi_2S_3nanomaterials with different morphologies, such as nanorods, nanoleaves, dandelion-like nanostructure, nanoflowers and nanocabbages using [$Bi(SCOPh)_3$] as single-source precursor [24]. Metal dithiocarbamate has been widely studied as single source precursor for the preparation of metal sulphide [12,22,25]. Bismuth *N*-ethyl cyclohexyldithiocarbamate has been used as single-source precursor for the synthesis of bismuth sulphide by the thermal decomposition route at 400 °C [26]. The bismuth dithiocarbamate precursor was calcined for different durations. The optical, structural, and compositional properties of the obtained bismuth sulphide were also studied.

2.4 Metal doped bismuth sulphide

Doping is capable of increasing the concentration of charge carriers by donating or accepting electrons. Since the doped semiconductor has now lost its purity as a result of the introduction of a foreign material, these donor and acceptor materials are sometimes referred to as "impurities". Normally, the impurities are referred to as dopants or doping agents.

Different transition metal doped bismuth sulphide semiconductor nanoparticles have been reported. For example, manganese(Mn^{2+}) doped Bi_2S_3 nanoparticles of different morphologies containing polyoxyethylene 100 stearate (as capping agent), have been synthesized by a simple wet chemical technique by Anasane and Ameta [27]. The introduction of a suitable metal ion, such as Mn^{2+}, into a substrate such as a semiconductor host material reduces the band gap energy of the semiconductor. The result is a faster movement of electrons between the conduction and valence band.Many applications utilized in nanoelectronic devices are based on this property [28]. A simple synthesis of Eu-doped Bi_2S_3 NPs, in various ratios, through the breakdown of dual single source precursors: Bi(III) dithiocarboxylate and Eu(III) dithiocarboxylate complexes has been reported using a simple solvothermal technique [29,30].

Microspheres of tin-doped Bi_2S_3 (TDBs) composed of nanosheets was synthesized using an easy one step solvothermal route, and a viable formation mechanism was reported. The results showed nanosheets which consist of tin-doped Bi_2S_3 with a bit of Sn^{4+} substitution at Bi^{3+} sites within the Bi_2S_3 lattice [31]. Silver doped bismuth sulphide ($AgBiS_2$) nanoparticles have been reported by single source precursor approach using bismuth diethyldithiocarbamate as the sulphur precursor under reflux condition in presence of hexadecylamine [32]. The long chain amine acted as both the capping agent as well as shape directing coordinating solvent because it has been shown to control the rate of particle growth and size when used as a capping agent [13].

2.5 Common dyes in photocatalytic studies

Common dyes used in photocatalytic experiments are: Rhodamine B and Methylene Blue (cationic) and Acid Orange 7 (anionic). For non-color compounds, chlorophenols, dichloroacetic acid, nitrobenzene, aniline and formic acid are commonly used. Methylene blue (MB) is one of the most common dyes used in the industry, which causes the most pollution in water, hence has been chosen as the dye of interest in this study.

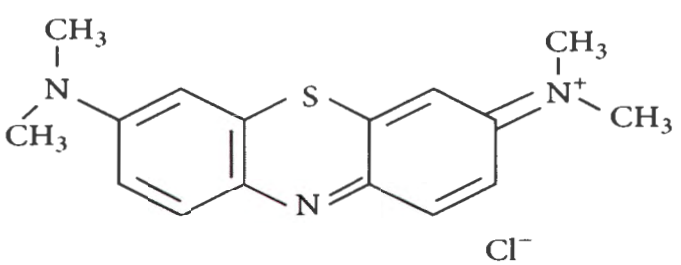

Figure 2.1: Methylene blue dye structure

Methylene blue (MB) is a basic dye, which is normally used for dyeing wool and silk. It is also used for medical purposes to inspect some diseases. Discharging of waste-water pollutants, contaminated with MB, to feed water resources, such as rivers, lakes, and seas without efficient degradation results in harmful effects, like burns of eye, nausea, vomiting, and diarrhoea [33]. The removal of the colour of waste-water is a burning issue all over the world, as it creates water pollution. Therefore, finding an effective treatment method for waste-water containing dyes has become an important research goal. Dyes are one of these harmful organic pollutants and are

released mainly from the textile and painting industries to the Environment [34]. When these dyes hydrolyse and react with other pollutants present in the wastewater effluents, they produce lethal carcinogenic by products, which not only threaten the aquatic environment but also the health and wellbeing of human. Photocatalytic degradation of pollutants by semiconductors is a new and effective technique for their removal from effluents of industries.

Water has a broad impact on all aspects of human life including livestock's but not limited to health, food, energy, and economy. Every each person on Earth requires at least litres of clean and safe water to drink, cook and also keeping themselves clean. Moreover, to the environmental, economic, and social impacts of poor water supply and sanitation [33], the supply of fresh water is essential for the safety of human being. Therefore, it is important to have clean and safe water for the environment. Methylene blue (MB) was used as a model pollutant in this work in order to evaluate the photocatalytic performance of the Bi_2S_3 in aqueous solution using irradiation time as variable parameter.

2.6 Photocatalytic property of Bi_2S_3 nanoparticles and its composites

Organic dyes, especially azo dyes such as methyl orange (MO), have been reported to possess high cytotoxicity for the mammalian tissues [35]. It is very difficult to decompose such dyes by natural processes. Under light irradiation, semiconductor-based photocatalystscan effectively decomposed dyes. This occurs when the semiconductors are irradiated with the photon whose energy is higher or equal to the photocatalyst's band gap energy [36].

There are many factors which can affect the performance of photocatalysts. Such factors include the exposed crystal faces, specific surface area, morphology and the particle's structure. One of the efficient ways to increase the photoactivity of photocatalysts is by the control of the particle's morphology and properties like the surface and bulk crystal structure. Composites synthesized by bismuth subsalicylate serving as the bismuth source. The photocatalytic activity of one-dimensional (1D) belt-like Bi_2S_3/BiOCl composites, obtained via a simple one-pot solvothermal route, has been evaluated by studying the catalytic degradation of salicylic acid (SA) and Rhodamine B (RhB) under the irradiation of visible light [37]. It was demonstrated that the coupling of Bi_2S_3/BiOCl composites enhanced the photocatalytic activity when compared with

Bi_2S_3 and BiOCl [38,39].The same composites when obtained as three-dimensional (3D) flower-like hierarchical microspheres and as two-dimensional 2D plate-like nanostructure also showed improved photocatalytic properties when tested for the degradation of 2, 4-dichlorophenol and methyl orange [40].

A photocatalyst was effectively synthesized by the combination of the rational heat-treatment process and ion exchange technique. A successful synthesis of $Bi_2S_3/Bi_2O_3/Bi_2O_2CO_3$ composite has been reported which exhibited superior photocatalytic degradation of formaldehyde under visible light irradiation. The composite also showed good photocatalytic activity for methyl orange and phenol, in addition to good stability [41]. The highly improved activity of the composites could be attributed to the increased light absorption and effective charge separation.

Bi_2S_3 could act as a sensitizer as a result of its ability to absorb visible light with wavelength up to 800 nm [42]. The nanocomposites of Bi_2S_3/SnS_2 heterostructure (synthesized by combining the hydrothermal growth method and a facile in situ growth method) have been applied for the breakdown of organic dye MO under visible light radiation [43].

2.7 Photocatalytic property of metal doped Bi_2S_3 nanoparticles

Doping of group II-VI nanocrystals with active luminescent centre and controlled grain size has been shown to produce new opportunities with wide applications in field such as photovoltaic cells, photodetectors, and photo degradation of organic pollutants under the illumination of visible and UV light [44]. Jiang *et al,* reported the photocatalytic activities of tin doped Bi_2S_3 (TDBs). Tin(IV) is an inexpensive and simple metal ion to obtain. It is a doubly-ionized donor as it can afford donor ion, increase higher electron carrier content and can immensely alter the band gap and the optical characteristics of photocatalysts [31]. In addition, it can enhance the specific surface area and range of light response. The enhanced photocatalytic activities of the TDBs might be attributed to the prevention of the recombination of photogenerated electrons and holes by the dopant Sn [31].

The photocatalytic properties of the synthesized Bi_2S_3 nanomaterials was evaluated by studying the decolourization of methyl violet dye, and also the electron transfer reaction in sodium thiosulphate (STS) and potassium ferricyanide (PFC). The activity of the Bi_2S_3 nanoparticles was

established to have occurred under UV light assisted reaction, leading to the decolourization of methyl violet dye and which also accelerated the redox reaction of $Fe(CN)_6^{3-}$and $S_2O_3^{2-}$[27]. An improved photocatalytic activity of europium doped Bi_2S_3 nanoflowers for the degradation of organic pollutants under visible light has been reported [38]. Eu^{3+} can be doped into the Bi_2S_3 moiety under ambient conditions because its ionic size is closer to that of Bi^{3+} [45]. Therefore, doping of Bi_2S_3 with europium would be an effective way to improve the photocatalytic activity. The photocatalytic efficiency of the Eu doped Bi_2S_3 nanoparticles were evaluated by observing the degradation of methylene blue (MB) in aqueous solution under visible light. The rate of photo enhanced degradation of MB increased with an increase in the concentration of the dopant ion.

Selenium has been doped into Bi_2S_3 to prepare a series of photocatalysts with improved activity. The Se-doped Bi_2S_3 showed high photocatalytic activity in the degradation of methylene blue under visible-light irradiation ($\lambda > 400$ nm). The effects of different Se contents, synthesis time, temperatures, among others, on the photocatalytic activity were reported. The activity of the Se-doped Bi_2S_3 was higher than that of undoped Bi_2S_3 nanoparticles [46]. The effect of interstitial doping of Cu into MoS_2/Bi_2S_3 photocatalysts has also been reported [47]. The as-prepared Cu-MoS_2/Bi_2S_3 photocatalysts were evaluated for photocatalytic activity under the irradiation of simulated solar light. The samples which contained varying concentration of Cu were applied in the photocatalytic splitting of water to generate hydrogen under the simulated solar light irradiation.

REFERENCES

[1] W. Tu, H. Liu, Chem. Mater. 12 (2000) 564.

[2] C. Ye, G. Meng, Z. Jiang, Y. Wang, G. Wang, L. Zhang, J. Am. Chem. Soc. 124 (2002) 15180.

[3] J. Lu, Q. Han, X. Yang, L. Lu, X. Wang, Mater. Lett. 61 (2007) 2883.

[4] T. Thongtem, A. Phuruangrat, S. Wannapop, S. Thongtem, Mater. Lett. 64 (2010) 122.

[5] X.-H. Liao, H. Wang, J.-J. Zhu, H.-Y. Chen, Mater. Res. Bull. 36 (2001) 2339.

[6] Q. Li, M. Shao, J. Wu, G. Yu, Y. Qian, \Inorg. Chem. Commun. 5 (2002) 933.

[7] B. Xue, T. Sun, F. Mao, J. Xie, Mater. Lett. 122 (2014) 106.

[8] J. Wu, F. Qin, G. Cheng, H. Li, J. Zhang, Y. Xie, H.J. Yang, Z. Lu, X. Yu, R. Chen, J. Alloys Compd. 509 (2011) 2116.

[9] Y. Jiang, Y.J. Zhu, J. Phys. Chem. B. 109 (2005) 4361.

[10] W. hui Li, Mater. Lett. 62 (2008) 243.

[11] E.B. Díaz-Cruz, O.A. Castelo-González, C. Martínez-Alonso, Z. Montiel-González, M.C. Arenas-Arrocena, H. Hu, Mater. Sci. Semicond. Process. 75 (2018) 311.

[12] M. Madankumar, D.Sivakumar, S.Premkumar, M. Manivannan, R.M. Mohamed,J Emer Tech Inn Res, 5 (2018) 886.

[13] F. Soofivand, M. Salavati-Niasari, F. Mohandes, Mater. Lett. 98 (2013) 55.

[14] M. Salavati-Niasari, Z. Behfard, M. Maddahfar, J. Ind. Eng. Chem. 20 (2014) 4066.

[15] G. Zhu, P. Liu, Cryst. Res. Technol. 44 (2009) 713.

[16] H. Zhang, D. Yang, S. Li, Y. Ji, X. Ma, D. Que, Nanotechnology. 15 (2004) 1122.

[17] A.M. Qin, Y.P. Fang, W.X. Zhao, H.Q. Liu, C.Y. Su, J. Cryst. Growth. 283 (2005) 230.

[18] M. Salavati-Niasari, D. Ghanbari, F. Davar, J. Alloys Compd. 488 (2009) 442.

[19] A. Helal, F.A. Harraz, A.A. Ismail, T.M. Sami, I.A. Ibrahim, Appl. Catal. B Environ. 213 (2017) 18.

[20] A. Helal, F.A. Harraz, A.A. Ismail, T.M. Sami, I.A. Ibrahim, Mater. Des. 102 (2016) 202.

[21] I. Jen-La Plante, T.W. Zeid, P. Yang, T. Mokari, J. Mater. Chem. 20 (2010) 6612.

[22] D.C. Onwudiwe, P.A. Ajibade, Int. J. Mol. Sci. 12 (2011) 5538.

[23] Y.C. Zhang, G.Y. Wang, X.Y. Hu, J. Alloys Compd. 437 (2007) 47.

[24] L. Tian, H.Y. Tan, J.J. Vittal, Cryst. Growth Des. 8 (2008) 734.

[25] G. Xie, Z.P. Qiao, M.H. Zeng, X.M. Chen, S.L. Gao, Cryst. Growth Des. 4 (2004) 513.

[26] N.H. Abdullah, Z. Zainal, S. Silong, M.I.M. Tahir, K.B. Tan, S.K. Chang, Thermochim. Acta. 173 (2016) 33.

[27] N. Anasane, R. Ameta, Mater. Sci. Pol. 35 (2017) 6.

[28] N. Dixit, N. Anasane, M. Chavda, D. Bodas, H.P. Soni, Mater. Res. Bull. 48 (2013) 2259.

[29] A. Sarkar, A.B. Ghosh, N. Saha, A.K. Dutta, D.N. Srivastava, P. Paul, B. Adhikary, Catal. Sci. Technol. 5 (2015) 4055.

[30] A.K. Dutta, S.K. Maji, K. Mitra, A. Sarkar, N. Saha, A.B. Ghosh, B. Adhikary, B Chem. 192 (2014) 578.

[31] X. Rong, F. Qiu, J. Rong, J. Yan, H. Zhao, X. Zhu, D. Yang, J. Solid State Chem. 230 (2015) 126.

[32] Y.Q. Yu, B.P. Zhang, Z.H. Ge, P.P. Shang, Y.X. Chen, Mater. Chem. Phys. 131 (2011) 216.

[33] C.R. Nony, M.C. Bowman, T. CairnsJ. Anal. Toxicol. 4 (1980) 132, 140.

[34] D. M. Johnson, D. R. Hokanson, Q. Zhang, K. D. Czupinski, and J. Tang, J. Environ. Manag, 4 (2008) 416, 88.

[35] X. Li, J. Zhu, H. Li, Appl. Catal. B Environ. 123 (2012) 174.

[36] J.S. Park, W. Choi, Langmuir. 20 (2004) 11523.

[37] Y. Mi, H. Li, Y. Zhang, R. Zhang, W. Hou, Appl. Surf. Sci. 423 (2017) 1062.

[38] J. Cao, B. Xu, H. Lin, B. Luo, S. Chen, Catal. Commun. 26 (2012) 204.

[39] A. Thiam, E. Brillas, J.A. Garrido, R.M. Rodríguez, I. Sirés, Appl. Catal. B Environ. 180 (2016) 227.

[40] U.I. Gaya, A.H. Abdullah, J. Photochem. Photobiol. C Photochem. Rev. 9 (2008) 1.

[41] Y. Huang, W. Fan, B. Long, H. Li, F. Zhao, Z. Liu, Y. Tong, H. Ji, Appl. Catal. B Environ. 185 (2016) 68.

[42] N. Liang, J. Zai, M. Xu, Q. Zhu, X. Wei, X. Qian, J. Mater. Chem. A. 2 (2014) 4208

[43] R. Albuquerque, M.C. Neves, M.H. Mendonça, T. Trindade, O.C. Monteiro, Colloids Surfaces A Physicochem. Eng. Asp. 328 (2008) 107.

[44] Y.N. Tan, C.L. Wong, A.R. Mohamed, ISRN Mater. Sci. 2011 (2011) 1.

[45] M. Zhao, G. Li, L. Li, L. Yang, J. Zheng, Cryst. Growth Des. 12 (2012) 3983.

[46] L. Song, C. Chen, S. Zhang, Powder Technol. 207 (2011) 170.

[47] W.P.C. Lee, L.L. Tan, S. Sumathi, S.P. Chai, Int. J. Hydrogen Energy. 43 (2018) 748.

CHAPTER 3

3.0 EXPERIMENTAL PROCEDURE

3.1 Preparation of the dithiocarbamate ligands and complexes

The dithiocarbamate ligands and complexes were prepared using some reported literature methods with slight modifications [1,2].

3.1.1 Synthesis of sodium 4-methyl-phenyldithiocarbamate [NaL^1]

4-methylaniline (2.14 g, 0.02 mol) was dissolved in 4 mL of distilled water and 25 mL of tetrahydrofuran (THF) and stirred. This was followed by the addition of a solution of NaOH (0.80 g, 0.02 mol), in distilled water, to the stirring mixture under an atmosphere of nitrogen. After stirring for 1 h, carbon disulphide (1.2 mL, 0.02 mol) was added dropwise via a syringe into the solution. Thereafter, the solution was stirred steadily for about 6-7 h at room temperature and filtered via suction. The precipitate obtained was then rinsed with ice-cold ethanol and kept in the refrigerator.

[NaL^1]: Yield 2.035 g, 69.2%; M.pt 226-228°C; Selected FTIR, υ (cm^{-1}): 1469 (C=N), 1243 (C_2-N), 975 (C=S), 2949 (-CH), 3053 (=CH), 3398 (-NH), 1506 δ(NH)

3.1.2 Synthesis of sodium N-phenyldithiocarbamate [NaL^2]

A solution of NaOH (0.8 g, 0.02 mol) in 10 mL of distilled water was prepared in a round bottomed flask. To this solution, aniline (1.86 g, 0.02 mol) was added and the mixture was stirred at a low temperature range of 2 to 4 °C. After about 5 min, carbon disulphide (1.21 mL, 0.02 mol) was added slowly to the mixture. The faint yellowish-white solid product which separated out was then filtered, washed with small portions of ether, and recrystallized in acetone.

[NaL^2]: Yield-1.56 g, 84.78%; M.pt 134 – 135°C; Selected FTIR, υ (cm^{-1}): 1442 (C=N), 1281 (C_2-N), 986 (C=S), 3009 (-CH), 3198 (=CH), 3400 (-NH), 1526 δ (NH)

3.1.3 Synthesis of sodium *N*-benzyldithiocarbamate [NaL^3]

A solution of NaOH (0.8 g, 0.02 mol) in 10 mL of distilled water was prepared in a round bottomed flask charged with a thermometer. To this solution, benzylamine (2.23 mL, 0.02 mol) was added, and the mixture was stirred at low temperature range of 2-4°C. After about 5 min, carbon disulphide (1.21 mL, 0.02 mol) was added slowly to the mixture. The yellowish-white solid product which separated out was filtered, washed with small portions of ether, and recrystallized in acetone.

[NaL^3]: Yield-1.34 g, 60.63%; M.pt. 178-180°C; Selected FTIR, υ (cm^{-1}): 1479 (C=N), 1219 (C_2-N), 963 (C=S), 2942 (-CH), 3284 (=CH), 3336 (-NH), 1552 δ(NH)

3.2. Synthesis of the bismuth dithiocarbamate complexes

The bismuth complexes were prepared by reacting an aqueous solution of the respective dithiocarbamate ligand with aqueous solution of $BiCl_3 \cdot 2H_2O$ in 3:1 mole ratio (ligand to metal salt). Then, the precipitate formed was filtered, washed using a mixture of ethanol (50 mL) and water (150 mL). The pure complex was obtained from the chloroform solution of the crude product by dissolving in chloroform, filtering to remove the by product and evaporating off the solvent.

Bi(III) tris (4-methyl-phenyldithiocarbamate)

[$Bi(L^1)_3$]: Yield- 1.38 g, 87.8%; M.pt: 195 – 196°C; Selected FTIR, υ (cm^{-1}): 1476 (C=N), 1241 (C_2-N), 1021 (C=S), 2835 (-CH), 3138 (=CH), 3300 (NH), 1546 δ(-NH); ^{1}H NMR ($CDCl_3$) δ (ppm) = 7.78 (s, 3H, H<u>N</u>-C_6H_4), 7.24 – 7.17 (m, 12H, HN-C_6<u>H</u>$_4$), 2.33 (s, 9H, Ar-CH_3); ^{13}C NMR ($CDCl_3$) δ (ppm) = 180.37 (-N<u>C</u>S_2), 137.09, 134.56, 130.11, 125.42 (HN-<u>C</u>$_6H_4$), 20.99 (Ar-<u>C</u>H_3); Anal. calc. $C_{24}H_{24}N_3S_6Bi$ (755.84): C, 38.14; H, 3.20; N, 5.56; S, 25.45; Found: C, 38.34; H, 3.11; N, 5.16; S, 25.22

Bi(III) tris (*N*-phenyldithiocarbamate)

[Bi(L^2)$_3$]: Yield-1.39 g, 85.93%; M.pt: 153-154 °C; Selected FTIR, υ (cm^{-1}): 1485 (C=N), 1232 (C_2-N), 1012 (C=S), 2790 (-CH), 3197 (=CH), 3313 (NH), 1524 δ(-NH); ^{1}H NMR ($CDCl_3$) δ (ppm)= 7.91 (s, 3H, HN-C_6H_5), 7.35 – 7.18 (m, 15H, N-C_6H_5); ^{13}C NMR ($CDCl_3$) δ (ppm)= 179.97 (-NCS_2), 137.13, 127.04, 129.56, 125.22 (HN-C_6H_5); Anal. calc.$C_{21}H_{18}N_3S_6Bi$ (713.76): C, 35.34; H, 2.54; N, 5.89; S, 26.95; Found: C, 35.23; H, 2.14; N, 6.01; S, 26.34

Bi(III) tris (*N*-benzyldithiocarbamate)

[Bi(L^3)$_3$]: Yield- 1.54 g,86.52%; M.pt: 174-176 °C; Selected FTIR, υ (cm^{-1}): 1490 (C=N), 1207 (C_2-N), 1030 (C=S), 2919 (-CH), 3279 (=CH), 3279 (NH), 1547 δ(-NH); ^{1}H NMR ($CDCl_3$) δ (ppm)= 7.68 (s, 3H,C_6H_5-CH_2-NH), 7.52 – 7.19 (m, 15H,C_6H_5-CH_2-NH), 4.80-4.69 (t, 6H,C_6H_5-CH_2-NH); ^{13}C NMR ($CDCl_3$) δ (ppm)= 181.91 (-NCS_2), 48.55 (C_6H_5-CH_2-NH), 136.71, 135.46, 134.22, 129.52, 126.80 (C_6H_5-CH_2-CH_2NH); Anal. calc. $C_{24}H_{24}N_3S_6Bi$ (755.01): C, 38.14; H, 3.20; N, 5.56; S, 25.45; Found: C, 37.99; H, 3.01; N, 5.78; S, 25.05

3.3 Synthesis of bismuth sulphide nanomaterials

Among the various methods that have been reported for the synthesis of nanoparticles, the use of single source precursors has the advantage of avoiding the toxic cation precursors and eliminating the undesired effects of the anions of the metal salts during the synthesis. These precursors are typically non-pyrophoric, air stable compounds and have proven to be of great advantage in synthesizing good quality nanocrystals as they need to be heated to only moderately high temperatures. In the light of these advantages, the SSP method has been chosen for the synthesis of Bi_2S_3 reported in this project.

3.3.1 Synthesis of Bi_2S_3 nanorods by solvothermal method[3]

In a typical procedure, 0.25 g of the respective bismuth complex was dispersed in trioctylphosphine (TOP). This suspension was injected into a degassed 4 g of pre-heated hexadecylamine (HDA) in a 250 mL round bottomed three neck flask at 120 °C under nitrogen. The reaction temperature dropped by 15 °C and was heated gently to 120 °C and maintained for 1 h. Thereafter, the reaction was terminated and the temperature of the mixture was allowed to cool down to 65 °C. Excess methanol was then added in order to flocculate the HDA capped

bismuth sulphide nanoparticles. The nanoparticles were isolated by centrifuging, rinsed 3 times with methanol and allowed to dry. Three different bismuth sulphides nanorods were isolated from precursor complexes and represented as $Bi_2S_3(1)$, $Bi_2S_3(2)$ and $Bi_2S_3(3)$ to denote the nanorods obtained from precursor compounds [**Bi(L^1)$_3$**], [**Bi(L^2)$_3$**], and [**Bi(L^3)$_3$**] respectively.

3.3.2 Synthesis of Bi_2S_3 nanoparticles by microwave method[4]

About 0.25 g of the respective bismuth dithiocarbamate complex was dispersed in ethylene glycol. The solution was transferred into a 25 mL Teflon lined microwave reactor vessel, bubbled with nitrogen, and then placed under microwave irradiation of 800 W with stirring. After about 1 hour, the resulting solution was cooled down to room temperature and ethanol was added to precipitate the product. The solution was centrifuged and the precipitate obtained was washed three times with ethanol and dried in air.

3.4 Synthesis of Mn(II) and Sn(IV) doped Bi_2S_3 nanomaterials by hydrothermal method[5]

Mn(II) and Sn(IV) doped Bi_2S_3 nanomaterials were prepared by introducing Mn(II) acetate (0.034 g) or Sn(IV) chloride (0.037 g) into the beaker containing the respective bismuth dithiocarbamate complex (0.25 g) and oleyamine (7.5 mL). The obtained solution was transferred into a 100 mL capacity Teflon-lined autoclave sample reactor vessel, and heated up to 180 °C. The reaction was maintained for 8 h. After the reaction, the solution was allowed to cool to room temperature, then ethanol was added and the precipitate obtained was centrifuged and washed with ethanol. The process of precipitation with ethanol and centrifuging was carried out three times and the samples were dried in air.

3.5 Characterization of metal complexes

The infrared spectral studies of the complexes were done using Fourier-transform infrared (FTIR) spectrometer (Nicolet 560), in the wavenumber range of 4000-500 cm^{-1} at room temperature. The Nuclear Magnetic Resonance (NMR) spectra were recorded using a 600 MHz BrukerAvance III NMR spectrometer for ^1H and ^{13}C NMR analysis. The melting point measurement was done using a Gallenkamp melting point instrument.

3.6 Characterization of the Bi_2S_3 nanoparticles

The absorption spectra of the bismuth sulphide nanoparticles were obtained using a varian UV–vis spectrophotometer. The photoluminescence (PL) spectra were measured using Perkin Elmer LS 45 Fluorimeter. Powder X–ray diffractogram (XRD) of the nanoparticles were recorded on a Bruker D8 Advanced XRD machine, equipped with a proportional counter using Cu Kαradiation (λ=1.5405 A, nickel filter). Samples were added on a flat steel sample holder and scanned from 10 to 80 °C. The diffraction peaks at several values were matched with other recorded standards in JCPDS. The internal morphology of the nanoparticles were studied using transmission electron microscopy-TEM (Hitachi HF–2000 TEM at 200 kV and FEI Tecnai G^2 Twin at 20 kV).The thermal behaviour of the adducts was studied using the simultaneous thermal analysis (STA) technique for parallel recording of TG (thermogravimetry) and DSC (differential scanning calorimetry) curves. The study was performed on an SDTQ 600 Thermal instrument. Samples were contained within alumina crucibles and heated at a rate of 10 °C min^{-1} from room temperature to 800 °C under flowing nitrogen.

3.7 Photocatalytic evaluation of the Bi_2S_3 and metal doped Bi_2S_3 nanomaterials [6]

The photocatalytic activities of the Bi_2S_3 and metal doped Bi_2S_3 nanoparticles were studied by measuring the degradation of methylene blue (30 mL, 10 mg/L) under visible light irradiation. For each measurement, 50 mg of the catalyst and dye solution were mixed in a Pyrex glass vessel. Then, the suspensions were magnetically stirred in the dark cupboard for about 1 h to ensure an adsorption-desorption equilibrium between the dye and the catalyst. After 30 min, the solutions were exposed to the halogen lamp for 6 h with constant stirring in the photocatalytic reaction compartment. The degradation efficiency of the dye was analysed using UV-vis spectrometer at specific intervals.

3.8 Results and Discussion

3.8.1 Synthesis of the dithiocarbamate ligands and complexes

Dithiocarbamate derivatives are prepared by the nucleophilic reaction between primary or secondary amines with carbon disulphide, in the presence of a strong base e.g, sodium hydroxide, potassium or ammonium hydroxide. The reaction is carried out at a very low

temperature in ice (0 - 4°C), and it usually gives high yield. When dithiocarbamates are prepared from primary amines, the products obtained are usually less stable than dithiocarbamate obtained from secondary amines. The poor stability of the dithiocarbamate obtained from primary ammines has been ascribed to the presence of acidic hydrogen on the nitrogen [7]. Because of the poor stability of the ligands, the complex formation was initiated *in-situ* using stoichiometric ratios of ligand to metal salt (3:1). The obtained complexes were stored under reduced temperature. Figure 3.1 presents the structures of the complexes synthesized.

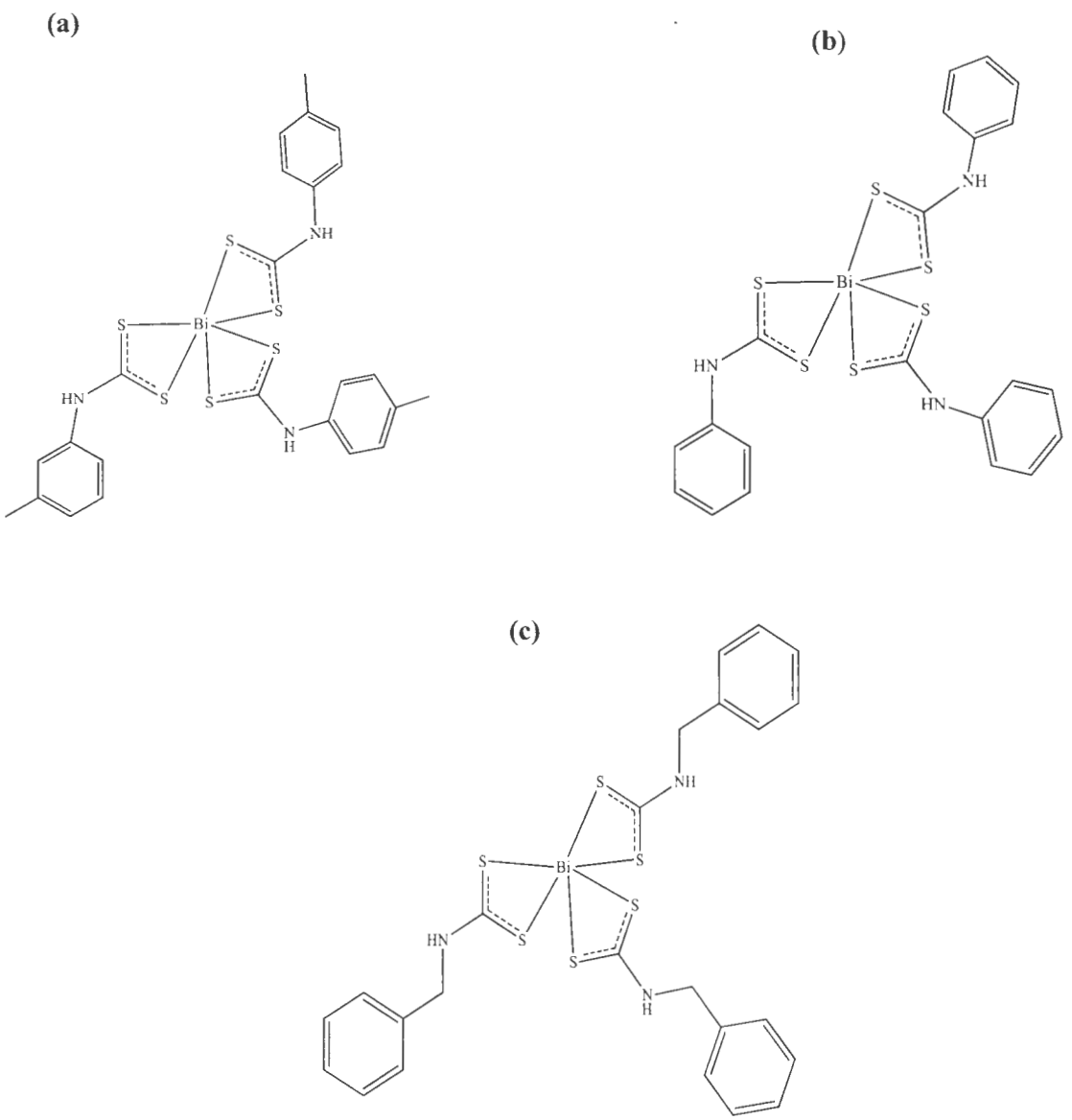

Scheme 3.1: Structures of the synthesized (a) Bi(III) tris (4-methyl-phenyldithiocarbamate), (b) Bi(III) tris (N-phenyldithiocarbamate), and (c) Bi(III) tris (N-benzyldithiocarbamate) complexes.

3.8.2 FTIR spectroscopic studies

The FTIR spectra of the ligands and the complexes were compared in order to ascertain the possible coordination sites involved in the complexation of the ligands with the metal ion. Vibration frequencies in the range 1479 – 1442 and 1281 – 1219 cm^{-1} were observed in the ligands, and these were attributed to the stretching vibrations of C-N bands found dithiocarbamate compounds. In the spectra of the complexes, a shift in the position of these bands was observed in the range of 1490 – 1476 cm^{-1} for ν(C=N) and 1241 – 1207 cm^{-1} for ν(C-N) [8]. The former is indicative of a partial double bond character of the C-N stretching vibrational band [9]. The appearance of a single symmetric peak for the stretching vibration (C-S) around the region 1000 ±70 cm^{-1} is indicative of a bidentate mode of coordination, while a splitted peak around this same region shows an anisobidentate or a monodentate coordination mode between the metal and the dithiocarbamate moiety [9-11]. In this study, these CS peaks were observed as a single peak in the range of 1021 – 968 cm^{-1} similar to what has been reported in literature, suggesting the existence of a bidentate mode of coordination in each of the complexes [12]. The stretching vibrations found around 3284 – 3053 cm^{-1} in the ligands were attributed to the (=C-H) of the aromatic ring and these bands shifted upon complexation to a lower frequency range in the complexes at about 3138 – 3007 cm^{-1}. Furthermore, the stretching vibration attributed to the para-substituted methyl group in $\mathbf{L^2}$ were observed in the spectrum complex $[\mathbf{Bi(L^2)_3}]$ as two peaks around 812 cm^{-1} and two low intensity peaks around 1894 and 1902 cm^{-1} similar to what has been reported in literature [1]. The stretching vibrational band of N-H bond for the ligands observed in the frequency range of 3400 – 3336 cm^{-1} shifted to a lower frequency range of 3279 – 3197 cm^{-1} in the complexes. The M-S band are often observed in the far infrared region in the frequency range of 300–450 cm^{-1} [13]. This band was observed in all the complexes between 350 and 450 cm^{-1}.

3.8.3 NMR spectroscopic studies of the complexes

The NMR spectral data of the complexes are shown in Figures 3.2 – 3.4. The spectral data of the complexes showed similar values although there are minor differences in the dithiocarbamate moiety of **[Bi(L^1)$_3$]** complex due to the para-substituted methyl group on the aromatic ring [7]. The protons of the aromatic rings in each of the complexes resonated in the low field region as a complex multiplets in the range 7.51 – 7.18 ppm [12]. From the observed frequencies of the aromatic protons, the peaks having the higher values are assigned to the protons ortho- to the carbon of the thioureide group; the high resonant frequency value is ascribed to the deshielding effect as a result of the electronegative N-atom and their proximity to the CS_2 group [12]. The signals of the protons ($-CH_3$) from the methyl group of **[Bi(L^1)$_3$]** complex resonated as singlet around 2.33 ppm. Furthermore, the signals due to the methylene protons ($-CH_2$) appeared in the range of 4.80– 4.69 ppm assinglet in the benzyl complex **[Bi(L^3)$_3$].** The proximity of the methylene group to the electronegative nitrogen is responsible for the appearance of the signal in this environment [14]. The proton of the -NH group was found somewhat down-field at about 7.91 - 7.68 ppm due to its attachment to nitrogen atom similar to what has been reported [14].In the ^{13}C NMR spectra, the complexes showed carbon signals in the range of 181-179 ppm, ascribed to the carbon of the thiouireide bond [15]. The appearance and position of this peak shows the contribution of the double bond character in the complexes to a formally single N-C bond in the dithiocarbamate moiety [16]. The phenyl carbons from the dithiocarbamate moiety are affected by the coordination of the bismuth metal. Coordination of the bismuth atom to the respective ligands caused a decrease in the partial double bond character of the nitrogen–carbon bond as well as the movement of electron density towards the nitrogen from the carbon atom of the dithiocarbamate group. This, explains the additional deshielding of carbon sites upon complexation[12]. The carbon signal of the methyl group in the para- position of complex **[Bi(L^1)$_3$]** was observed at 20.99 ppm [1], while the carbon signal of the methylene group of complex **[Bi(L^3)$_3$]** was observed for the benzyl derivative at 48.55 ppm [14].

(a)

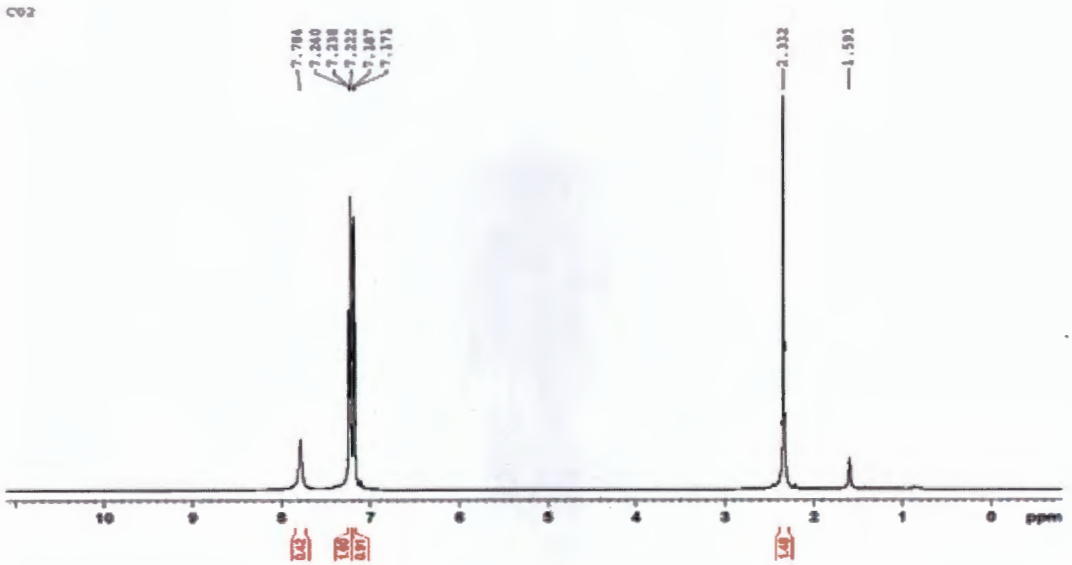

(b)

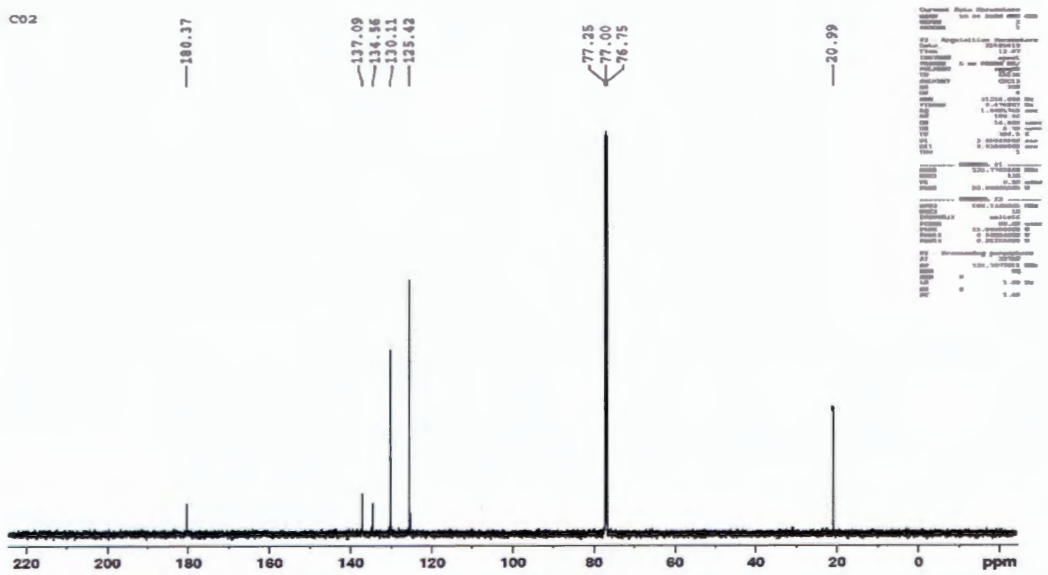

Figure 3.2: **(a)** ^{1}H and **(b)** ^{13}C NMR spectra of Bi(III) tris(4-methyl-phenyldithiocarbamate) complex, **[Bi(L^1)$_3$]**.

(a)

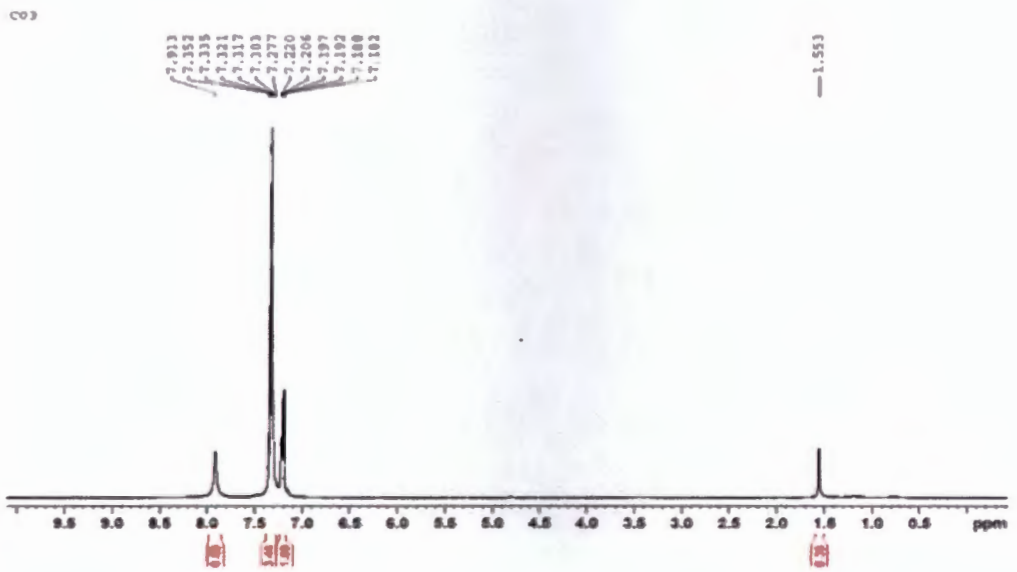

(b)

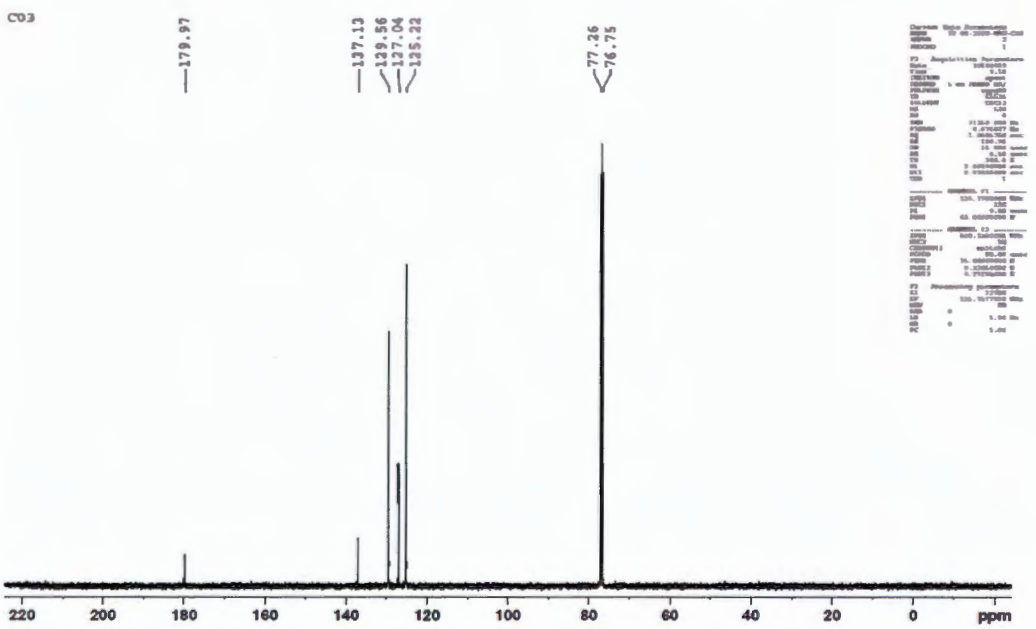

Figure 3.3: **(a)** ^{1}H and **(b)** ^{13}C NMR spectra of Bi(III) tris (*N*-phenyldithiocarbamate) complex, **[Bi(L^2)$_3$]**.

(a)

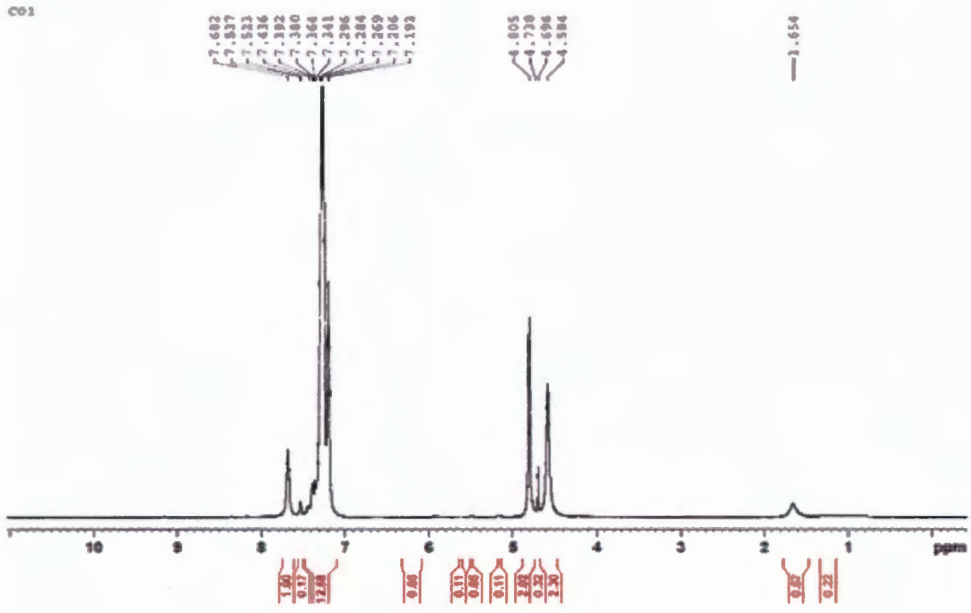

(b)

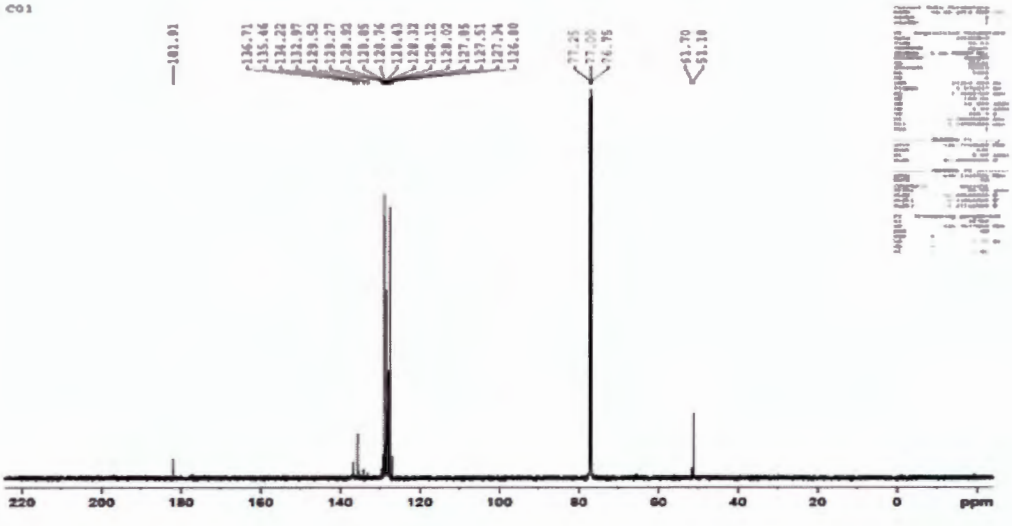

Figure 3.4: **(a)** ^{1}H and **(b)** ^{13}C NMR spectra of Bi(III) tris (*N*-benzyldithiocarbamate) complex, **[Bi(L^3)$_3$]**.

3.8.4 Thermal studies

Figure 3.5 presents the TG/DTG curves of **[Bi(L^1)$_3$]**, **[Bi(L^2)$_3$]**, and**[Bi(L^3)$_3$]**, obtained under nitrogen atmosphere.The thermogravimetric curves of the complexes showed a single decomposition step (Fig. 3.5a to c) in the range 275 – 375, 275 – 369, and 216 – 340 °C, for complexes **[Bi(L^1)$_3$]**, **[Bi(L^2)$_3$]**, and**[Bi(L^3)$_3$]**, respectively. Prior to the decomposition, the compounds underwent sharp melting at 195, 154 and 176 C respectively. In the TGA curve, the presence of a plateau before 200 °C with no apparent weight loss is indicative of the absence of any entrapped water molecules or solvent within the compounds. After melting, the complexes maintained their stability for additional temperature of about 80 – 100 °C, before decomposition. The absence of any observable change in the DTG curve between the melting and decomposition temperature indicated that the compounds did not undergoe a crystalline change before decomposition set in [17]. The decomposition of the compounds involved a sharp mass loss involving most of the organic ligand, and the maximum rate of decomposition, deduced from the DTG curve, occurred around 344, 350 and 301 °C for **[Bi(L^1)$_3$]**, **[Bi(L^2)$_3$]**, and**[Bi(L^3)$_3$]**, respectively. Based on the temperature of maximum rate of decomposition, the stability of the three compounds could be said to follow the trend **[Bi(L^2)$_3$]>[Bi(L^1)$_3$]>[Bi(L^3)$_3$].**In general, during thermal decomposition, dithiocarbamate complexes could form the respective metal sulphides by undergoing a single decomposition or via the isothiocyanate intermediate. The complexes could also volatilize leaving behind negligible amounts of residue, hence volatile and no-volaitile dithiocarbamates complexes are known [18,19]. In the present study, the stoichiometric calculation of the amount of residue obtained at the end of the TGA analysis (800 °C) confirmed Bi_2S_3 as the component of the final residue from each decomposition profile. In related study, thermal decomposition of Bismuth *N*-ethyl cyclohexyl dithiocarbamate under nitrogen atmosphere gave pure phase orthorhombic Bi_2S_3 [20]; while the final residue obtained from tris(*N*-furfuryl-*N*-benzyldithiocarbamato-S,S')bismuth(III) decomposed in air atmosphere was analyzed to be α-Bi_2O_3 [21].

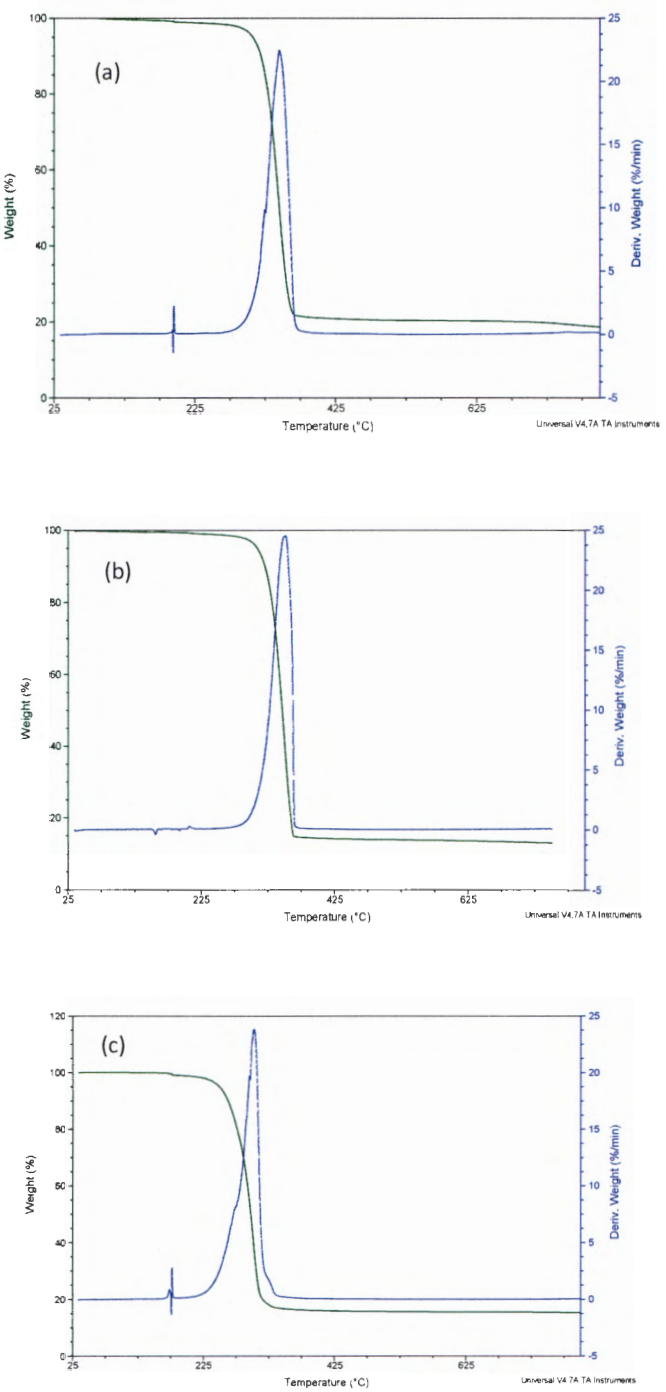

Figure 3.5: TG/DTG curves of **[Bi(L^1)$_3$]**, **[Bi(L^2)$_3$]**, and **[Bi(L^3)$_3$]**,obtained under nitrogen atmosphere.

REFERENCES

[1] D.C. Onwudiwe, T. Arfin, C.A. Strydom, R.J. Kriek, Electrochim. Acta. 104 (2013) 19.

[2] D.C. Onwudiwe, Y.B. Nthwane, A.C. Ekennia, E. Hosten, Inorgan. Chim. Acta. 447 (2016) 134.

[3] G. Zhu, P. Liu, J. Zhou, X. Bian, X. Wang, J. Li, B. Chen, Mater. Lett. 62 (2008) 2335.

[4] J. Wu, F. Qin, G. Cheng, H. Li, J. Zhang, Y. Xie, H.J. Yang, Z. Lu, X. Yu, R. Chen, J. Alloys Compd. 509 (2011) 2116.

[5] S. Kaowphong, P. Dumrongrojthanath, S. Kittiwachana, S. Thongtem, T. Thongtem, Mater. Lett. 107 (2013) 295.

[6] N. Riaz, F.K. Chong, B.K. Dutta, Z.B. Man, M.S. Khan, E. Nurlaela, Chem. Eng. J. 185 (2012) 108.

[7] D.C. Onwudiwe, T. Arfin, C.A. Strydom, R.J. Kriek, Electrochim. Acta. 109 (2013) 809.

[8] N.H. Abdullah, Z. Zainal, S. Silong, M.I.M. Tahir, K.B. Tan, S.K. Chang, Mater. Chem. Phys. (2016).

[9] A.M. Paca, P.A. Ajibade, Mater. Chem. Phys. 202 (2017) 143.

[10] P.A. Ajibade, D.C. Onwudiwe, M.J. Moloto, Polyhedron 30 (2011) 246.

[11] J.Z. Mbese, P.A. Ajibade, J. Sulfur Chem. 35 (2014) 438.

[12] D.C. Onwudiwe, P.A. Ajibade, Polyhedron. 29 (2010) 1431.

[13] F. Bensebaa, Y. Zhou, A.G. Brolo, D.E. Irish, Y. Deslandes, E. Kruus, T.H. Ellis, Spectrochim. Acta 55A (1999) 1229.

[14] F.F. Bobinihi, J. Osuntokun, D.C. Onwudiwe, J. Saudi Chem. Soc. 22 (2018) 381.

[15] D.C. Onwudiwe, P.A. Ajibade, Synth. React. Inorg. Met. Nano-Metal Chem. 40 (2010) 279.

[16] N. Srinivasan, S. Thirumaran, S. Ciattini, J. Mol. Struct. 936 (2009) 234.

[17] E.T.G. Cavalheiro, M. Ionashiro, G. Marino, S.T. Breviglieri, G.O. Chierice, Trans. Met. Chem. 25 (2000) 69.

[18] A. Bajpai, S. Tiwari, Thermochim. Acta. 411 (2004) 139.

[19] R.B. Lanjewar, A.N. Garg, Ind. J. Chem. 31A (1992) 849.

[20] N.H. Abdullah, Z. Zainala, S. Silong, M. I. M. Tahir, K-B. Tan, S-K Chang, Thermochim. Acta 632 (2016) 37.

[21] S. Tamilvanan, G. Gurumoorthy, S. Thirumaran, S. Ciattin. Polyhedron 121 (2017) 70.

CHAPTER 4

4.1. DISCUSSION

This chapter presents the characterization of bismuth sulphide nanomaterials prepared by solvothermal and microwave methods; and the metal (Sn and Mn) doped bismuth sulphide obtained via the use of an autoclave. The compounds prepared in chapter three: **[Bi(L^1)$_3$]**, **[Bi(L^2)$_3$]**, and **[Bi(L^3)$_3$]**, were utilized as single source precursors. The results clearly showed the effect of the method of synthesis on the optical and structural properties of the obtained bismuth sulphide. Furthermore, the evaluation of the photocatalytic properties of the bismuth sulphides are presented and discussed.

4.1 XRD studies

XRD was employed to determine the crystalline phase of the undoped and the Mn/Sn doped as-prepared sample of Bi_2S_3 nanomaterials. Fig 4.1 to 4.6 show the overlapped diffractogram of undoped Bi_2S_3 and Mn/Sn doped Bi_2S_3 nanoparticles obtained from the XRD analysis and the patterns were identified as orthorhombic crystal structure of $Bi_2S_3$with a JCPD No. 17-0320 [12]. Notable peaks observed at 2θ values of 23.39°, 24.92°, 28.60° and 31.79° can be indexed to the reflection pattern of (220), (130), (211) and (221) respectively. It is worth noting that the intensity of the diffraction peak of Mn doped Bi_2S_3 is lower than that of the undoped Bi_2S_3. In all the Mn/Sn doped Bi_2S_3 in Figure 4.1 to 4.6, this trend seems to be the same. Apart from the decrease in intensity, it could also be observed that the diffraction peaks of some of the Mn and Sn doped Bi_2S_3 tend to be mildly displaced toward the zero mark of the 2θ value in degrees. This indicated that Mn/Sn have doped into the lattice of Bi_2S_3.

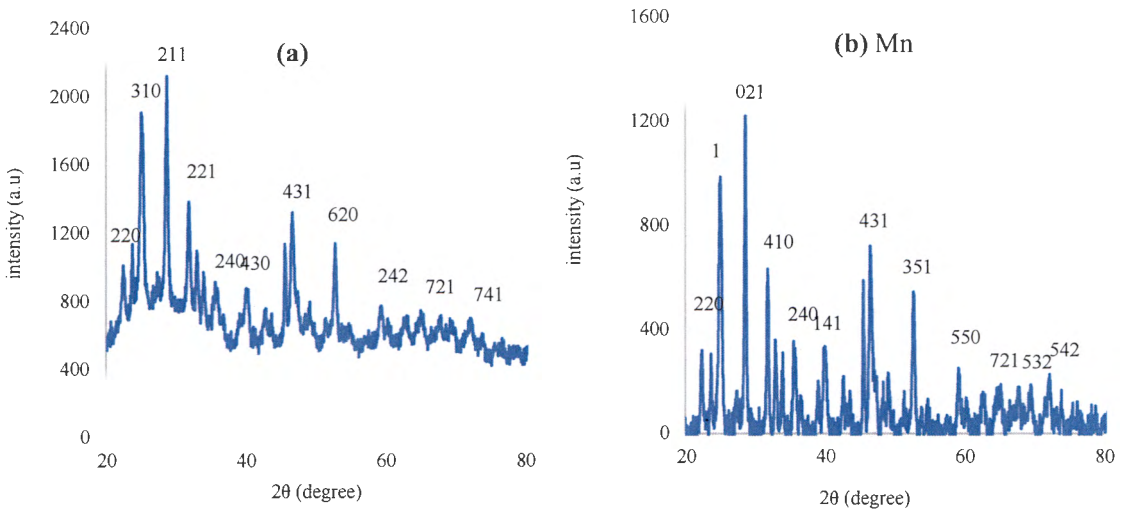

Figure 4.1: XRD of (a) undoped and (b) Mn doped Bi_2S_3 nanomaterials obtained from $[\mathbf{Bi(L^1)_3}]$.

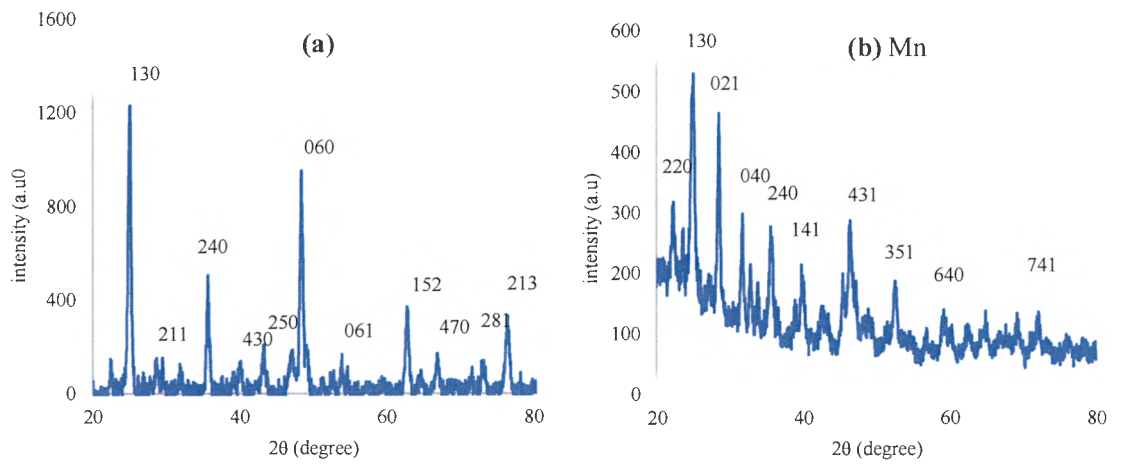

Figure 4.2: XRD of (a) undoped and (b) Mn doped Bi_2S_3 nanomaterials obtained from $[\mathbf{Bi(L^2)_3}]$.

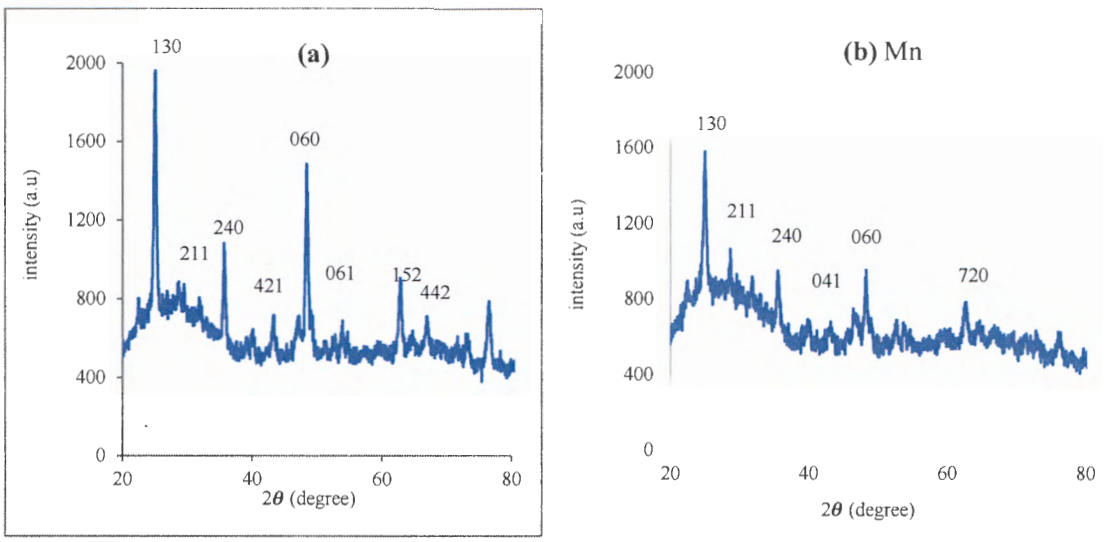

Figure 4.3: XRD of (a) undoped and (b) Mn doped Bi_2S_3 nanomaterials obtained from $[\mathbf{Bi(L^3)_3}]$.

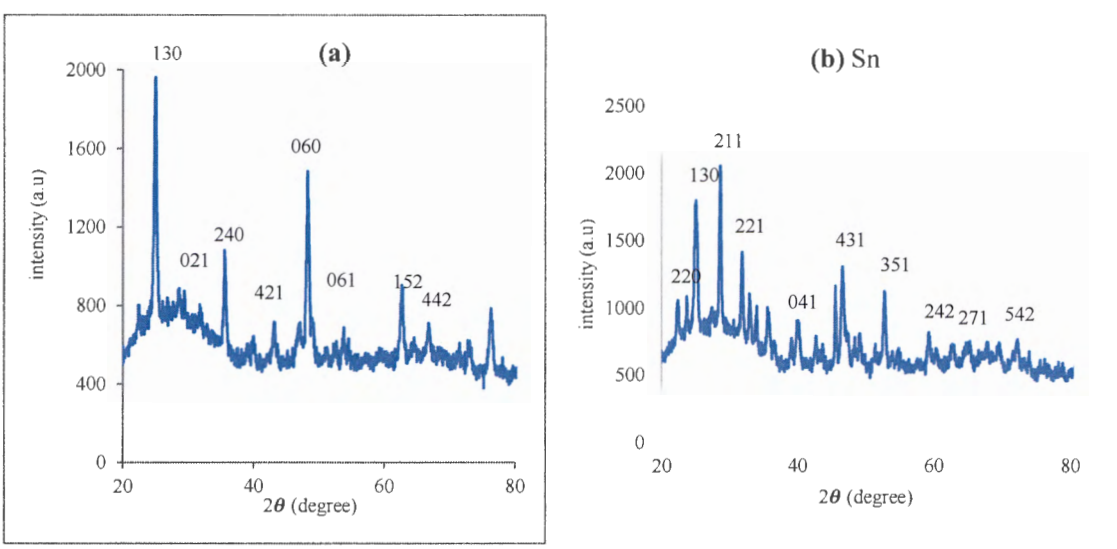

Figure 4.4: XRD of (a) undoped and (b) Sn doped Bi_2S_3 nanomaterials obtained from $[\mathbf{Bi(L^1)_3}]$.

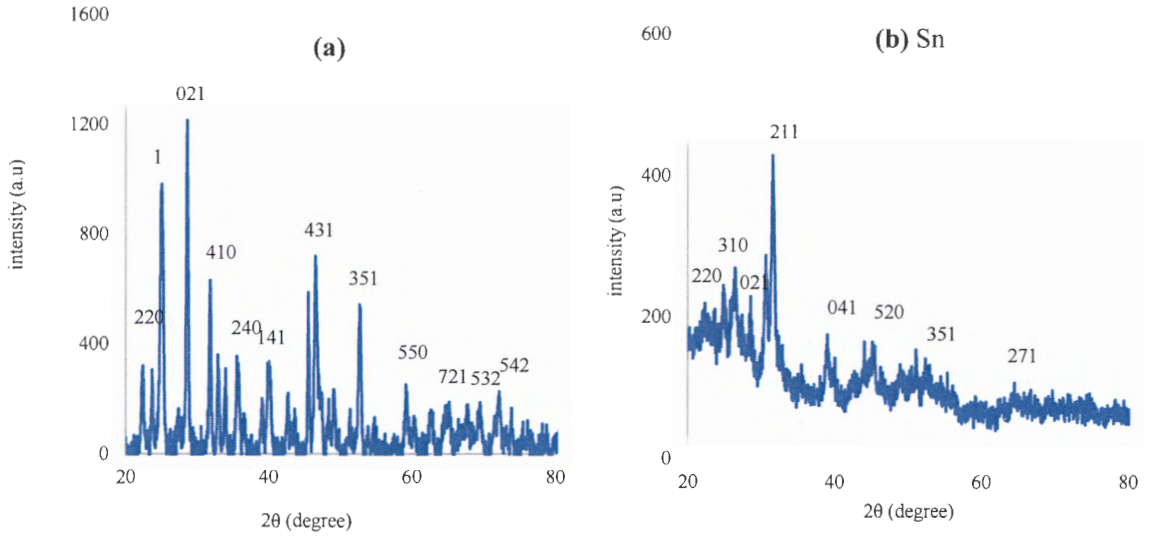

Figure 4.5: XRD of (a) undoped and (b) Sn doped Bi_2S_3nanomaterials obtained from $[\mathbf{Bi(L^2)_3}]$.

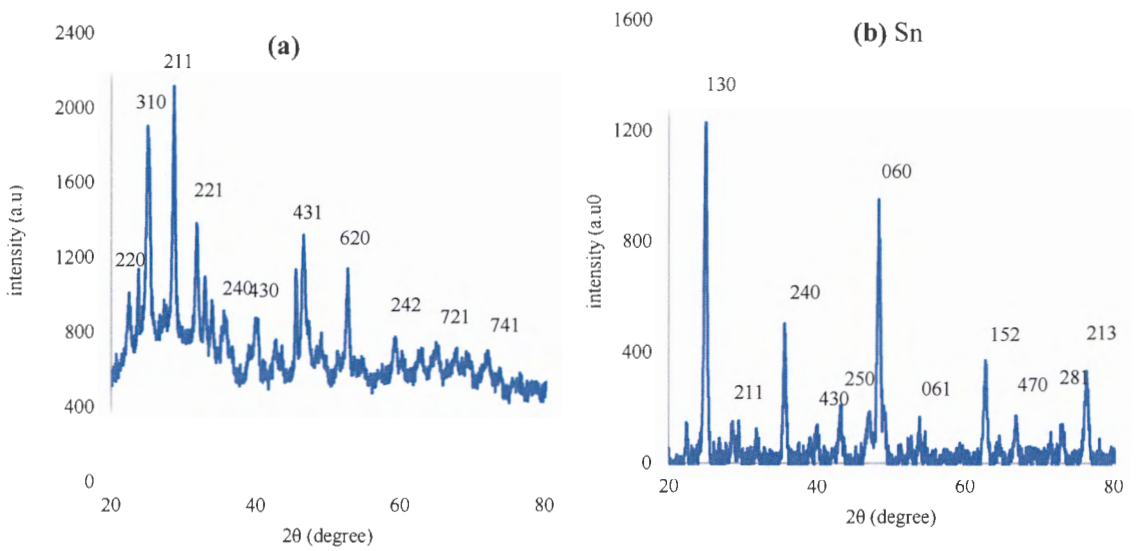

Figure 4.6: XRD of (a) undoped and (b) Sn doped Bi_2S_3 nanomaterials obtained from $[\mathbf{Bi(L^3)_3}]$.

4.2 TEM studies

4.2.1 Microwave irradiation method

Figures 4.7-4.9 show the TEM images of the Bi_2S_3 nanomaterials obtained using complexes **[Bi(L^1)$_3$]**, **[Bi(L^2)$_3$]**, and **[Bi(L^3)$_3$]** respectively, under microwave irradiation. All the nanoparticles appeared agglomerated, and the effect of using different types of complexes (under same synthesis conditions) did not seem to influence the morphology of the nanoparticles. Contrary to the nanorods obtained when hot injection method was used, the TEM images of all the nanoparticles obtained by microwave methods depicted spherical morphology. It was difficult to estimate the sizes of the nanoparticles from the TEM images without compromising on the number of images required to make a reasonable average size determination. However, the size of the nanoparticles was less than 100 nm. The shape of nanoparticles is dependent on nucleation and growth process. In microwave synthesis, solvents play a critical role in the process of products formation. Properties such as the rate of collision between the reactants molecules, the rate of heating of the reaction, and the reaction temperature vary in different solvents [13]. Therefore, different nanostructures would result from different solvents. However, in the synthesis of nanoparticles using precursor compounds, the properties of the compounds have significant influence on their morphology and size. More specifically, in dithiocarbamates slight variations in the functional groups on the dithiocarbamato ligand have pronounced influence on the properties of the resulting nanoparticles even at uniform synthesis conditions such as temperature and solvent [14]. The observation of similar morphology and size in all the nanoparticles obtained irrespective of using three different complexes might be related to the similarity in their structure and decomposition profile. The undoped Bi_2S_3 and metal doped Bi_2S_3 nanomaterial showed different shape of nanorods using microwave, solvothermal and hydrothermal methods.

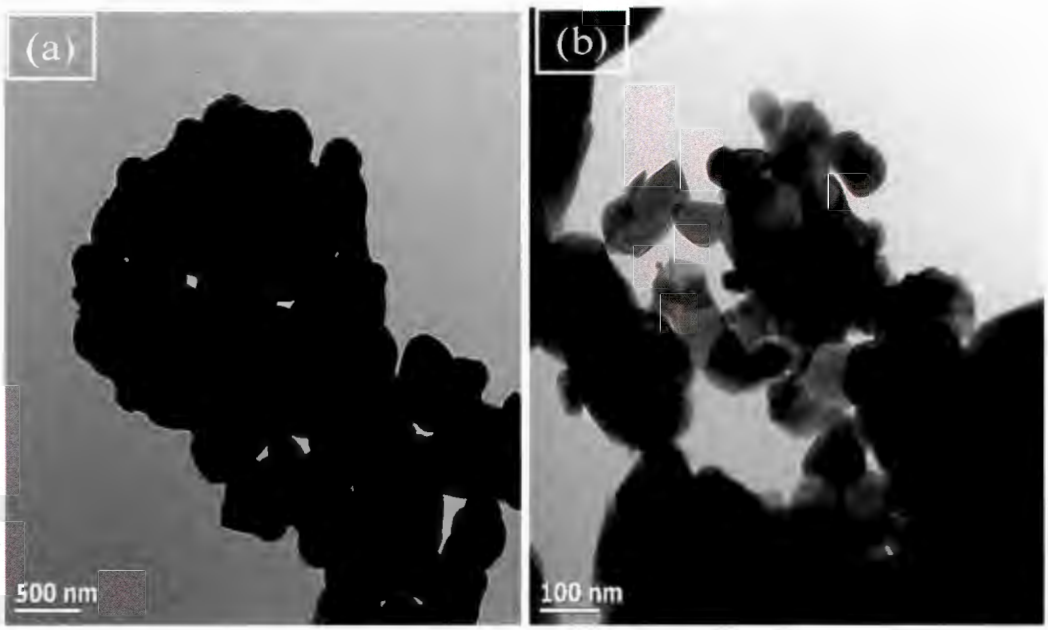

Figure 4.7: TEM images of Bi_2S_3 synthesized from complex **[Bi(L^1)$_3$]**.

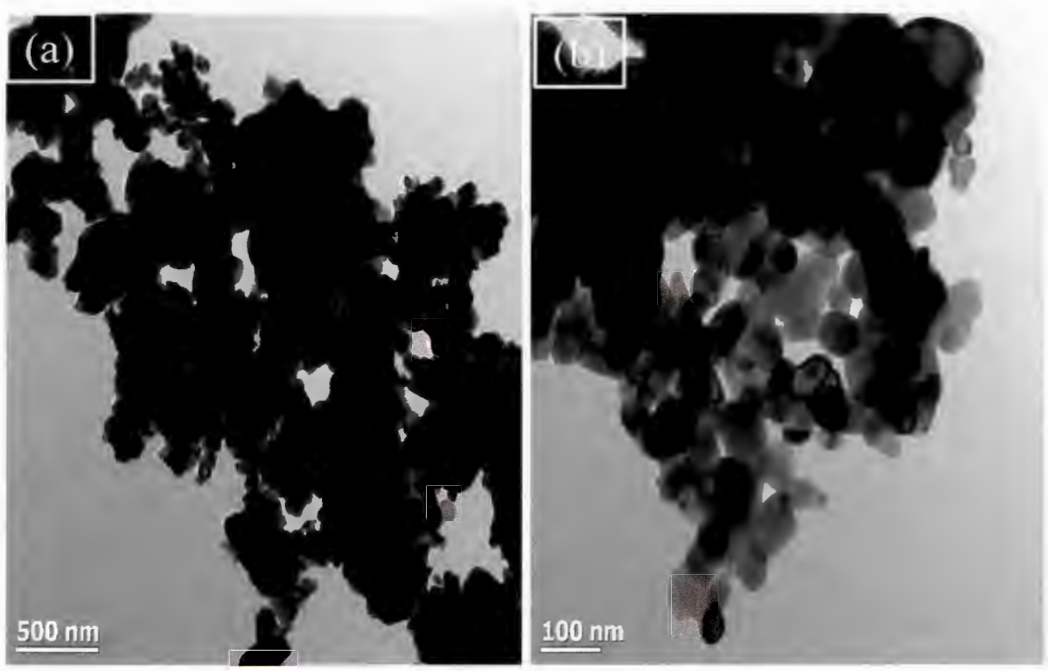

Figure 4.8: TEM images of Bi_2S_3 synthesized from complex **[Bi(L^2)$_3$]**.

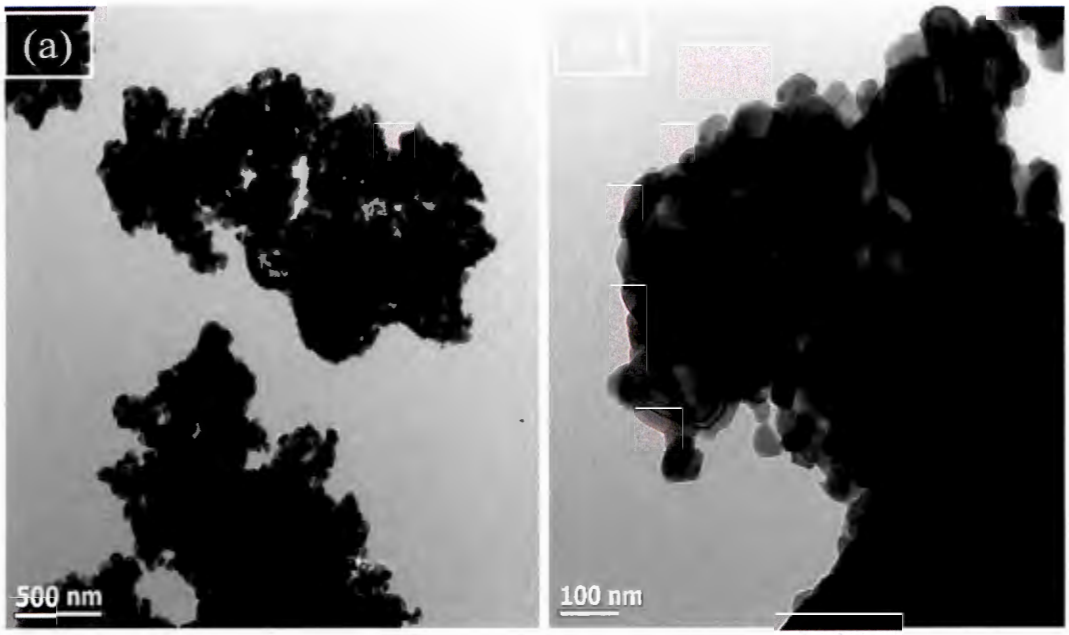

Figure 4.9: TEM images of Bi_2S_3 synthesized from complex **[Bi(L^3)$_3$]**.

4.2.2 Solvothermal method

The method of synthesis of nanomaterials influences the morphology and size of the as synthesized nanomaterials. Different morphologies and sizes of Bi_2S_3were prepared using a solvothermal method, and the TEM resultsshowed nanorods with length of 100 nm and diameter of 20 nm as shown in Fig 4.10. The Figures 4.10a and 4.10b showed low and high magnification of the TEM micrograph of Bi_2S_3 which exhibits nanorod morphology with average length and width size of 85.39 and 13.4 nm respectively. The nanorods were slightly monodispersed with less than 40 percent of the nanorod superimposed on one another. The inset in Figure 4.10 shows clearly the lattice fringes of Bi_2S_3 which confirmed the crystalline nature of the nanoparticles.

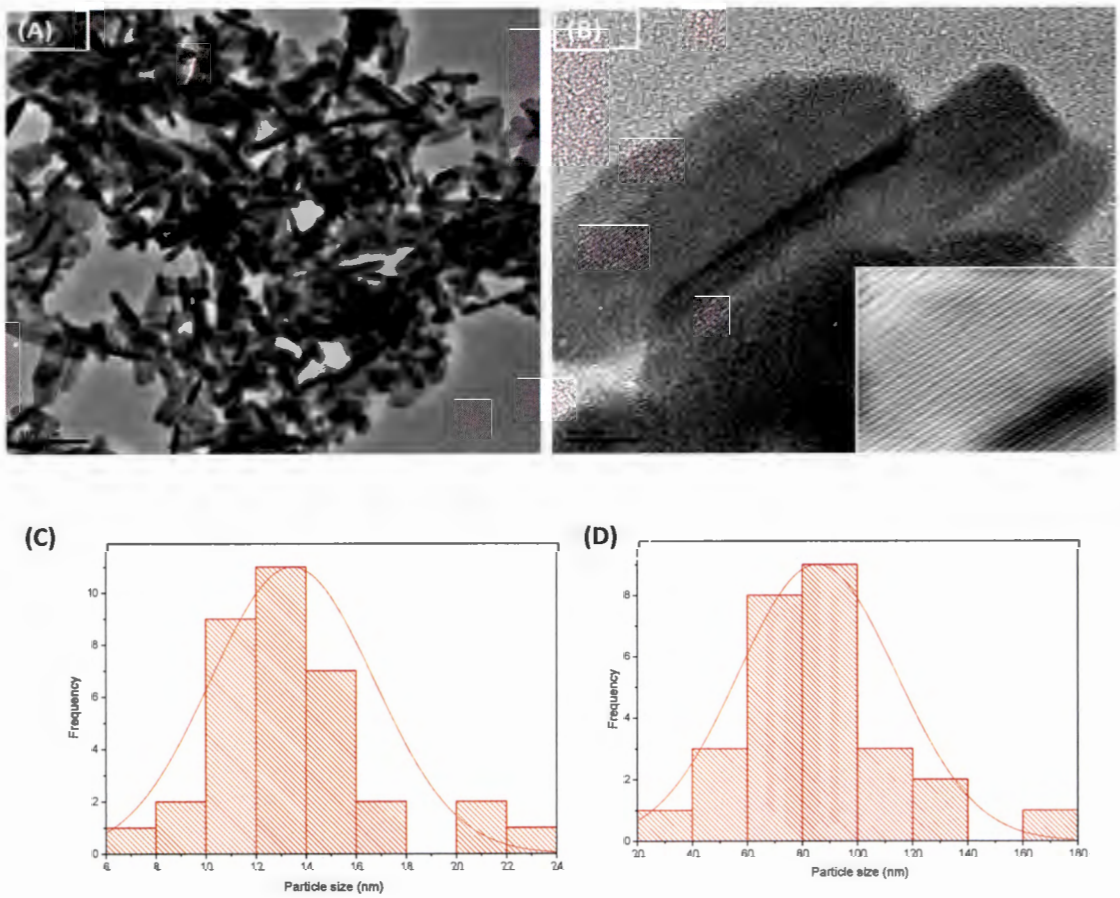

Figure 4.10: TEM micrograph ofBi_2S_3(1) nanorods prepared from [$\mathbf{BiL^1_3}$] at **(a)** low magnification, **(b)** high magnification, inset-HRTEM showing lattice fringes; with corresponding particle size histogram showing **(c)** width and **(d)** length of the nanorods.

The particles size distribution histogram in Figure 4.10 c and 4.10d reveal wide length and width of the nanorod. The calculated average aspect ratio for the nanorod is 6.3 nm. The nanorod type of morphology exhibited by the Bi_2S_3 is slightly due to the chain type structure of Bi_2S_3 nanoparticles which is known to form band structures as Bi units interlinked with weaker van der waals forces [14]. Figure 4.11a and 4.11b depict the TEM micrograph of Bi_2S_3(2) at lower and higher magnification and obtained from **[$Bi(L^2)_3$]**. The morphology of the sample Bi_2S_3(2) is rod-like the previous sample Bi_2S_3(1). The average size of the rods in length and width are 79.0 and 13.76 nm. Calculated aspect ratio of the Bi_2S_3nanorods obtained from **[$Bi(L^2)_3$]** is 5.7 nm.

Lattice fringes are shown in Figure 4.11(c), as inset diagram, and it confirmed the crystallinity of the nanorods.

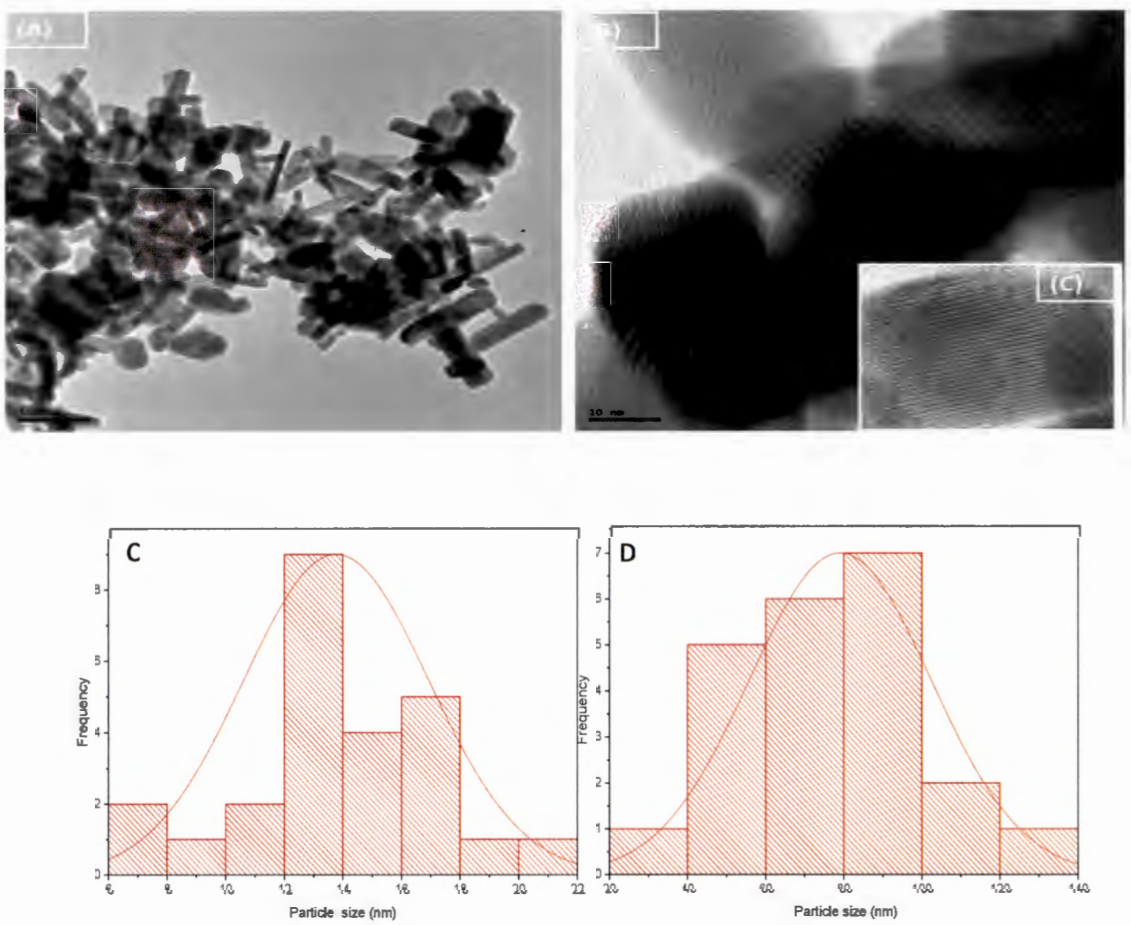

Figure 4.11: TEM micrograph of Bi_2S_3(2) nanorods prepared from **[BiL$^2_3$]** at **(a)** low magnification, **(b)** high magnification, inset-HRTEM showing lattice fringes; with corresponding particle size histogram showing **(c)** width and **(d)** length of the nanorods.

Figure 4.12 shows the TEM micrograph of Bi_2S_3(3) nanorods at low and high magnification. The TEM images reveal nanostructures that are made up of short and long nanorods with the length and width ranging from 15-55 nm and 40-140 nm respectively. The average size of length and

width are 74 and 36 nm. Like the previously discussed nanorods, the HRTEM shows lattice fringes which are synonymous to good crystallinity of the nanorods.

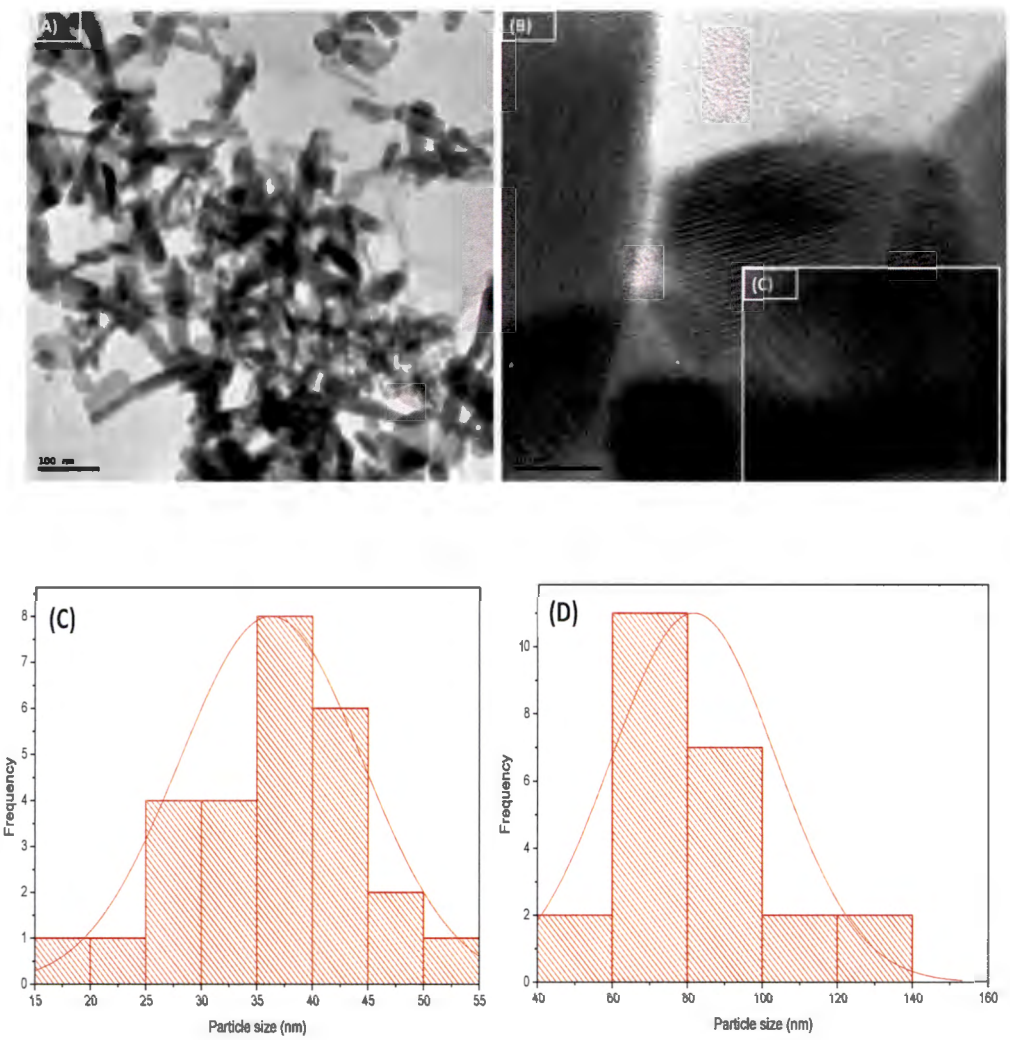

Figure 4.12: TEM micrograph of Bi_2S_3(3) nanorods prepared from [**BiL$^3_3$**] at **(a)** low magnification, **(b)** high magnification, inset-HRTEM showing lattice fringes; with corresponding particle size histogram showing **(c)** width and **(d)** length of the nanorods.

4.2.3 Hydrothermal method

The metal doped Bi_2S_3 nanorods were successfully prepared through hydrothermal method and assembled narrow length nanorods were obtained. TEM micrograph of Mn doped Bi_2S_3 in Figure 4.13a and b showed that the nanomaterials were made up of needle shaped nanorods with the width of the nanorods in the range of 3-10 nm and the length of the nanorods being between 20-80 nm. Particle size distribution histogram in Figure 4.13c and 4.13d revealed 70 and 8 nm as the length and width of the nanorods.

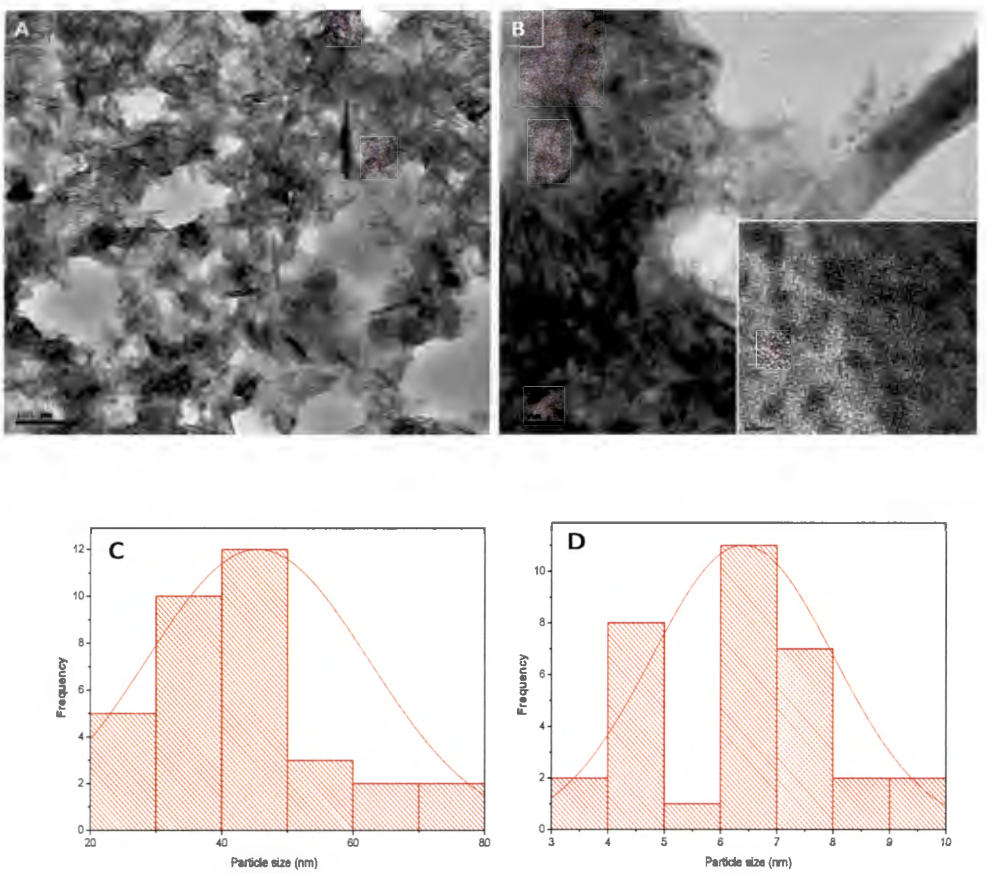

Figure 4.13: TEM micrograph of Mn doped Bi_2S_3(1)prepared from $[\mathbf{Bi(L^1)_3}]$ at **(a)** low magnification, **(b)** high magnification, inset-HRTEM showing lattice fringes; with corresponding particle size histogram showing **(c)** width and **(d)** length of the nanorods.

Figure 4.14 represents the micrograph of Mn doped Bi_2S_3(2) nanoparticles synthesized from **[Bi(L^2)$_3$]**. The doped nanomaterial appear smaller in diameter when compared with the undoped Bi_2S_3 nanorods. The particles have width in the range of 4 to 16 nm and length between 40 to 160 nm. Estimated aspect ratio for these nanorods is 10 nm.

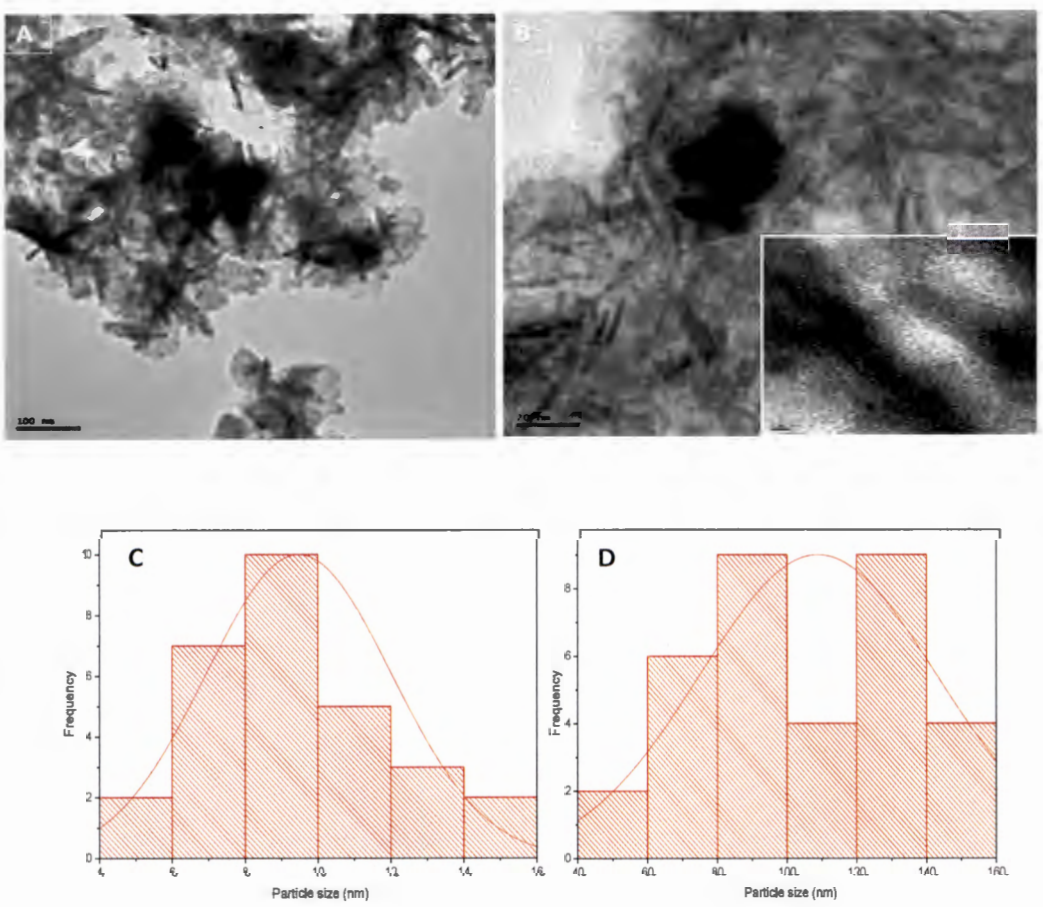

Figure 4.14: TEM images of Mn doped Bi_2S_3(2) prepared from **[Bi(L^2)$_3$]** at **(a)** low magnification, **(b)** high magnification, inset-HRTEM showing lattice fringes; with corresponding particle size histogram showing **(c)** width and **(d)** length of the nanorods.

Figure 4.15a and 4.15b show the TEM micrograph of Sn doped Bi_2S_3(1) at low and high magnification respectively. Rod shaped Bi_2S_3 nanomaterials were embedded in web-like materials. Although the particles were few, they appeared clearly visible at lower magnification than at high magnification. Like the other doped Bi_2S_3 the Sn-doped Bi_2S_3 exhibited lattice fringes which was an indication of the crystallinity of Sn-doped Bi_2S_3(1). Particle size distribution histogram revealed a narrow and wide particle size distribution for the width and length of the nanorods.

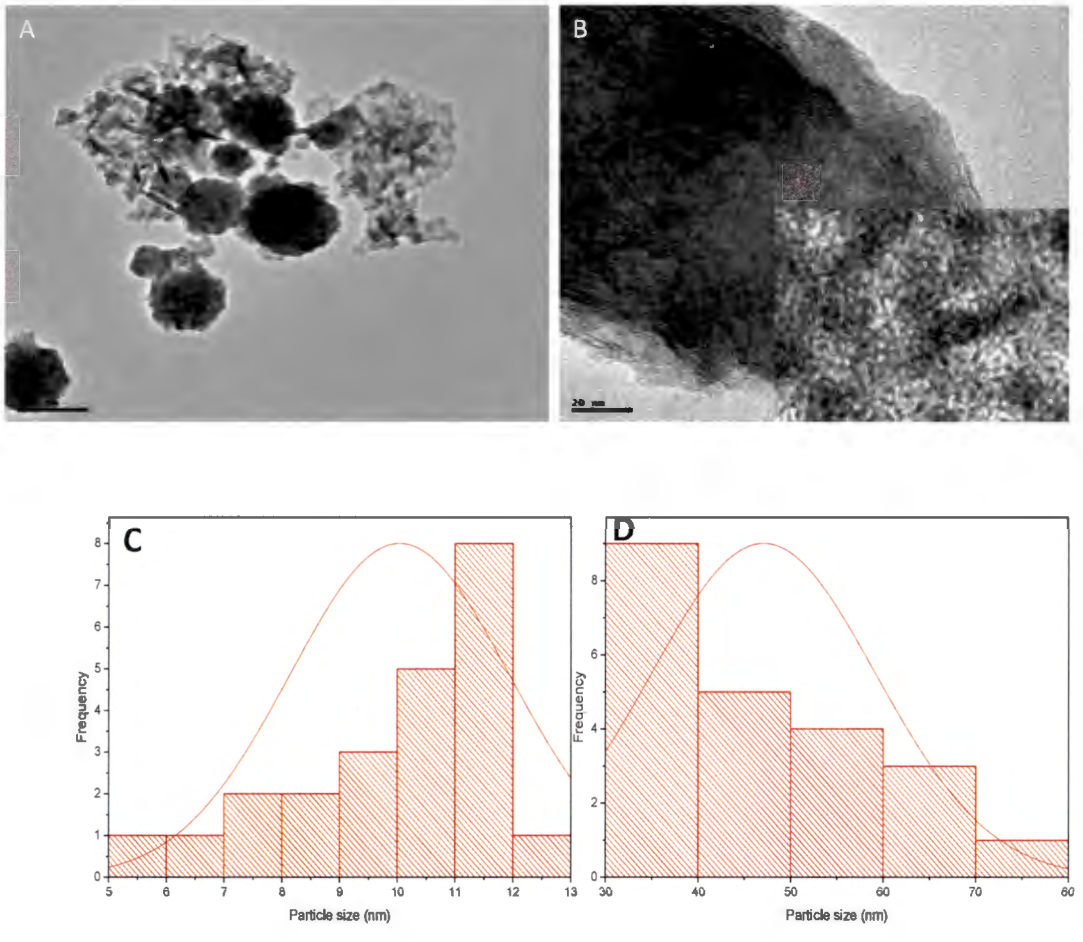

Figure 4.15: TEM images of Sn doped Bi_2S_3(1) prepared from **[Bi(L^1)$_3$]** at **(a)** low magnification, **(b)** high magnification, inset-HRTEM showing lattice fringes; with corresponding particle size histogram showing **(c)** width and **(d)** length of the nanorods.

Interestingly, the micrograph of Sn doped Bi_2S_3(2) nanorods shown in Figure 4.16a and 4.16b were covered by semi-transparent creased and wrinkle materials layers. The dimension of these

nanorods was measured in terms of length and width. The observed average size of the width was 7.19 nm while the length was 83.29 nm. Size distribution in terms of the width was narrow but the size distribution of the length was wide. This was apparent from the particle size distribution histogram that is presented in Figure 4.16c and 4.16d. Inset is the HRTEM that shows lattice fringes which indicate the crystallinity of the nanomaterial.

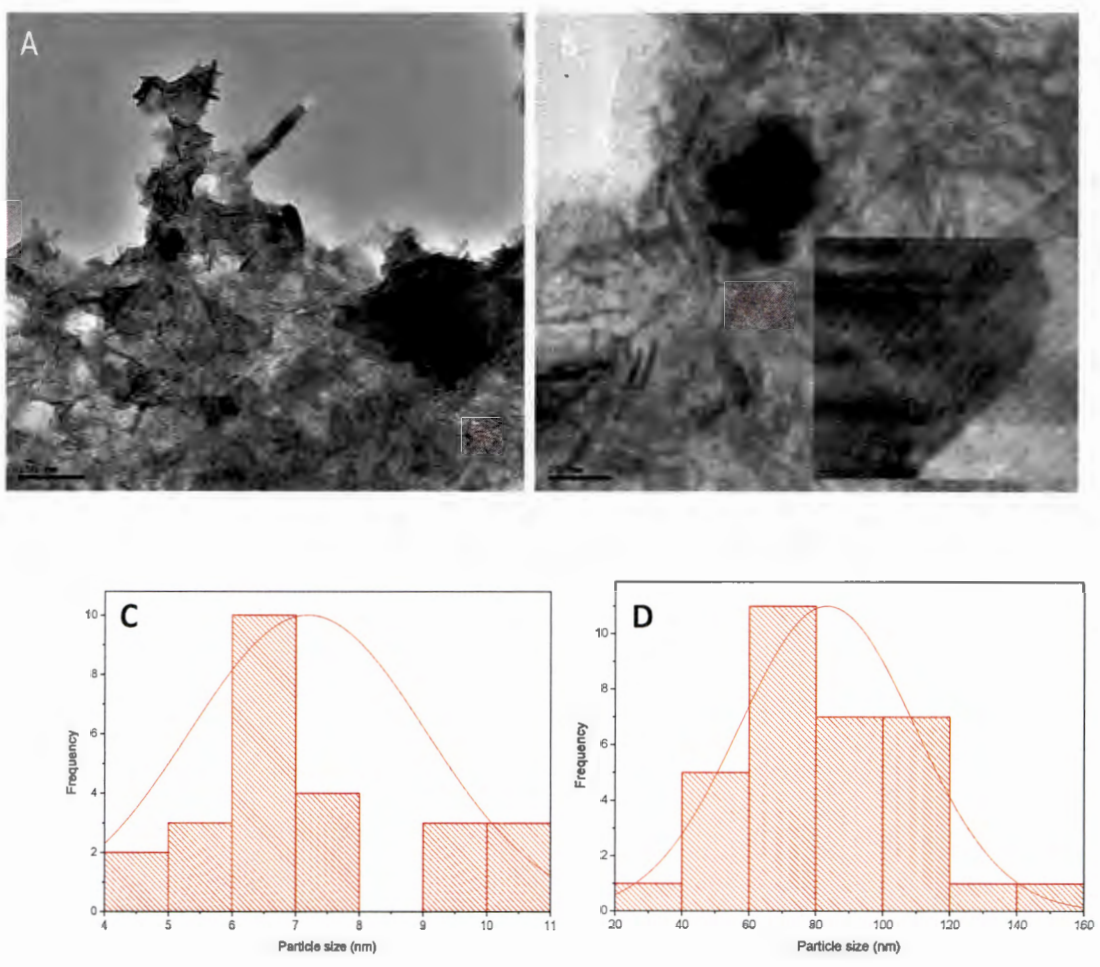

Figure 4.16: TEM images of Sn doped Bi_2S_3(2) prepared from **[Bi(L^2)$_3$]** at **(a)** low magnification, **(b)** high magnification, inset-HRTEM showing lattice fringes; with corresponding particle size histogram showing **(c)** width and **(d)** length of the nanorods.

4.3 EDX analysis of Bi_2S_3 doped with Mn ions

4.3.1 EDX analysis

In order to ascertain and confirm the presence of the dopants (Mn and Sn) within the doped bismuth sulphide, the samples were subjected to EDX analysis, which is an analytical technique that showed the percentage composition of elements present in a material. The percentage weight for the Mn and Sn ion were successfully estimated by the EDX analysis. Figure 4.17a-c and 4.18a-c show the EDX of Mn and Sn doped Bi_2S_3 obtained from **[Bi(L^1)$_3$]**, **[Bi(L^2)$_3$]**, and **[Bi(L^3)$_3$]** respectively. The spectra showed the results of the final products as composed of Mn, Bi and S for the Mn doped Bi_2S_3 nanomaterials, and Sn, Bi, and S for the Sn doped Bi_2S_3nanomaterials respectively without any other elements. The presence of the Mn and Sn is an indication that the Bi_2S_3 was successfully doped.

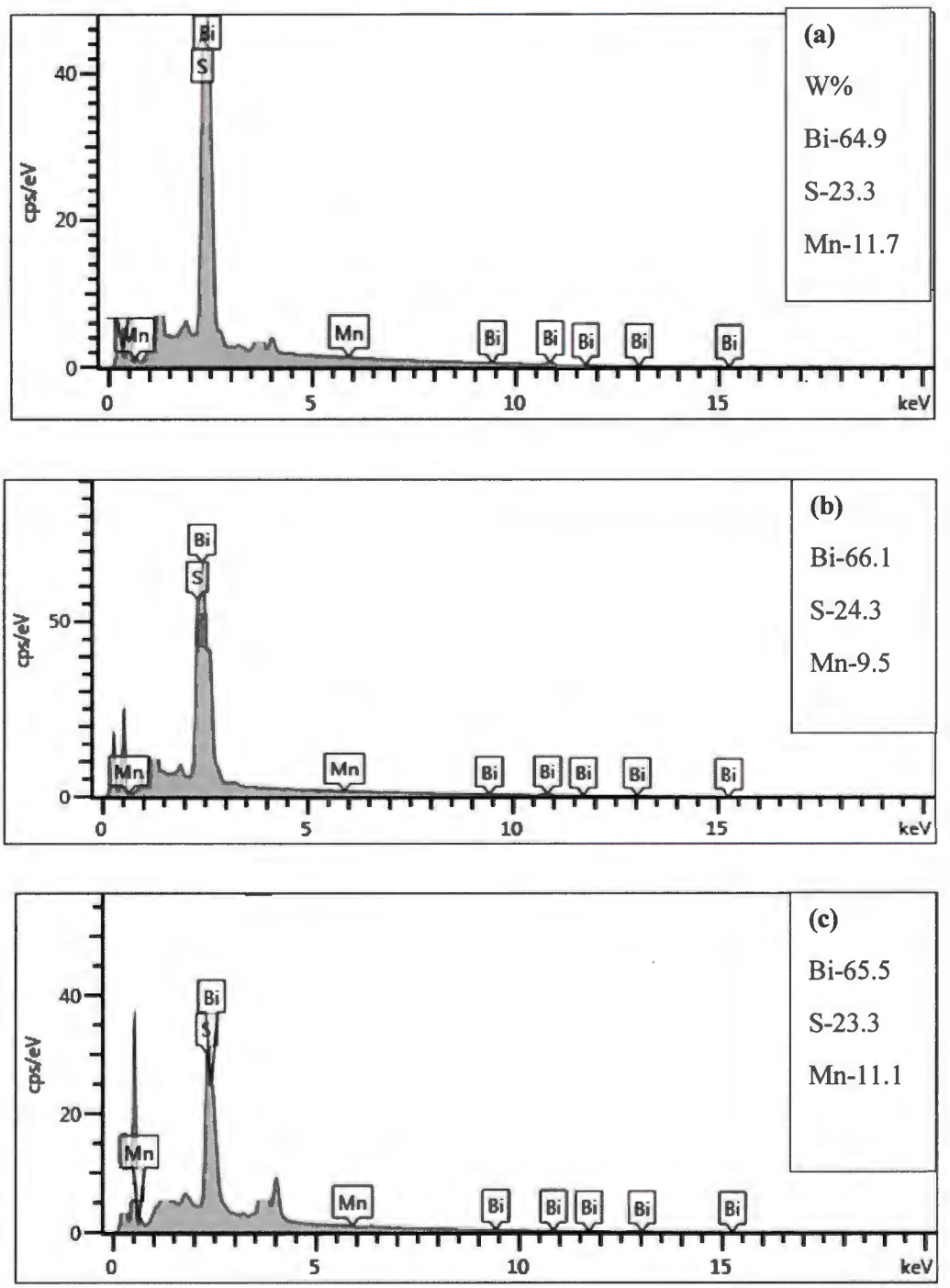

Figure 4.17: EDX spectra of Mn doped Bi_2S_3 obtained from **[Bi(L^1)$_3$]**, **[Bi(L^2)$_3$]**, and **[Bi(L^3)$_3$]**.

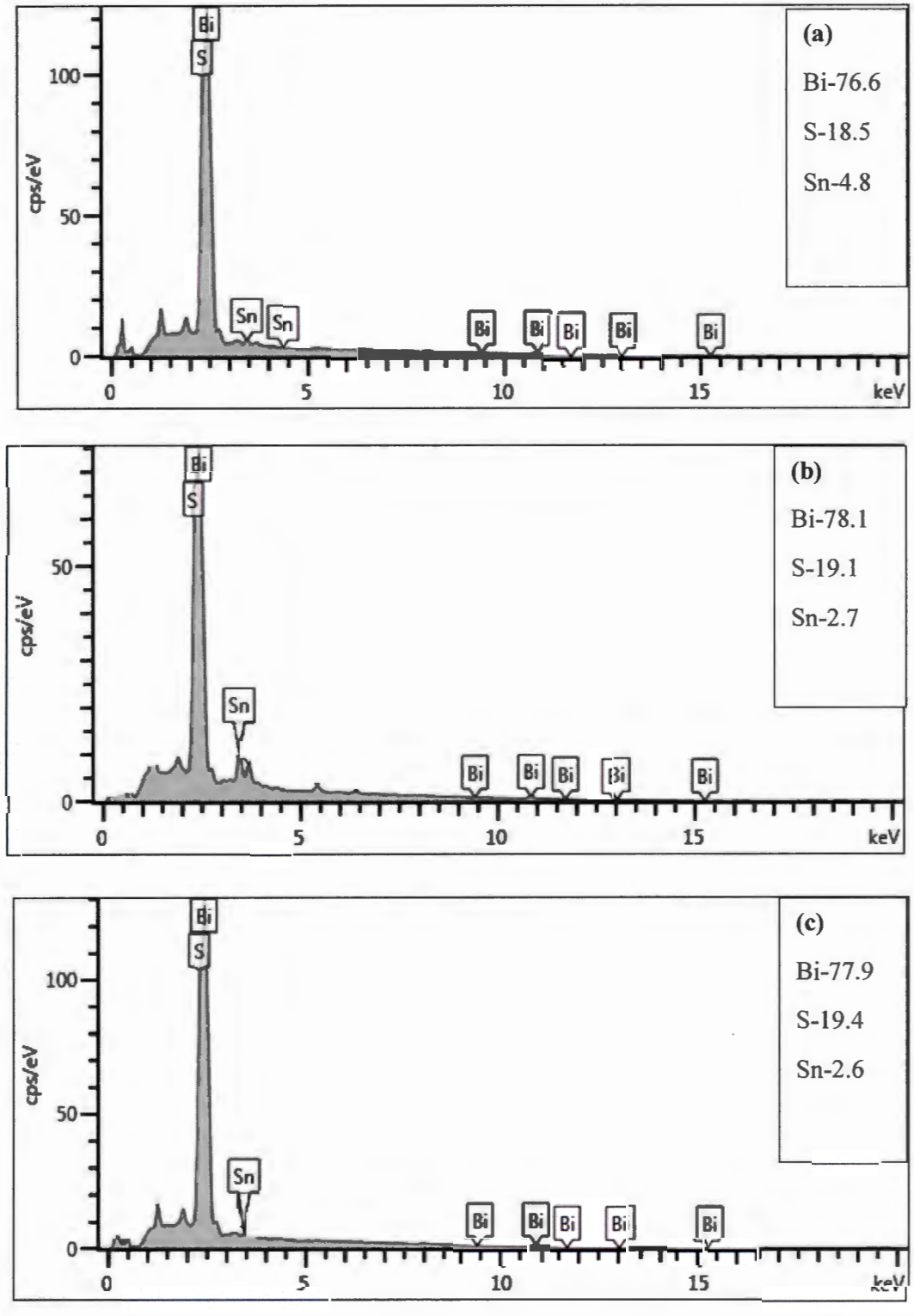

Figure 4.18: EDX spectra of Sn doped Bi_2S_3 obtained from $[Bi(L^1)_3]$, $[Bi(L^2)_3]$, and $[Bi(L^3)_3]$.

4.4 UV-vis studies

UV-vis spectroscopy gives an insight into the understanding of the optical band gap of nanomaterials. In semiconductor nanomaterials, the optical excitation of electrons across the band gap is allowed. This process produces an abrupt increase in absorption at the wavelength which corresponds to the band gap energy. This feature, in the optical spectrum, is known as the optical absorption edge [15, 16]. The position of the band edge and shape of the absorption shoulder are dependent on some properties of the synthesized nanomaterials, such as shape, size and size distribution. It is also strongly dependent on the type of surfactants used in the synthesis process. In semiconductor NPs, size estimation could be deduced from the position of the absorption band edge. Unlike the other methods of particle size determination, size determination from absorption spectra is not affected by the presence of aggregates. This is because the electronic coupling between particles in an aggregate is sufficiently weak. Hence, the resultant spectrum is determined by the primary particles only [17].

4.4.1 Tauc plots of Bi_2S_3

A plot of $(\alpha h\nu)^2$ versus $h\nu$ for a direct band estimated by the value of a x-axis intercept of $(\alpha h\nu)^2$ versus $h\nu$ provides a measure of the transition energy [18]. Figure 4.19a, 4.19b and 4.19c represent the UV-vis spectra of Bi_2S_3 obtained from **[BiL^1$_3$]**, **[BiL^2$_3$]** and **[BiL^3$_3$]** complexes respectively. Figure 4.19a shows the UV-vis spectrum of Bi_2S_3(1) derived from **[BiL^1$_3$]** with absorption peak at 580 nm and absorption edge at 613 nm. The band gap energy of the Bi(III) complexes was calculated using Jan Tauc plot [19].

The Tauc equation is represented as follows:

$\alpha h\nu = D(h\nu - E_g)^n$ .... (1)

where, $h\nu$ = the energy of incident photon

α = linear absorption coefficient of the material

E_g= optical bandgap energy

D = constant and n = 2 as exponential for indirect bandgap semiconductors.

From the Tauc plot, the band gap were about 2.02, 2.04 and 2.26 eV for the Bi_2S_3(1), Bi_2S_3(2), and Bi_2S_3(3), prepare from [**Bi(L^2)$_3$**], [**Bi(L^2)$_3$**], and [**Bi(L^2)$_3$**] respectively.

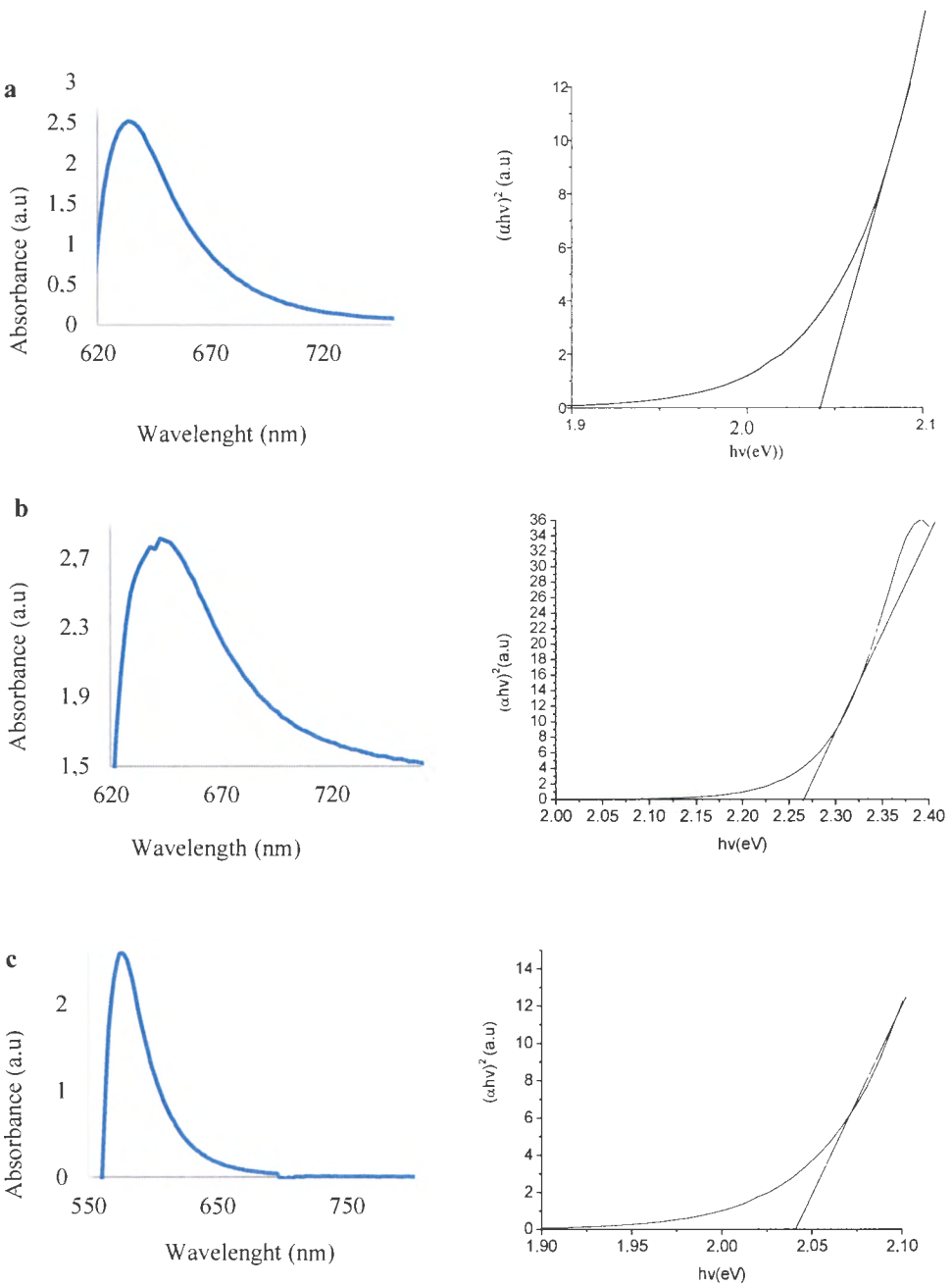

Figure 4.19: UV-vis spectra of Bi_2S_3 nanorods prepared from (a) [**BiL^1_3**] (b) [**BiL^2_3**] and (c) [**BiL^3_3**] and their corresponding plots of $(\alpha hv)^2$ versus hv.

4.4.1 UV-vis of Mn doped Bi_2S_3

The absorption spectra of Mn-doped Bi_2S_3nanorods are shown in Figure 4.20. The optical absorption band gap estimated using Tauc plot for the doped Bi_2S_3 was in the range of 1.64 to 1.76 eV (figure 4.20a & b). These were lower than the value obtained for undoped Bi_2S_3. It showed that Mn doping caused a notable red shift of the absorption edge. This could be due to the fact that doping offers more valence electrons, which could be excited easily into free carriers by photons. Hence, Mn doping introduced a donor level under the conduction band of Bi_2S_3, leading to a narrower band gap [20]. This phenomenon was a typical consequence of quantum effect and could be explained thus: as particle size fell into nanoscale, the movement of electrons would be confined more intensively, resulting in the differentiation near the Fermi level which would broaden the band gap [21].

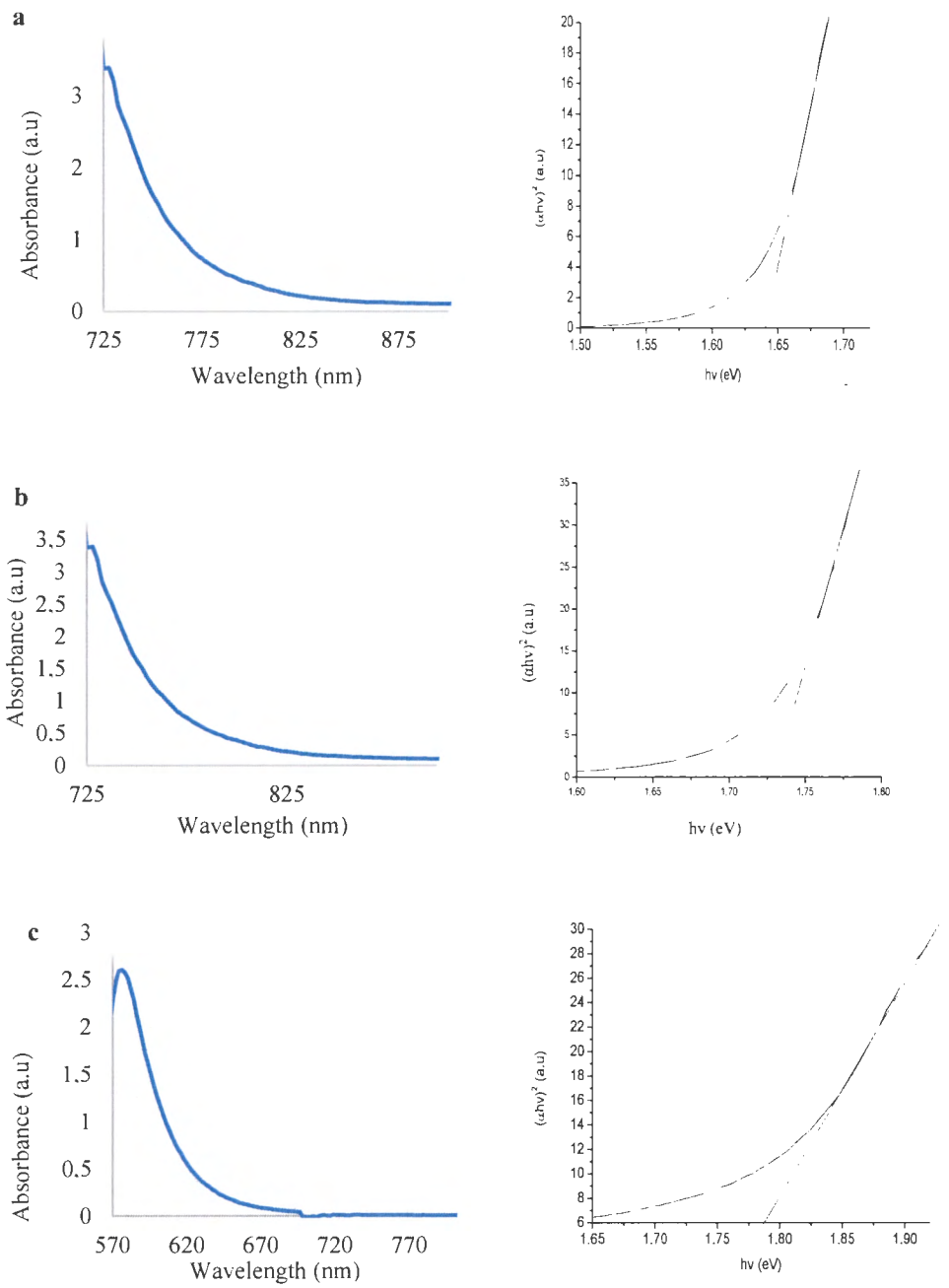

Figure 4.20: UV-vis spectra Mn doped Bi_2S_3 nanomaterials prepared from (a) [**Bi(L^1)$_3$**], (b) [**Bi(L^2)$_3$**] and [**Bi(L^3)$_3$**]; and their corresponding plot of $(\alpha hv)^2$ versus hv.

Figure 4.21 shows the UV-vis absorption spectrum of Sn doped Bi_2S_3 nanorods obtained by analysing the dissolved as-prepared Sn-doped sample in toluene. UV-vis absorption peak was observed around 640 – 730 nm, while the absorption edge was found to extend beyond 730 nm. The optical band gap energy was estimated using the Tauc plot and was found to be in the range 1.67 to 1.74 eV. A red shift was also observed between the undoped and the doped Bi_2S_3 nanomaterial. Ando *et al,* has ascribed red shift upon the introduction of doping material as a consequence of the substitution of the metal ion in the crystal lattice of the substrate materials (in this case bismuth ion-Bi^{3+}) by the dopant. In general, it was reported that different doping ion exhibit different effects on the absorption spectra of the nanomaterials of interest [22].

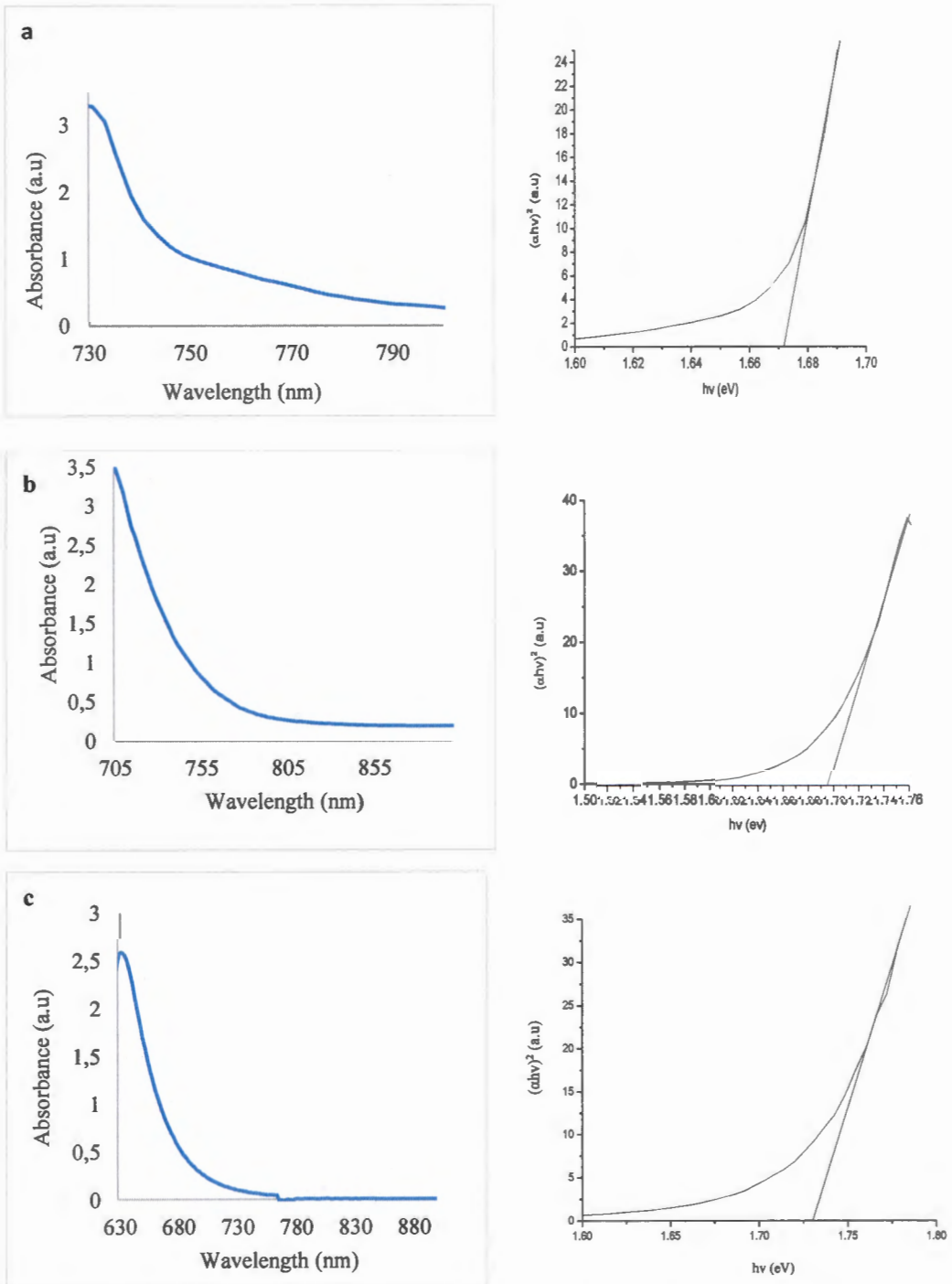

Figure 4.21: UV-vis spectra Sn doped Bi_2S_3nanomaterials prepared from (a) **[Bi(L^1)$_3$]**, (b) **[Bi(L^2)$_3$]** and **[Bi(L^3)$_3$]**; and their corresponding plot of $(\alpha h\nu)^2$ versus hν.

4.5 Evaluation of photocatalytic property

Methylene blue (MB) was used as a model pollutant in this work in order to evaluate the photocatalytic performance of the Bi_2S_3 in aqueous solution using irradiation time as variable parameter. Theoretically, upon irradiation of semiconductors with the appropriate band structure, they absorb energy and it is higher than their band gap. A photoexcited electron is promoted from the valence band to the empty conduction band, and leaving behind a hole in the valence band. These photo-generated excitons (electrons and holes) are separated and migrate to the particle surface. This is followed by the generation of various reactive oxygen species, such as hydroxyl radicals and superoxide anions, and possibly oxygen which is generated from water. These active species are capable of oxidising a wide range of organic chemical substrates with no selectivity [23,24].

The wavelength of maximum absorption for MB is 664 nm which is due to the absorption of the π- system [25]. MB can be degraded either by oxidative degradation of the MB molecule or by a two-electron reduction [26,27]. The photodegradation efficiency of the synthesized Bi_2S_3 on the MB is shown in Figure 4.22-4.24, while the doped Bi_2S_3 using only samples obtained from complexes **[Bi(L^1)$_3$]** and **[Bi(L^2)$_3$]**are presented in Figures 4.25-4.28. The UV–vis spectra of the original and degraded MB solutions were determined by a UV–vis spectrophotometer at 15 min time interval within 150 min. The absorption peaks of the MB solutions at 664 nm gradually declined with time in the presence of the nanoparticles due to an oxidative degradation process [28]. This indicates the degradation of the MB in the aqueous solutions. The absence of any new peak indicates that no intermediates were produced during the degradation. The photocatalytic activity of Bi_2S_3photocatalysts for MB photodegradation was calculated as follows:

$$\text{Degradation } \% = \frac{A_c - A_t}{A_c} \times 100 \qquad (1)$$

where A_c is the initial solution of dye concentration and;

A_t is the final solution of dye concentration after treating with the photocatalyst

In the bare Bi_2S_3 nanomaterials, the efficiency of the dye degradation was in the range 82-87%. However, the efficiency showed an increase above 90% with the doped samples. Compared to the undoped Bi_2S_3, the metal doped Bi_2S_3 nanorods has higher photocatalytic activity which might be attributed to the photo-generated electrons and holes recombination that were prevented by doping Sn and Mn. In addition the energy from absorbed photons can be efficiently transferred to the dopant which is utilized in the excitation and increases the rate of reactions on the surface of NPs [29].

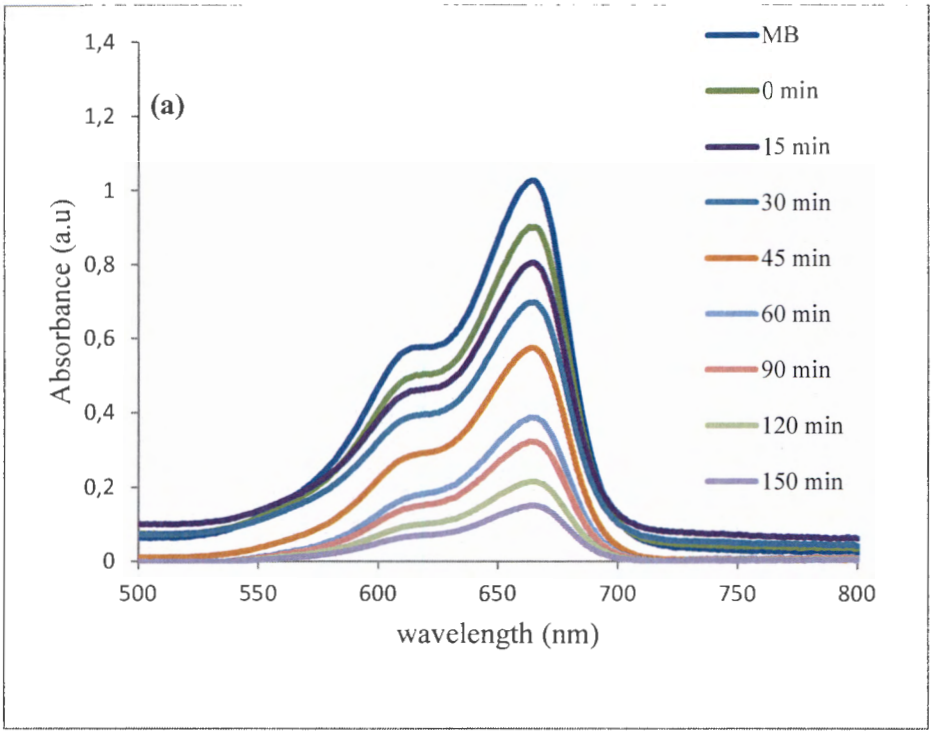

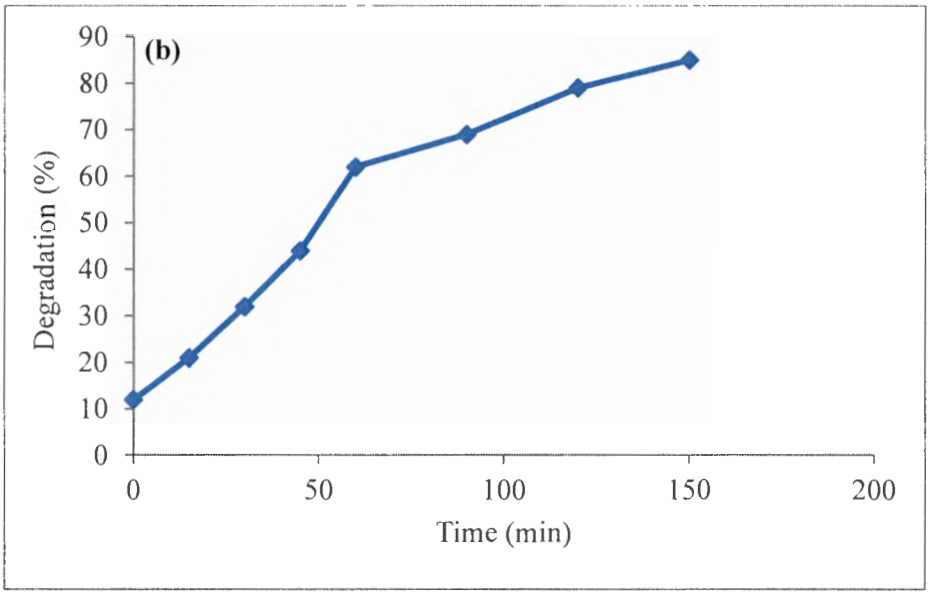

Figure 4.22: (a) The absorption spectra of aqueous MB at different time intervals, and (b) percentage degradation of MB with change in time, using Bi_2S_3(1) prepared using **[Bi(L^1)$_3$]**.

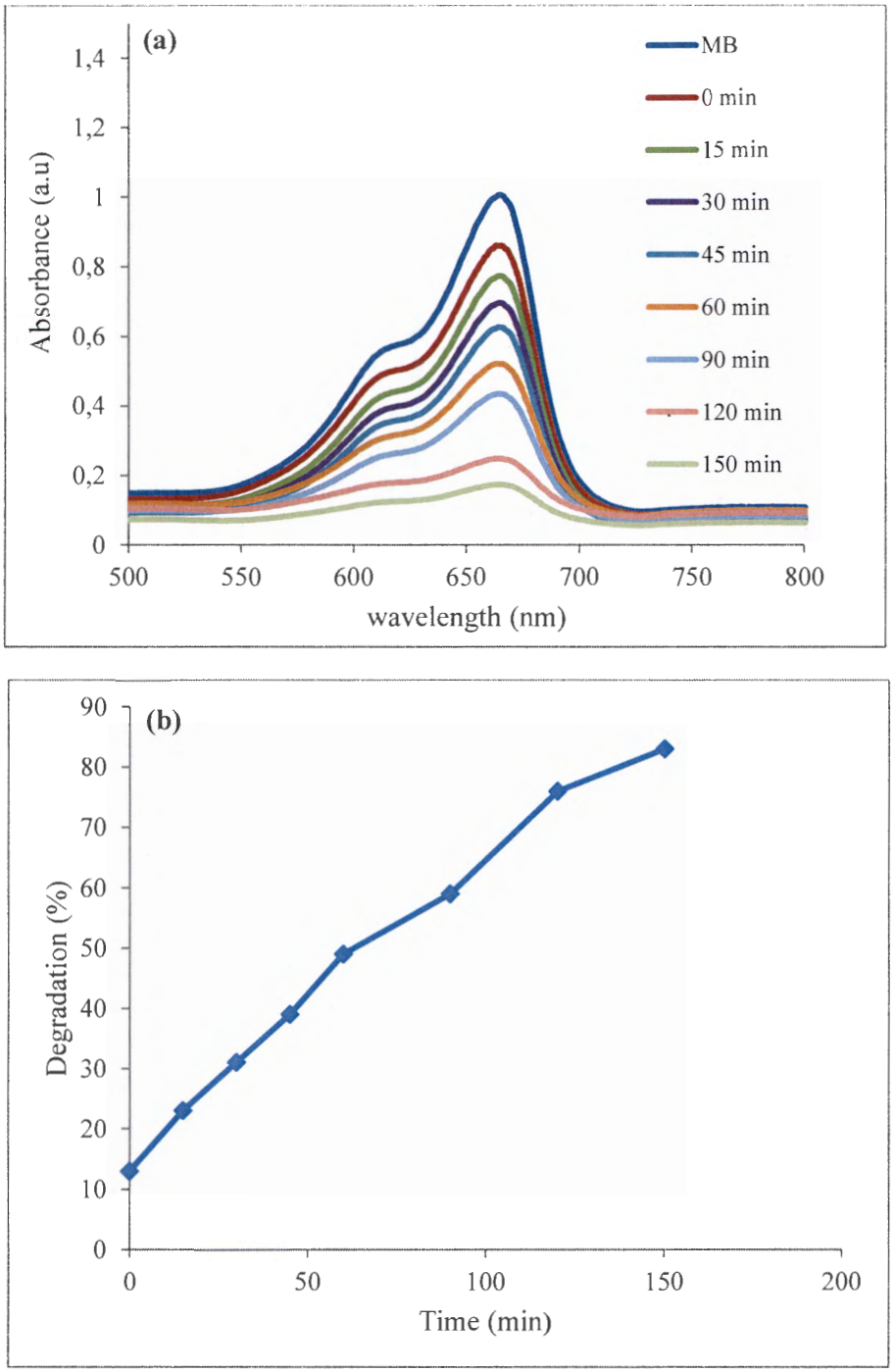

Figure 4.23: (a) Absorption spectra of aqueous MB at different time intervals, and (b) percentage degradation of MB with change in time, using Bi_2S_3(2) prepared using [**Bi(L^2)$_3$**].

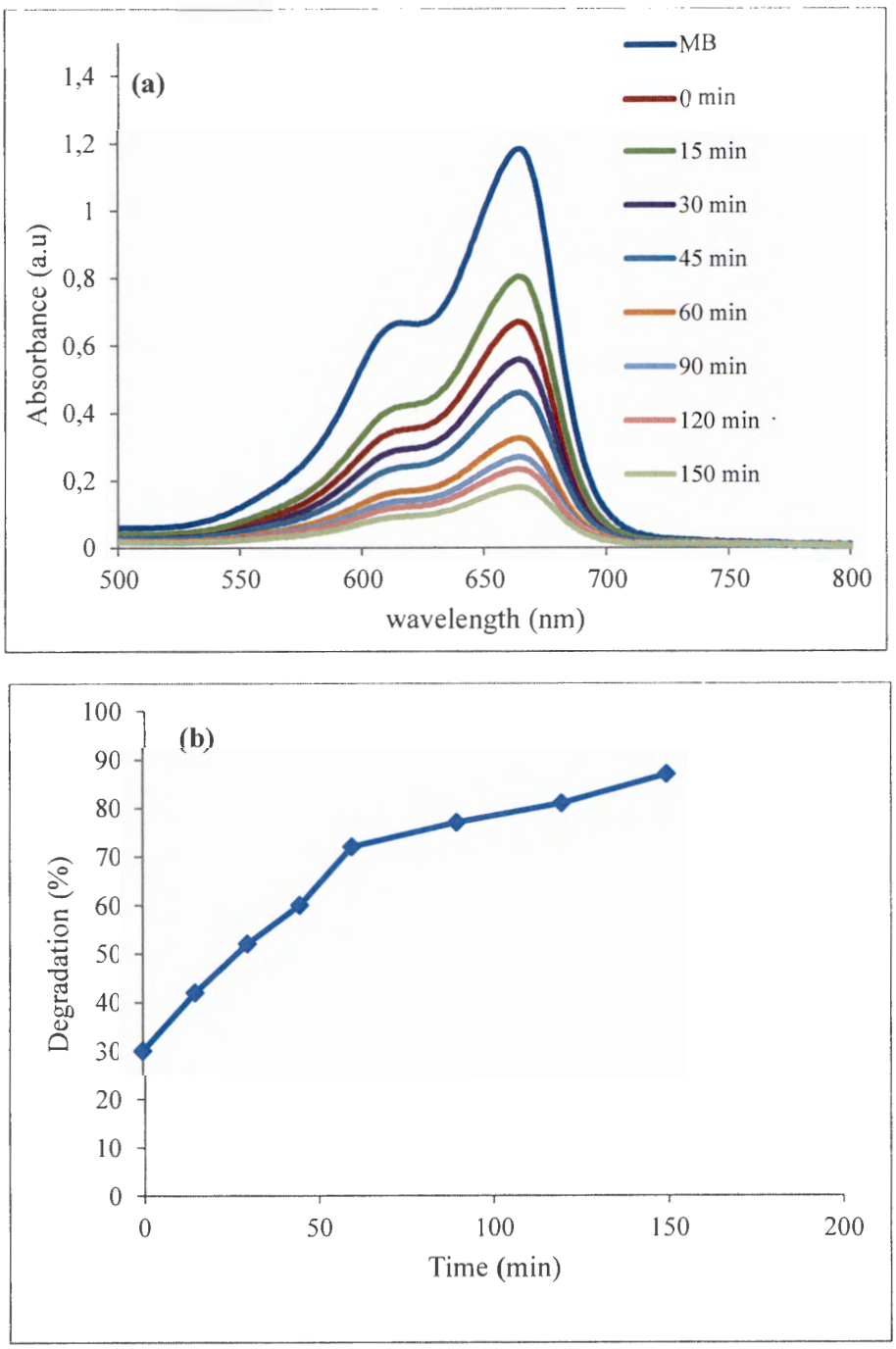

Figure 4.24: (a) Absorption spectra of aqueous MB and (b) percentage degradation of MB using Bi_2S_3(3) prepared using **[Bi(L^3)$_3$]**.

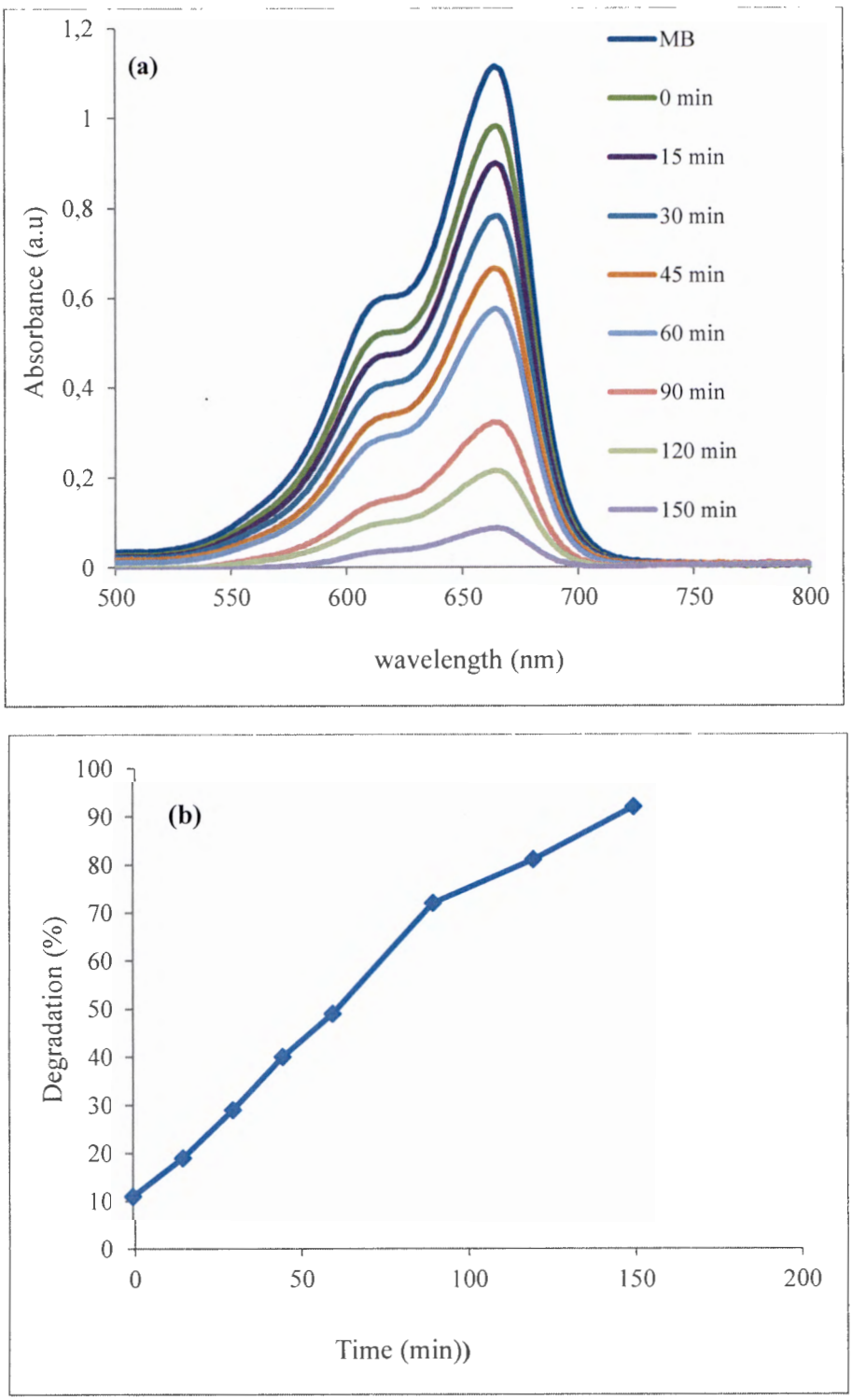

Figure 4.25: (a) Absorption spectra of aqueous MB and (b) percentage degradation of ME using Sn doped Bi_2S_3(1).

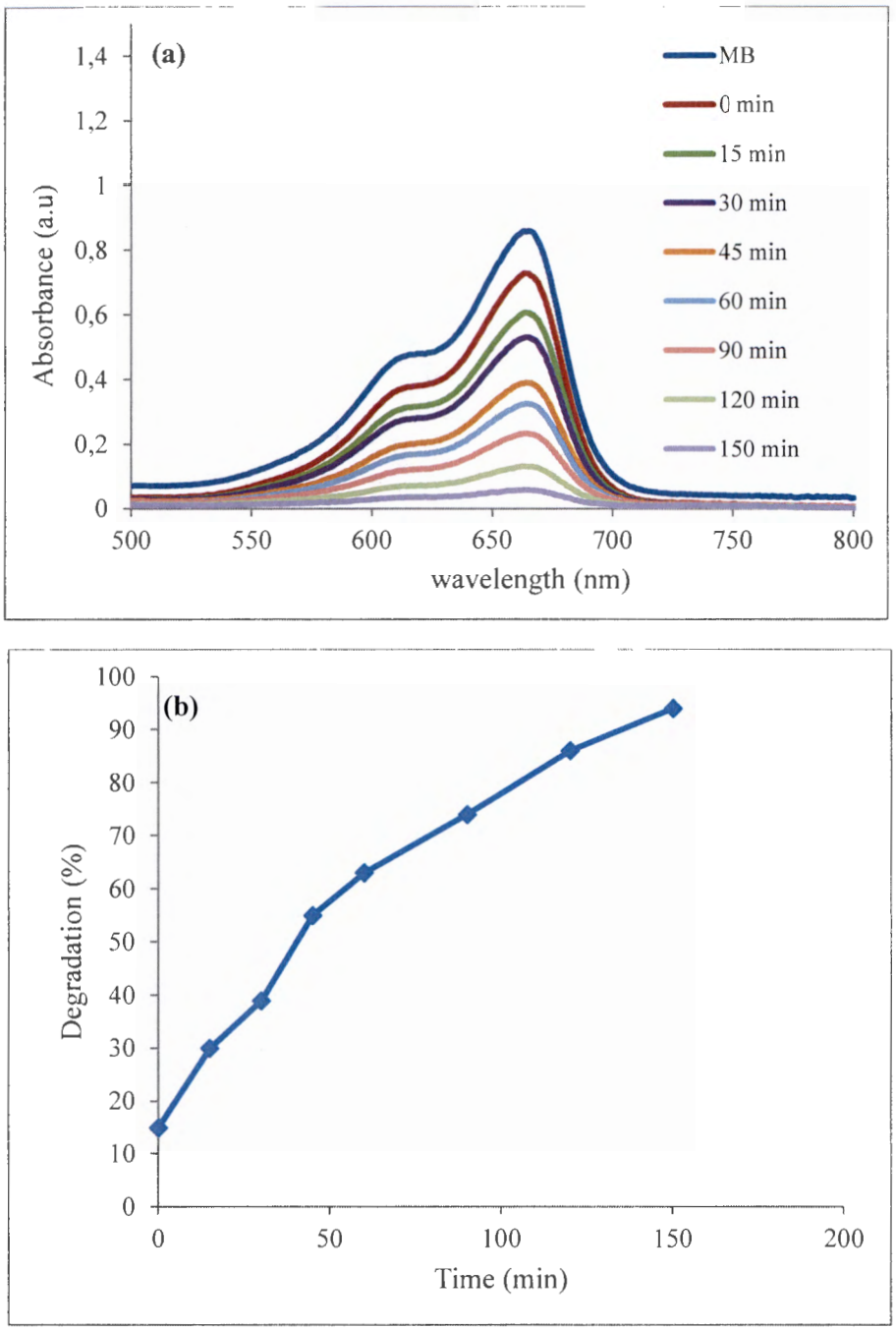

Figure 4.26: (a) Absorption spectra of aqueous MB, and (b) percentage degradation of MB using Sn doped Bi_2S_3(2).

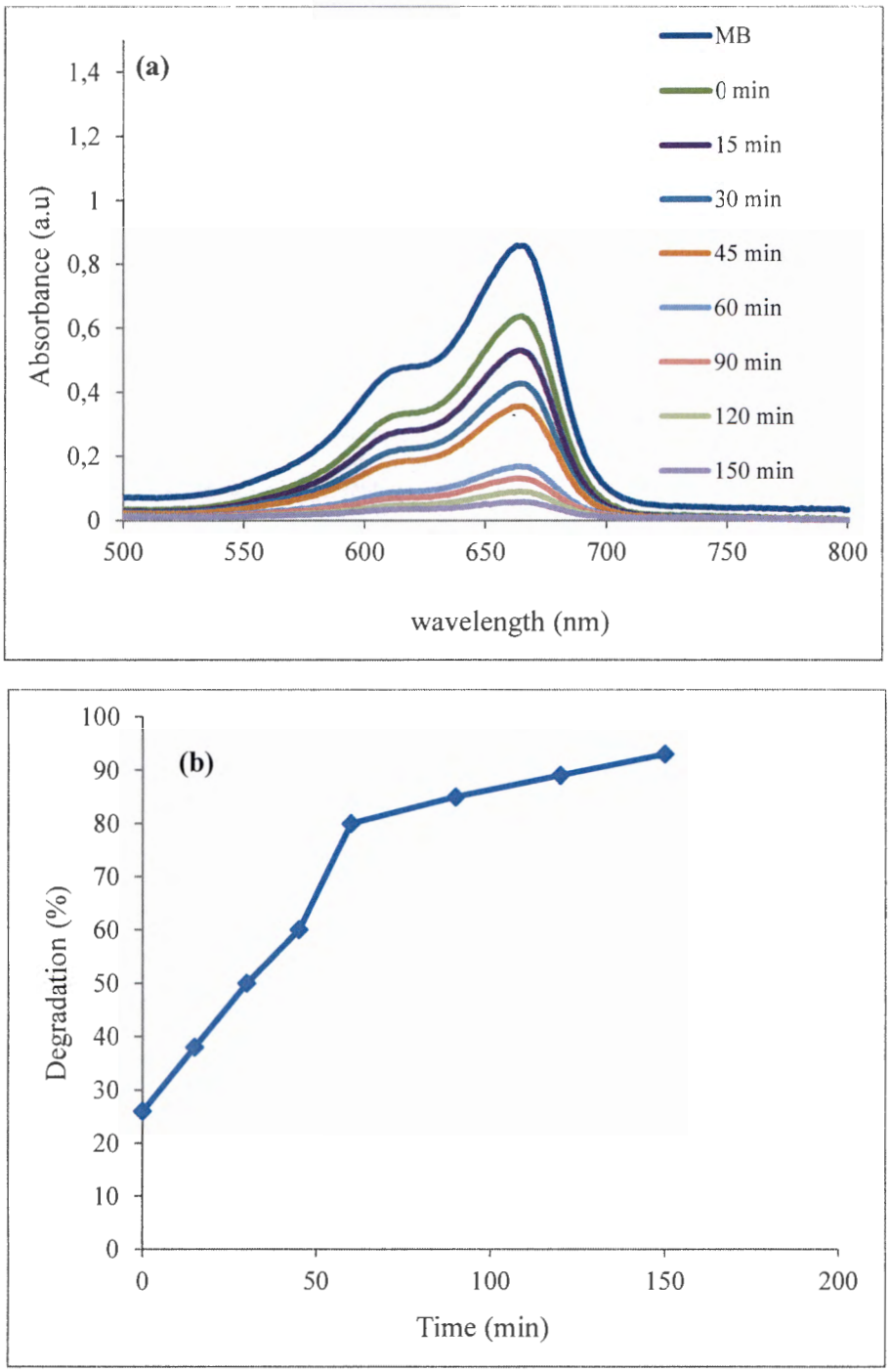

Figure 4.27: (a) Absorption spectra of aqueous MB and (b) percentage degradation of MB using Mn doped Bi_2S_3(1).

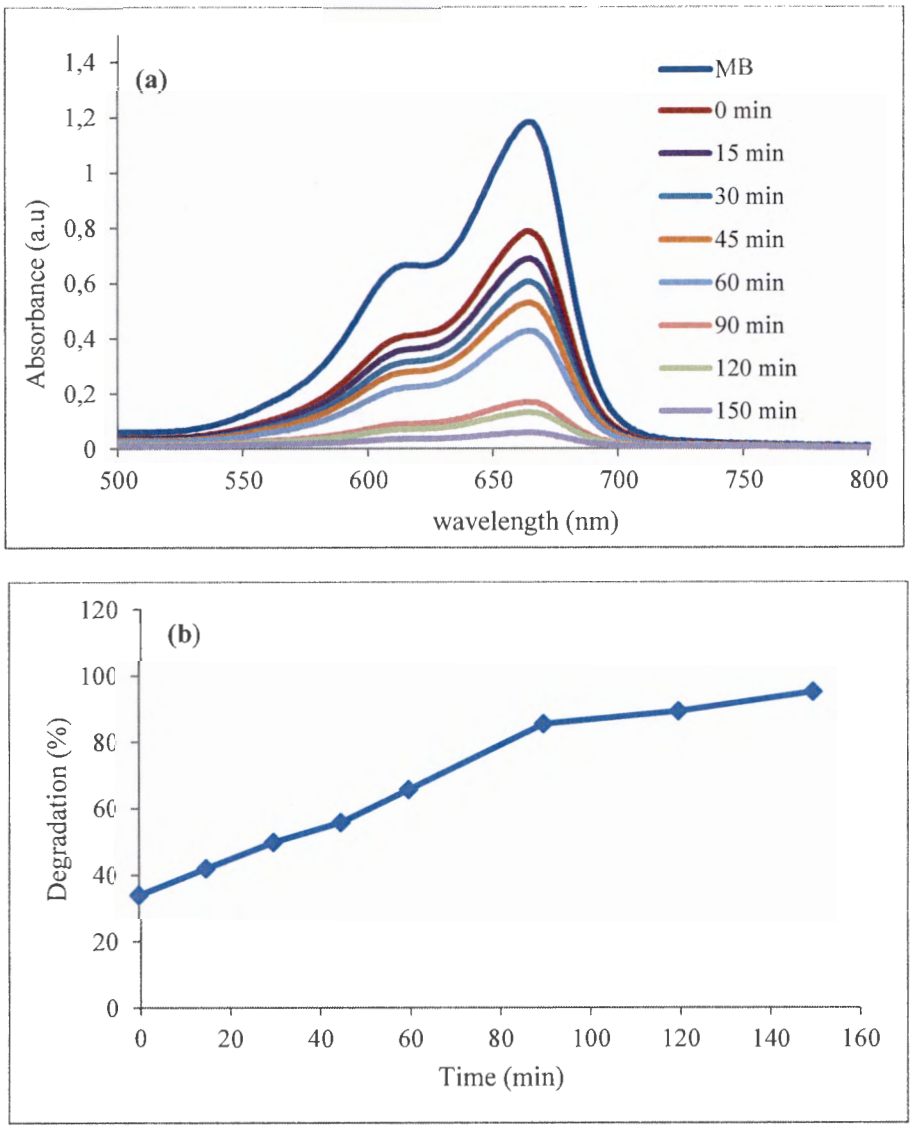

Figure 4.28: (a) The absorption spectra of aqueous MB and (b) percentage degradation of MB using Mn doped Bi_2S_3(2).

4.6. MB degradation process

The photocatalytic results showed pronounced reduction in the intensities of the bands at 664 and 290 nm. These suggest that both the chromophore and aromatic parts of methylene blue were broken down in the reaction process. The photocatalytic degradation of MB by semiconductor Bi_2S_3 is not a consequence of a direct redox reaction between the Bi_2S_3 nanomaterials and the MB molecules. The pathway for the photocatalytic degradation of MB in water has been proposed by Houas *et al.* [29]. During photo-enhance degradation, the electrons which were generated in the Bi_2S_3 under the irradiation of visible light would either recombine with the holes of the valence band or react with the adsorbed oxygen on the surface of Bi_2S_3. In the latter case, oxygen ions are created, which in turn combine with the adsorbed water molecules to form hydroxyl radicals $^{\bullet}OH$. Eventually, the reactions of MB with the radicals cause the degradation of the dye molecules. The sequence of this process could be itemized as follows:

The activation of Bi_2S_3 by incident light ($h\upsilon$) generates excitons (electron-hole pairs), which are powerful oxidizing and reducing agents, respectively following the equation [30]:

$$Bi_2S_3 + h\nu \rightarrow e^- + h^+ \quad (1)$$

The oxidation of the adsorbed water molecules on the surface of Bi_2S_3 results into the production of hydroxyl radical according to reaction:

$$H_2O \rightarrow H^+ + {}^{\bullet}OH \quad (2)$$

This is followed with the reduction and oxidation reactions as follows:

$$\text{Reduction-}\ OH^- + h^+ \rightarrow {}^{\bullet}OH, \quad (3)$$

$$\text{Oxidation-}\ O_2 + e^- \rightarrow O_2^- \quad (4)$$

Finally, the degradation of the organic compound (MB) occurs:

$$MB + {}^{\bullet}OH \rightarrow \text{products } (CO_2 + H_2O + NH_4^+ + NO_3^- + SO_4^{2-} + Cl^-) \quad (5)$$

The doping of the Bi_2S_3 nanomaterials was beneficial to the photocatalytic activity of Mn and Sn-doped Bi_2S_3.

The degradation process, showing the energy diagram with the different band levels position, are shown in Figure 4.6.

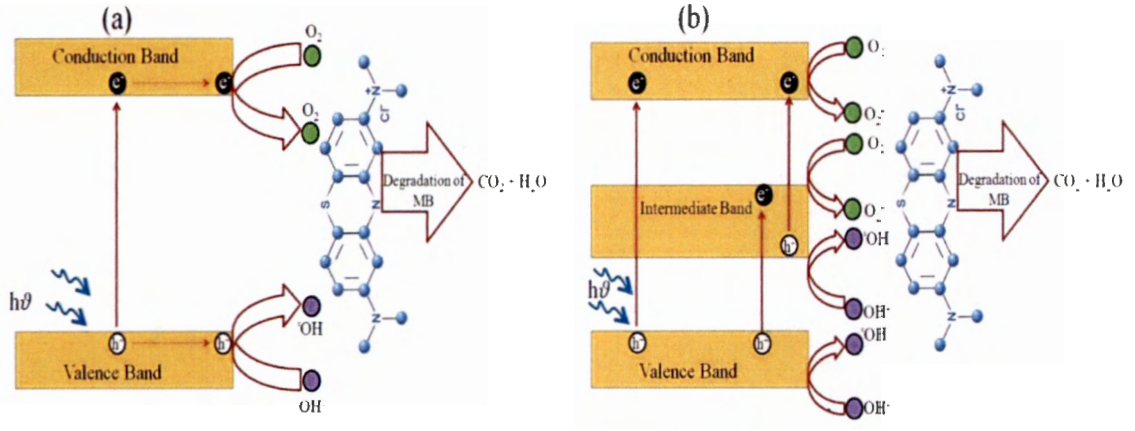

Figure 4.29: Schematic representation of degradation of MB in (a) pure Bi_2S_3, (b) metal doped Bi_2S_3 with intermediate band [30].

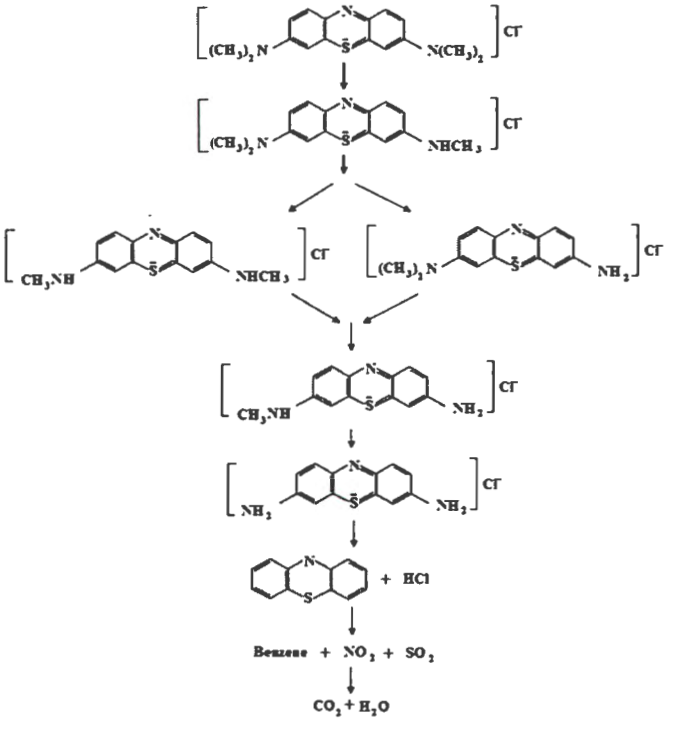

Scheme 4.1: Chemical structure of MB and the photocatalytic reaction pathway [31].

The UV-vis spectra of Bi_2S_3 nanomaterials showed the maximum absorption band centered at 655 nm. UV light alone could not induce complete decolourization of the MB dye. But when irradiated in presence of Bi_2S_3 nanomaterials, UV light led to complete decolourization of the dye. The absorption band at 655 nm decreased and disappeared. When the size of bulk metals goes to the nanoscale, electron transfer is more efficient as compared to the bulk material [32, 33].

The role of metal doped NPs in decolourization is to control the behaviour of materials, through many technologies and for this reason; researchers have begun to explore the use of dopants to influence the properties of semiconductor nanoparticles [34]. The energy from absorbed photons can be efficiently transferred to the dopant which are utilized in the excitation and increases the rate of reactions on the surface of NPs [35]. The curves of the degradation of MB dye over Sn doped $Bi_2S_3$are about 92-94% and Mn doped Bi_2S_3 around 93-96% which is much better than the Sn doped. These is because of the adsorption of the as-prepared samples are different, it goes smaller with the mole ratio of Sn increased, which could owe to the enlarged specific surface area [34].

REFERENCES

[1] N. Hollingsworth, A. Roffey, H.U. Islam, M. Mercy, A. Roldan, W. Bras, M. Wolthers, C.R.A. Catlow, G. Sankar, G. Hogarth, N.H. De Leeuw, Chem. Mater. 26 (2014) 6281.

[2] S. N, Vercellotti, G. White J, A.Fegan, C.Wagner, Bischof, Mol.Pharm. 9 (2012) 2146.

[3] Y. Jiang, Y.J. Zhu, Z.L. Xu, Mater. Lett. 60 (2006) 2294.

[4] Z.J. Yang, J.K. Song, M.B. Zheng, S.T. Liao, H.Q. Chen, G.B. Ji, H.Y. Wang, J.M. Cao, Acta Chim. Sinica. 66 (2008) 2558.

[5] X.H. Liao, H. Wang, J.J. Zhu, H.Y. Chen, Mater. Res. Bull. 36 (2001) 2339.

[6] T. Thongtem, C. Pilapong, J. Kavinchan, A. Phuruangrat, S. Thongtem, J. Alloys Compd. 500 (2010) 195.

[7] Y. Jiang, Y.J. Zhu, J. Phys.Chem. 109B (2005) 4361.

[8] J. Lu, Q. Han, X. Yang, L. Lu, X. Wang, Mater. Lett. 61 (2007) 2883.

[9] Wen-hui Li, Mater. Lett. 62 (2008) 243.

[10] M. Zhang, D.J. Chen, R.Z. Wang, J.J. Feng, Z. Bai, A.J. Wang, Mater. Sci. Eng. 33C (2013) 3980.

[11] P. Marchand, C. J. Carmalt, Coord. Chem. Rev. 257 (2013) 3202.

[12] F. Chen, D. Jia, Y. Cao, X. Jin, A. Liu, Ceram. Int. 41 (2015) 14604

[13] A. Mauracher, O. Echt, A.M. Ellis, S. Yang, D.K. Bohme, J. Postler, A. Kaiser, S. Denifl, P. Scheier, Phys. Rep. 751 (2018) 1

[14] M.A. Malik, P. O'Brien, N. Revaprasadu, Sulfur Silicon Relat. Elem. 180 (2005) 689

[15] S. Boldish, W. White, Am. Mineral. 83 (1998) 865.

[16] V. Kumar, S. Sharma, T. Sharma, V. Singh, Opt. Mater. 12 (1999) 115.

[17] M. Agata, H. Kurase, S. Hayashi, K. Yamamoto, Solid State Commun. 76 (1990) 1061.

[18] H.B. Li, L.L.Chai, X.Q.Wang, X.Y. Wu, G.C.Xi, Y.K. Liu, Y.T Qian, Cryst. Growth Des. (2007) 1918.

[19] L. Polavarapu, N. Venkatram, W. Ji, Q.H. Xu, Appl. Mater. Interf. 1 (2009) 2298.

[20] S.-Y. Luo, B.-X. Yan, J. Shen, Thin Solid Films 522 (2012) 361

[21] J. C. Yu, W. Ho, Z. Jiang, and L. Zhang, Chem. Mater. 14 (2002) 3808.

[22] N. Sahoo, K. Apparao, Appl.Physics A 63 (1996) 195.

[23] U.I. Gaya, A.H. Abdullah, J. Photochem. Photobiol. C Photochem. Rev. 9 (2008) 1

[24] J. Huang, H. Zhang, X. Zhou, X. Zhong, Mater. Chem. Phys. 138 (2013) 755

[25] M.L. Rache, A.R. García, H.R. Zea, A.M.T. Silva, L.M. Madeira, J.H. Ramírez, Appl. Catal. B Environ. 146 (2014) 192

[26] M.H.H. Mahmoud, A.A. Ismail, M.M.S. Sanad, Chem. Eng. J. 187 (2012) 96

[27] R. Fateh, A.A. Ismail, R. Dillert, D.W. Bahnemann, J. Phys. Chem. C. 115 (2011) 10405

[28] A. Helal, F.A. Harraz, A.A. Ismail, T.M. Sami, I.A. Ibrahim, Mater. Des. 102 (2016) 202

[29] M. Mehrabian, Z. Esteki. Optik 130 (2017) 1168.

[30] A. Houas, H. Lachheb, M. Ksibi, E. Elaloui, C. Guillard, J.M. Herrmann. Appl. Catal. B: Environmental 31 (2001) 145.

[31] R.S. Dariani, A. Esmaeili, A. Mortezaali, S.Dehghanpour. Optik 127 (2016) 7143.

[32] R.M Mohamed, D.I Mckinney, W.M Sigmund, Mat. Sci. Eng. R, 73 (2012), 1

[33] Z. Chen, D. Li, W. Zhang, Y. Shao, T. Chen, M. Sun, X. Fu, J. Phys. Chem. C, 113 (2009), 4433.

[34] X. Rong, F. Qiu, J. Rong, J. Yan, H. Zhao, X. Zhu, D. Yang, J. Solid State Chem. 230 (2015) 126.

[35] N. Pradhan, D. Goorskey, J. Thessing, X.G Peng, J. Am. Chem. Soc, 127 (2005), 17586

CHAPTER 5

CONCLUSION

Bi(III) complexes of 4-methyl-N-phenyldithiocarbamate, N-phenyldithiocarbamate and N-benzyldithiocarbamate were successfully prepared and these complexes were characterized by NMR and FTIR spectroscopy. The FTIR spectroscopy for all the ligands (L) and complexes (BiL) was performed to give an insight into the nature of the functional groups present. FTIR spectra of the ligands for dithiocarbamate compounds and bismuth(III) complexes obtained in the range of 4000 – 280 cm^{-1}. The complexes showed the stretching frequency of ν(C=N) bands in the range of 1490 – I476 cm^{-1} for ν(C=N) showing the partial double bond character and 1241–1207 cm^{-1} for ν(C-N) shifting to greater frequencies. The complexes were also found stable and crystalline with very good yields. For both the ligands and complexes, the stretching frequency of υ(N-H) were found in the range of 3197– 3398 cm^{-1}, while the υ(N-H) bending vibration appeared around 1506 –1552 cm^{-1} respectively. The slight differences were observed between the three complexes and were assigned to the inductive effect of the methyl group substituent on the para-position of complex BiL^1_3 [($Bi(S_2CNHp\text{-}MePh)_3$]. The ^1H and ^{13}C NMR spectra for all the complexes were presented in chapter 3. The resonance in the complexes compared with the ligands confirmed the coordination of the metal ion with the dithiocarbamate ligand. However, the complexes showed similar values but with slight difference in complexBiL^1_3 due to the para-substituted methyl group on the dithiocarbmate moiety of [$Bi(S_2CNHp\text{-}MePh)_3$]. The complexes also showed the aromatic ring proton appearing in the range 7.51 – 7.18 ppm. The observed frequency of the aromatic protons, showed that the peaks with the higher values were assigned to the protons ortho- to the carbon of the thioureide group; thus the deshielding effect assigned to the higher resonant frequency value due to the electronegative nitrogen atom. Moreover, the ^{13}C NMR spectra of all the complexes showed the carbon signals in the range of 181–179 ppm assigned to the thioureide bond.Complex BiL^2_3showed the methylene carbon of the benzyl group was observed at 48.55 ppm. There is also an up-field shift observed for the resonance of (N-H) in all the complexes compared to the dithiocarbamate ligands and the carbon signals of the NCS_2 in the ^{13}CNMR which confirmed the coordination by CS_2. The aromatic carbon in the phenyl ring of the dithiocarbamate ligand is affected by the coordination of the bismuth sulphide and this caused a weak deshielding which

could be assigned to the movement of the electron density towards the nitrogen from the carbon atom and also increasing sulphur electron density from the dithiocarbamate group.

The as-prepared complexes were used as single source precursors for the Bi_2S_3 nanoparticles and metal doped Bi_2S_3 were also prepared using microwave, solvothermal, hydrothermal methods. Bi_2S_3 nanoparticles with nanorod morphology were synthesized by microwave, solvothermal and hydrothermal methods and were characterized by the following techniques: XRD, TEM, HRTEM, UV-vis. The XRD results confirmed that all the as-prepared Bi_2S_3 nanomaterials were orthorhombic phase. EDX confirmed that the doping of the Mn^{2+} and Sn^{2+} ions was present into the Bi_2S_3 nanomaterials and the crystal phase of pure Bi_2S_3 nanoparticles showed no change. Furthermore, the optical properties of Bi_2S_3 and metal doped Bi_2S_3 nanomaterials obtained from $[BiL^1{}_3]$, $[BiL^2{}_3]$ and $[BiL^3{}_3]$ complexes were analyzed using UV-vis spectroscopy. The band gap energies (Eg) were estimated using the Tauc equation $[(\alpha h\upsilon)^2$vs. $h\upsilon]$. From the Tauc plot, the observed band gaps were found around2.02– 2.04 eV for pure Bi_2S_3 nanoparticles and the absorption peaks were found around 638–644nm. However, the band gap of metal doped Bi_2S_3 nanomaterials were found to be lower around 1.64 – 1.73eV, with the absorption peaks around 717–730 nm. This indicates the band gap energy had shifted with the introduction of dopants compared to the pure Bi_2S_3 band gap (1.3 eV), and it was due to quantum confinement effect. TEM images of Bi_2S_3 and metal doped Bi_2S_3 confirmed the different size and shape of the nanorods with 100 nm in length and 20 nm in diameter. Nanoparticles with spherical morphology whose sizes are less than 100 nm were obtained from microwave methods. However it is difficult to estimate the exact sizes of nanoparticles from the TEM images without compromising on the number of images required to make a reasonable average size determination. The metal doped Bi_2S_3 nanorods showed very tiny particles size of nanorods and also there appeared to be an observable decrease in diameter of the nanorods in the metal doped Bi_2S_3 nanoparticles. The undoped and the doped Bi_2S_3 nanoparticles showed crystallinity as revealed by the HRTEM images and this was confirmed by the presence of lattice fringes.

The photocatalytic degradation activities of the undoped and metal doped Bi_2S_3 were evaluated using methylene blue as the organic substrate. The photocatlytic properties for the undoped Bi_2S_3 and metal doped Bi_2S_3 nanorods showed good photocatalytic activity as well as stability in the degradation of methylene blue under UV-vis irradiation source. The undoped Bi_2S_3 nanorods

showed photocatalytic degradation efficiency of 82-87% while metal doped Bi_2S_3 nanorods showed photocatalytic activity of 92-96%. The highly improved photocatalytic degradation efficiency of metal doped Bi_2S_3 nanoparticles can be explained by increasing the UV-vis light absorption and efficient charge separation. The report recommends that these can be applied in the environmental remediation and water treatment.

5.2 FUTURE STUDIES

Based on the conclusion of this research there are still some things that can be study further in order to understand the effect of the conditions:

1. The investigation of the same complexes to confirm complete dye degradation.

2. There is also need to test the Bi_2S_3 nanomaterials on real waste-water containing methylene blue dye as part of future studies

3. Improve the quality of the synthesized materials

APPENDIX

FTIR results

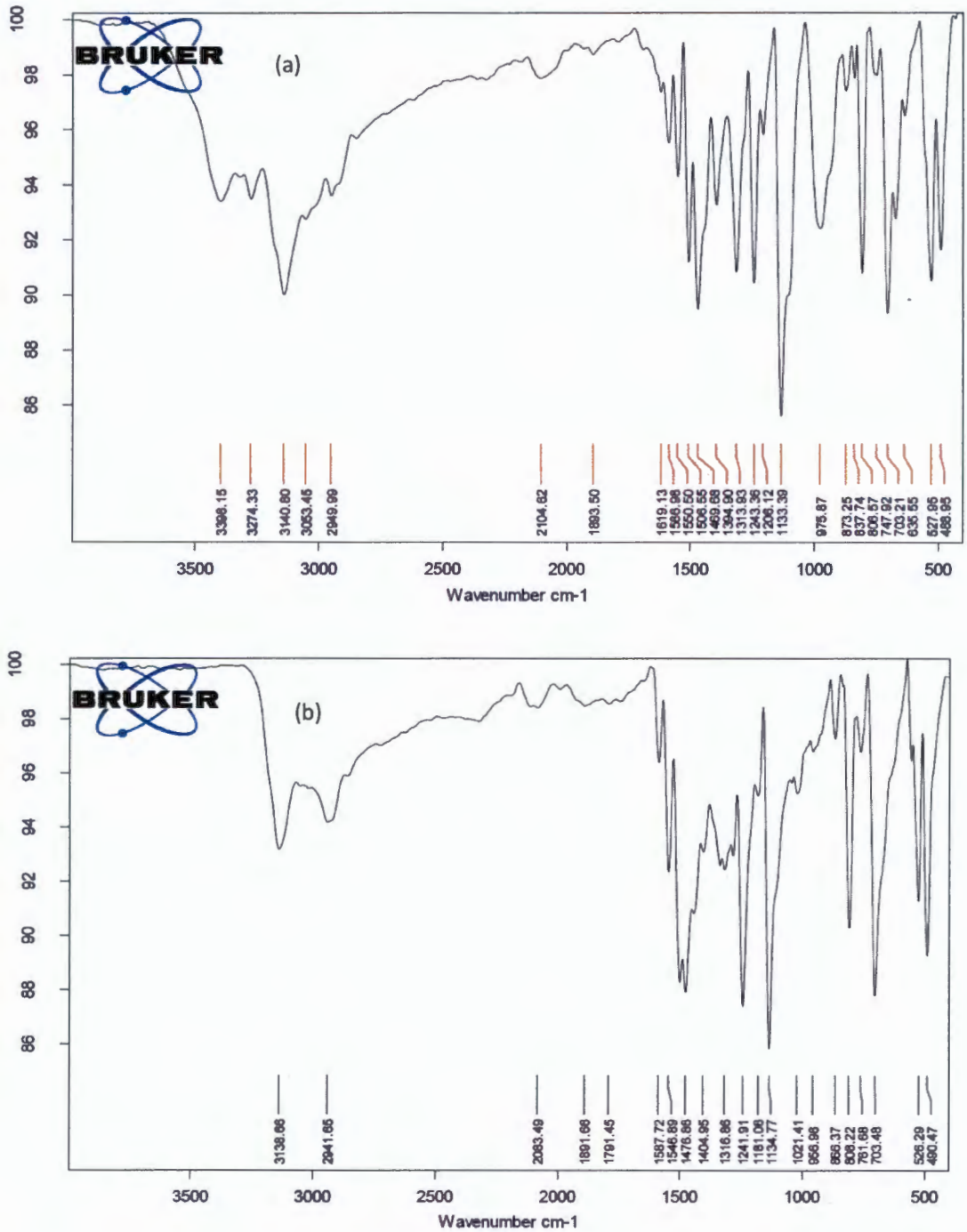

Figure **S1:** (a) **NaL**[1] and (b) **BiL**[1]$_3$ (4-methyl-N-phenyldithiocarbamate)

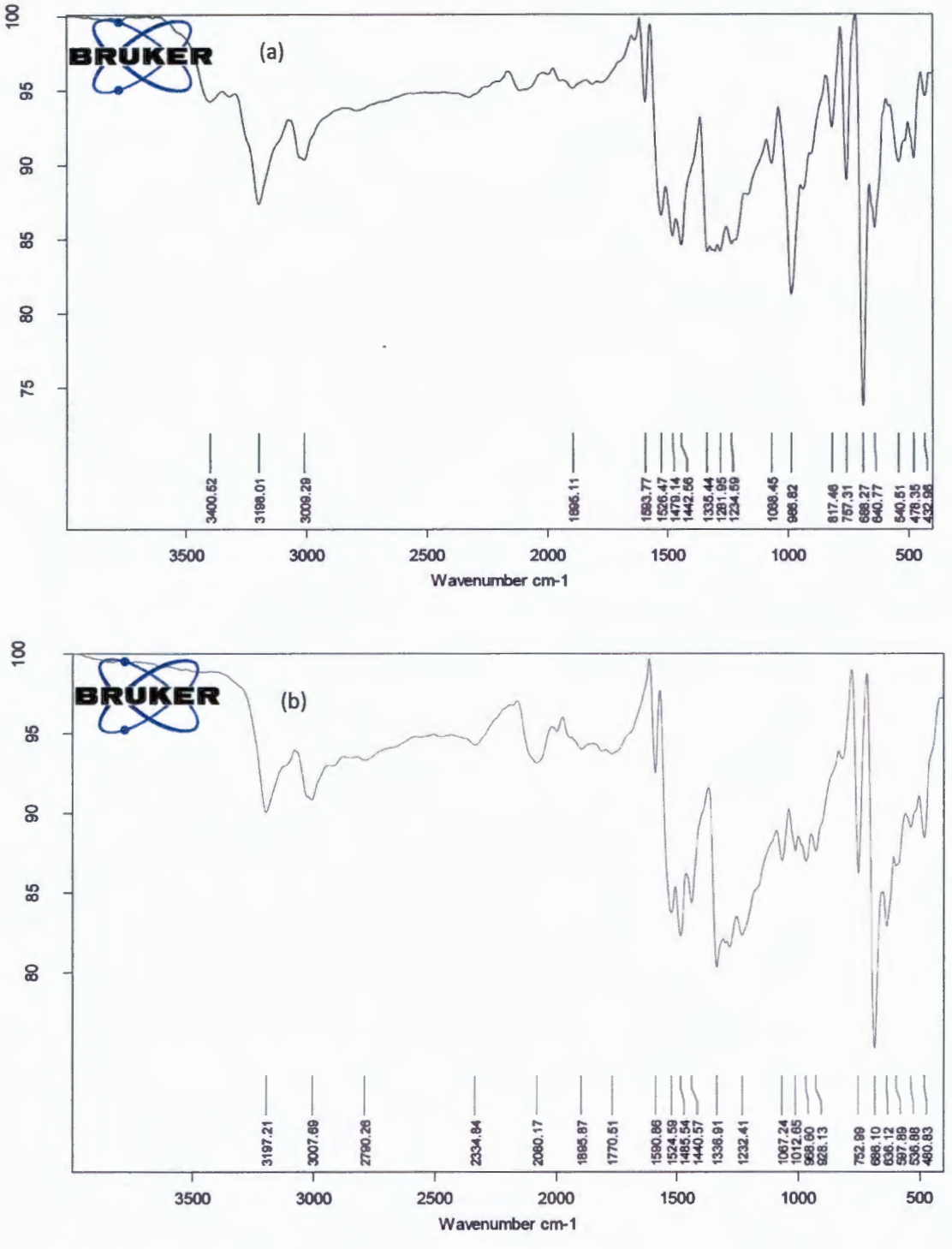

Figure **S2:** (a) **NaL**^{2} and (b) **BiL**$^2{}_3$ (N-phenyldithiocarbamate)

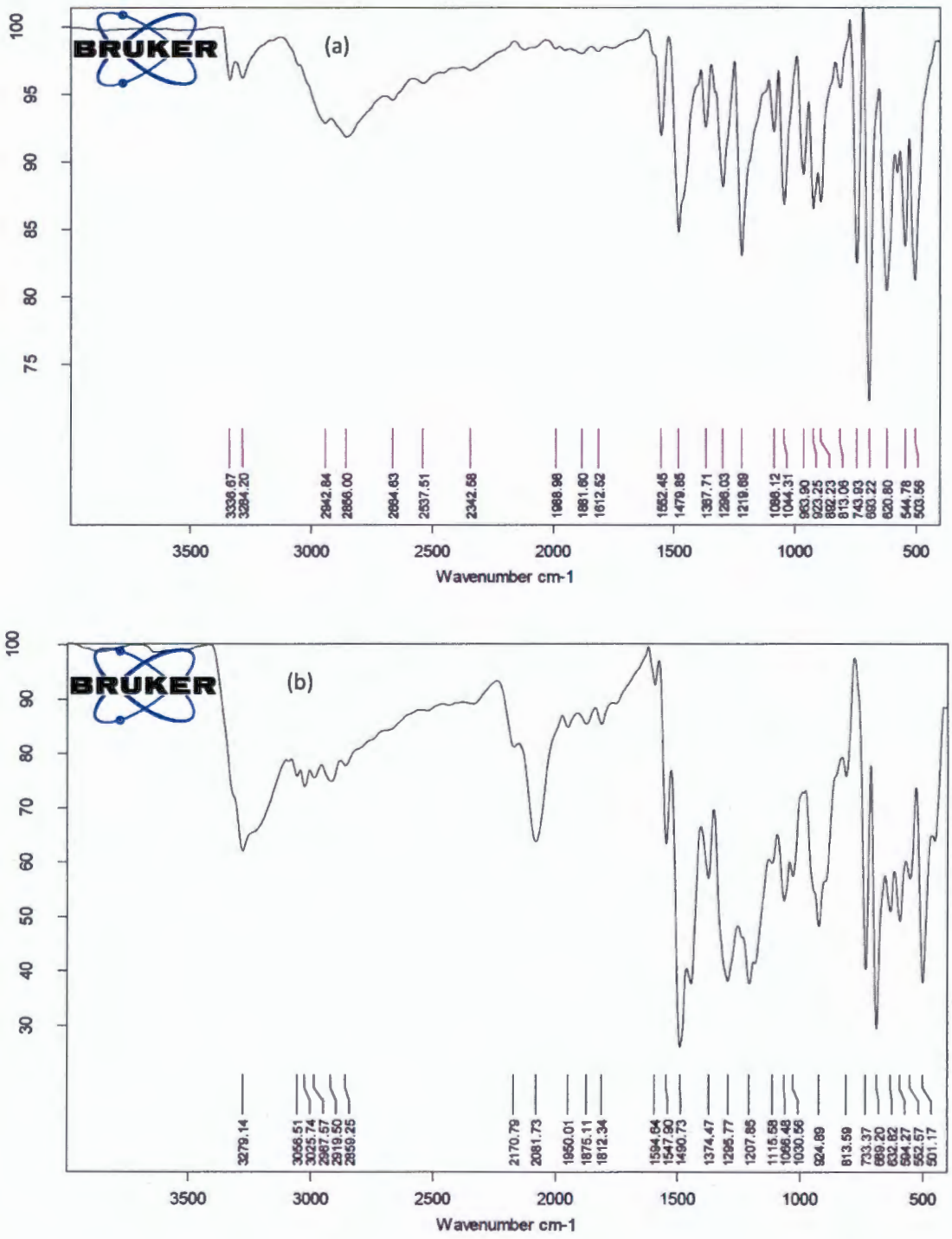

Figure **S3:** (a) **NaL^3** and (b) **BiL$^3_3$** (N-benzyldithiocarbamate)